Lattice Calculation of the $\pi^0 \to e^+e^-$ and the $K_L \to \gamma\gamma$ Decays

Yidi Zhao

Submitted in partial fulfillment of the
requirements for the degree of
Doctor of Philosophy
under the Executive Committee
of the Graduate School of Arts and Sciences

COLUMBIA UNIVERSITY

2022

Abstract

Lattice Calculation of the $\pi^0 \to e^+e^-$ and the $K_L \to \gamma\gamma$ Decays

Yidi Zhao

In the standard model the rare kaon decay $K_L \to \mu^+\mu^-$ is a highly suppressed, "strangeness changing neutral current process" that requires the exchange of two weak bosons with an accurately measured branching fraction $B(K_L \to \mu^+\mu^-) = (6.84 \pm 0.11) \times 10^{-9}$ [1]. For this measurement to become an important short-distance test of the standard model, the competing $O(\alpha_{\rm EM}^2 G_{\rm F})$ two-photon contribution must be computed and removed from the total decay amplitude. While the imaginary part of this contribution can be obtained from the $K_L \to \gamma\gamma$ decay rate and the optical theorem, the real part must be computed in QCD [2]. Depending on a relative sign, a 10% calculation of the real part of the $O(\alpha_{\rm EM}^2 G_{\rm F})$ two-photon contribution would lead to a 6% or 17% test of the standard model.

As a first step in developing a strategy for computing the two-photon contribution to the $K_L \to \mu^+\mu^-$ decay, we examine a simpler process $\pi^0 \to e^+e^-$. Here no weak interaction vertex is involved and, more importantly, there is no intermediate hadronic state with a mass smaller than that of the initial pion. The sole complication arises from the presence of the two-photon intermediate state, only one of the difficulties offered by the $K_L \to \mu^+\mu^-$ decay. We show that the $\pi^0 \to e^+e^-$ amplitude can be calculated with an analytic continuation method where the entire decay amplitude including the imaginary part is preserved. The real part involves non-perturbative QCD contribution and is of substantial interest, while the imaginary part of calculated amplitude can be compared with the prediction of optical theorem to demonstrate the effectiveness of this

method. We obtain $\mathrm{Re}\mathcal{A} = 18.60(1.19)(1.04)$ eV, $\mathrm{Im}\mathcal{A} = 32.59(1.50)(1.65)$ eV and a more precise value for their ratio $\frac{\mathrm{Re}\mathcal{A}}{\mathrm{Im}\mathcal{A}} = 0.571(10)(4)$ from continuum extrapolation of two lattice ensembles, where $\mathcal{A}$ is the decay amplitude, the error in the first parenthesis is statistical and the error in the second parenthesis is systematic.

Next, we develop a computational strategy to determine the $K_L \to \gamma\gamma$ decay amplitude. It involves the same hadronic matrix element as the $K_L \to \mu^+\mu^-$ decay as well as all the intermediate states whose energies are lower than or close to the initial kaon sate except for the $|\pi\pi\gamma\rangle$ that is difficult to deal with. While the lattice QCD calculation is carried out in finite volume, the emitted photons are treated in infinite volume and the resulting finite-volume errors decrease exponentially in the linear size of the lattice volume. Only the CP-conserving contribution to the decay is computed and we must subtract unphysical contamination resulting from single pion and eta intermediate states which grow exponentially (or fall slowly) as the time separation between the initial and final lattice operators is increased. Results from a calculation without disconnected diagrams on a $24^3 \times 64$ lattice volume with $1/a = 1$ GeV and physical quark masses are presented.

Table of Contents

List of Figures

List of Tables

Acknowledgements

First and foremost I would like to thank my advisor Prof. Norman Christ for his support in the completion of this project and throughout my graduate research. His passion for physics and energetic characteristics are such a great inspiration to me. The weekly discussion is fruitful and constantly produces ideas without which these inventions would be impossible.

I am grateful to Prof. Robert Mawhinney for all the insightful discussions during the group meetings and help on the machines. I greatly appreciate Professor Luchang Jin, Chris Kelly, Cheng Tu, and Professor Xu Feng's substantial help and close collaboration on the project.

I would also like to thank my colleagues: Joseph Karpie, Masaaki Tomii, Yong-Chull Jang, Bigeng Wang, Tianle Wang, Jiqun Tu, Duo Guo, Yikai Huo, and many others in RBC&UK QCD collaboration. I thoroughly enjoy working with such a great team of people and benefit greatly from their help and discussions.

Finally, I would like to thank my fiancée, Qi Sheng, for all her love and support during my difficult times.

Chapter 1: Introduction and background

The standard model of particle physics, based on the formulation of quantum field theory, is the theory describing three of the four known fundamental forces – the electromagnetic, weak, and strong interactions. The standard model is one of the most well-tested physics theories. Since its establishment in the 1970s, the standard model has explained almost all experimental results in particle physics with great accuracy and successfully predicted the existence of new particles, including the $W^{\pm}$ and Z boson, top quark, tau neutrino, and the Higgs boson.

The electromagnetic interaction is described by quantum electrodynamics (QED) and is believed to be well understood because of the simplicity of QED theory and the excellent agreement with experiments. One of the most famous examples is that the electron's anomalous magnetic moment was measured to agree with theory to an accuracy of around one part in one billion.

Quantum chromodynamics (QCD), established after the discovery of the quark model in the 1960s, is the fundamental quantum field theory that describes strong interactions through quarks and gluons. It is a non-Abelian SU(3) gauge theory where the three kinds of charge are usually referred to as colors . Because of the property of asymptotic freedom, QCD perturbation theory is used to accurately explain experiments performed at very high energies. However, at low energies close to or below the scale of Λ_{QCD}, the value of the strong coupling constant α_s is considerably larger and the QCD perturbation theory breaks down. Various effective theories, like the chiral perturbation theory, are very successful in predicting the strong interaction process in the low-energy regime. However, these methods are based on approximate symmetries and other approximations instead of a calculation from the first principles.

The weak interaction is complicated and unique in many ways. It is the only interaction that can change the flavor of quarks, the only interaction that violates CP symmetry, and also the only interaction where gauge bosons have mass. Because of these intriguing properties, the weak inter-

action provides great potential for discovering new physics beyond the standard model. Some of the most important examples include the direct and indirect CP-violating parameters ε and ε', the rare kaon decays, and the K_L-K_S mass difference.

Since its inception about 40 years ago, lattice QCD is the only known method to define the quantum field theory in a non-perturbative way and to perform nonperturbative QCD calculations from the first principles. Lattice methods augment traditional theoretical studies and extend the reach of low energy, high-precision searches for physics beyond the standard model. First-principles calculations of these standard model predictions using the methods of lattice QCD are becoming increasingly accurate and applicable to a wider range of phenomena. With the advances in supercomputers and lattice QCD algorithms in the last decades, direct calculation with physical light and strange quark masses has become feasible. This removed the need for extrapolations to obtain physical results and greatly reduced the errors in lattice calculations.

The weak interactions which occur in rare kaon decays provide an important opportunity to search with high sensitivity for phenomena not predicted by the standard model. In this work, we study the strangeness-changing neutral current process $K_L \to \mu^+\mu^-$. The short-distance contribution of this decay arises as a one-loop, second-order weak process involving the exchange of two $W^\pm$ bosons or one $W^\pm$ and one Z^0 [2]. The second-order decay amplitude can be computed in the standard model with the kaon decay constant f_K as the only required hadronic input. However, this test of the standard model at second order is made complicated by the presence of an order $\alpha_{\rm EM}^2 G_F$ decay amplitude from the two-photon contribution. Thus, for this process, we might hope to use lattice QCD to perform an accurate calculation of this background, two-photon process so that the complete decay could then be computed in the standard model.

The presence of various intermediate states whose energies are lower than kaon mass poses great challenges to the computation of the two-photon contribution to $K_L \to \mu^+\mu^-$ decay in lattice QCD. To tackle these difficulties step by step, in this work, we developed methods to calculate the $\pi^0 \to e^+e^-$ decay and the $K_L \to \gamma\gamma$ decay. These two decays are similar to the two-photon contribution to the $K_L \to \mu^+\mu^-$ decay in some aspects and the lattice calculation of these two

decays can be compared with experimental results to demonstrate the effectiveness of our methods.

This work is organized as follows. In Chapter 2, we briefly review the physics of the rare kaon decay $K_L \to \mu^+\mu^-$ in the standard model. In Chapter 3, we discuss the lattice QCD framework, the computation of quark propagators, and how to measure physical quantities on the lattice. In Chapter 4 we develop a new method of combining EM interactions and lattice QCD calculation and deal with the two-photon intermediate state. We also present the first first-principles calculation of the $\pi^0 \to e^+e^-$ decay. In Chapter 5, we show the formalism that we have developed to carry out the first calculation of the $K_L \to \gamma\gamma$ decay. The calculated decay amplitude agrees well with experimental values. In Chapter 6, we summarize our results and discuss the future prospects for calculating the $K_L \to \mu^+\mu^-$ decay.

Chapter 2: The physics of the $K_L \to \mu^+\mu^-$ decay

In this chapter, we review the physics of the $K_L \to \mu^+\mu^-$ decay in the standard model. In Section 2.1, we examine the experimental measurements of the $K_L \to \mu^+\mu^-$ decay amplitude and show how a lattice calculation with 10% accuracy will lead to an important test of the standard model. In Section 2.2, we show that an effective field theory with only u, d, and s quarks can be obtained at low energies by integrating out the heavy degrees of freedom. The effective weak Hamiltonian is composed of four-quark operators and can be calculated with lattice QCD. In Section 2.3, we discuss the most important challenge in the lattice calculation of the $K_L \to \mu^+\mu^-$ decay, which is the presence of various intermediate states whose energies are lower than that of the initial kaon state.

2.1 Overview of the $K_L \to \mu^+\mu^-$ decay

The rare decays of K mesons provide important opportunities for the discovery of physics beyond the standard model. For such processes, a combination of highly sensitive experiments with increasingly accurate lattice QCD calculations should result in continually more sensitive tests of the standard model.

We study the $K_L \to \mu^+\mu^-$ decay because, in contrast to similar processes like the $K_S \to \mu^+\mu^-$ and $K_L \to e^+e^-$ decay, it has larger branching ratio and its branching ratio is accurately measured [1]:

$$\mathrm{BR}(K_L \to \mu^+\mu^-) = (6.84 \pm 0.11) \times 10^{-9}. \tag{2.1}$$

The decay amplitude is composed of a short-distance contribution and a two-photon contribution. The short-distance contribution, as shown in Figure 2.1, is mediated by two W bosons or two

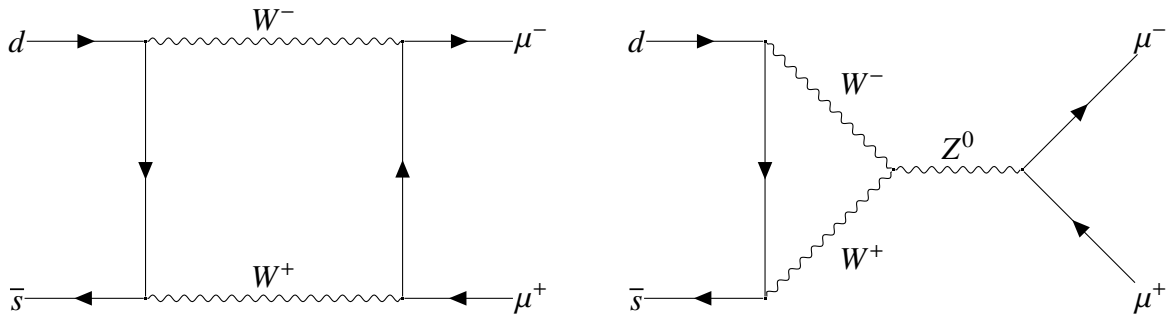

Figure 2.1: The short-distance contribution to the $K_L \to \mu^+\mu^-$ decay. The short-distance contribution is mediated by two W bosons.

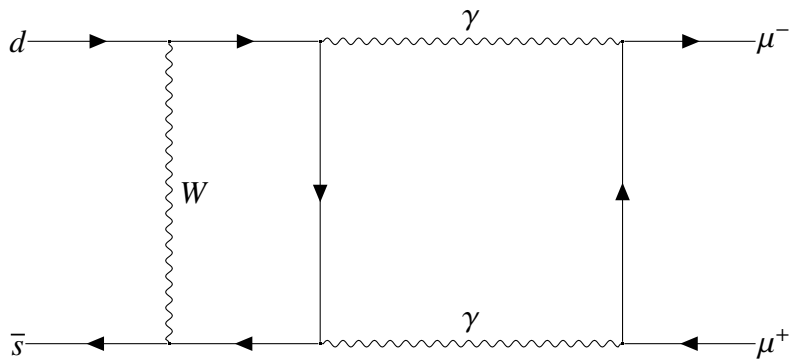

Figure 2.2: The two-photon contribution to the $K_L \to \mu^+\mu^-$ decay.

W bosons and a Z boson. The short-distance contribution has physics interest because it is a highly suppressed strangeness-changing neutral current process that can provide an important test of the standard model. However, there is also a two-photon contribution, as shown in Figure 2.2, that is mediated by two photons and dominates the decay amplitude. In order to compare the standard model prediction of short-distance contribution with the experiments, we must first calculate this $O(\alpha_{\rm EM}^2 G_F)$ two-photon contribution and combine it with the short-distance contribution and then compare with the observed experimental decay rate.

The two-photon contribution is described by a complex amplitude whose imaginary part is determined by the optical theorem and the known $K_L \to \gamma\gamma$ decay rate. Using the notation of Ref. [2]:

$$\frac{\Gamma(K_L \to \mu^+\mu^-)}{\Gamma(K_L \to \gamma\gamma)} = 2\beta_\mu \left(\frac{\alpha_{\rm EM}}{\pi}\frac{m_\mu}{M_K}\right)^2 \left(|F_{\rm imag}|^2 + |F_{\rm real}|^2\right), \tag{2.2}$$

where $\alpha_{\rm EM} = 1/137$ is the fine-structure constant of the electromagnetic interaction, m_μ is the mass

of muon, M_K is the mass of kaon, and β_μ is a dimensionless constant defined as

$$\beta_\mu = \sqrt{1 - \frac{4M_\mu^2}{M_K^2}}. \tag{2.3}$$

The imaginary part gets contributions from several available on-shell states, but is completely dominated by the $\gamma\gamma$ intermediate state:

$$F_{\text{imag}} = \frac{\pi}{2\beta_\mu} \ln\left(\frac{1-\beta_\mu}{1+\beta_\mu}\right). \tag{2.4}$$

The experimental decay rate and the known imaginary part determine $|F_{\text{real}}| = 1.167 \pm 0.094$. The real part of the decay amplitude gets contributions from both the two-photon part and the short-distance part

$$F_{\text{real}} = (F_{\text{real}})_{\text{EM}} + (F_{\text{real}})_{\text{weak}}\,. \tag{2.5}$$

The standard model predicts at one loop: $(F_{\text{real}})_{\text{weak}} = -1.82 \pm 0.04$. Thus, a lattice calculation of $(F_{\text{real}})_{\text{EM}}$ with 10% accuracy would determine $(F_{\text{real}})_{\text{weak}}$ to 6% or 17% depending on whether F_{real} and $(F_{\text{real}})_{\text{weak}}$ have the same or opposite signs, which could serve as an important test of the standard model.

2.2 The operator product expansion and the effective weak Hamiltonian

In the standard model, the strangeness-changing processes with $\Delta S = 1$ are allowed through the exchange of W boson. Since the masses of heavy particles like the W boson are much larger than the mass of kaon, at a low energy scale, the heavy degrees of freedom can be integrated out and the interaction can be effectively described by the four-quark operators. The effective weak

Hamiltonian with $\Delta S = 1$ is a sum of local four-quark operators

$$H_W^{\Delta S=1} = \frac{G_F}{\sqrt{2}} V_{us}^* V_{ud} (C_1 Q_1 + C_2 Q_2), \tag{2.6}$$

where G_F is the Fermi constant, V_{us} and V_{ud} are the CKM matrix elements, C_1 and C_2 are the Wilson coefficients, and Q_1 and Q_2 are the four-quark operators

$$Q_1 = (\bar{s}_a \gamma_L d_a)(\bar{u}_b \gamma_L u_b) = \sum_\mu \left(\bar{s}_a \gamma_\mu (1-\gamma_5) d_a\right) \left(\bar{u}_b \gamma_\mu (1-\gamma_5) u_b\right) \tag{2.7}$$

$$Q_2 = (\bar{s}_a \gamma_L d_b)(\bar{u}_b \gamma_L u_a) = \sum_\mu \left(\bar{s}_a \gamma_\mu (1-\gamma_5) d_b\right) \left(\bar{u}_b \gamma_\mu (1-\gamma_5) u_a\right), \tag{2.8}$$

where a and b are color indices and the spin indices are contracted within each pair of brackets. The operators Q_1 and Q_2 are called current-current operators because they originate from the W boson exchange between two quark currents, as shown by the diagrams in Figure 2.3. There are additional 8 operators in the weak Hamiltonian, called QCD penguin operators and electroweak penguin operators. However, the decay amplitude is dominated by the two current-current operators and we ignore the other 8 operators in this work.

The Wilson coefficients contain the contribution of the high energy part which has been integrated out from the full theory. The low energy part is then described by the four-quark operators Q_i. Therefore, effectively, we divide the calculation in the full theory into two parts: the high energy part is calculated perturbatively, while the low energy part, which is complicated because of the inapplicability of the asymptotic freedom property of QCD, is calculated on the lattice in a non-perturbative way.

2.3 Intermediate states in the two-photon contribution

The real part of the amplitude represented in Figure 2.2 can be obtained in Euclidean space. However, such a Euclidean space evaluation will contain other, unphysical terms which will often dominate the limit of large time separation needed in such a Euclidean space calculation to project

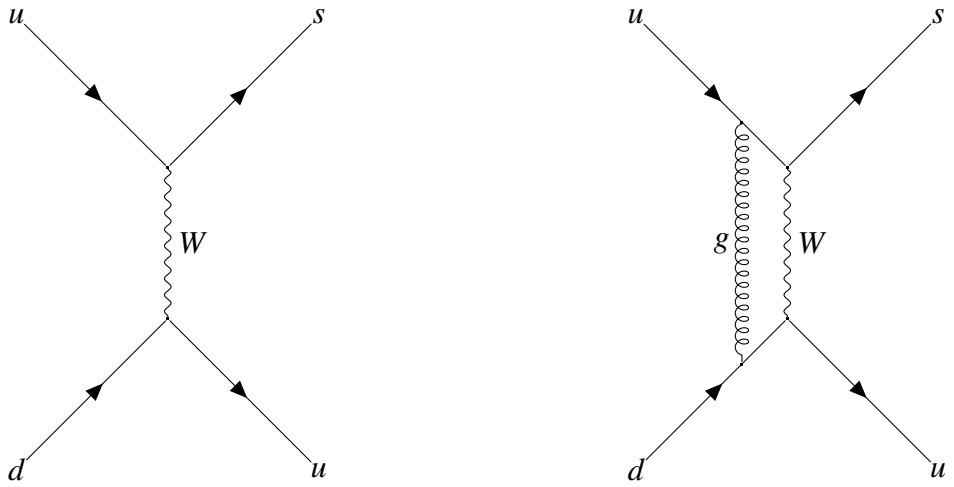

Figure 2.3: Feynman diagrams in the full theory from which the current-current operators Q_1 and Q_2 originate.

onto the kaon ground state. These additional terms are referred to as exponentially growing with increasing time separation because they correspond to possible intermediate states with energy less than that of the kaon. Suppose energy of such a state $|n\rangle$ is E_n and is smaller than M_K. As a result as one increases the time separation T between the operator which creates the K_L and the operators which absorb the final muons, a large contribution will come when H_W and J_ν quickly convert the kaon into a $|n\rangle$ state with energy E_n. This light state propagates from the location of the kaon to the leptonic E&M current which absorbs that photon. For the component of interest, a state with energy M_K propagates over the time interval T (as either the initial kaon or the final $\mu^+\mu^-$ pair), with a short-range interaction causing the $K_L \to \mu^+\mu^-$ transition of interest over a time interval of length $1/\Lambda_{\text{QCD}}$. The former dominates over the latter by the exponentially growing factor $\exp\{-(E_n - M_K)T\}$.

The most important intermediate state with energy less than that of the kaon is the two-photon intermediate state. In Chapter 4, we propose a method to tackle the problem of the two-photon intermediate states based on analytic continuation and apply this method to perform a lattice computation of a simpler process, the $\pi^0 \to e^+e^-$ decay.

Besides the two-photon intermediate state, depending on the time order of the operator in the matrix element $\langle T\{J_\mu(u)J_\nu(v)H_W(x)K_L(t_k)\}\rangle$, it will have the following intermediates states whose

energies are lower than or close to that of kaon:

- $\langle J_\mu(u) J_\nu(v) H_W(x) K_L(t_k)\rangle$: There can be $|\pi\rangle$ and $|\eta\rangle$ states between $J_\nu(v)$ and $H_W(x)$ or a $|\gamma\pi\pi\rangle$ state between $J_\mu(u)$ and $J_\nu(v)$.

  Since we ignore CP violation, $|0\rangle$ and $|\pi\pi\rangle$ intermediate states are not allowed between two EM currents and weak Hamiltonian. We also ignore the three-pion state $|\pi\pi\pi\rangle$ because its phase space is much smaller than that of the single-pion state $|\pi\rangle$.

- $\langle J_\mu(u) H_W(x) J_\nu(v) K_L(t_k)\rangle$: There can be $|\gamma\pi\pi\rangle$ state between $J_\mu(u)$ and $H_W(x)$.

- $\langle H_W(x) J_\mu(u) J_\nu(v) K_L(t_k)\rangle$: There are no intermediate states with energies lower than kaon mass.

The presence of the $|\gamma\pi\pi\rangle$ state poses significant challenges to the computation of the decay amplitude. Figure 2.4 shows such time order for which two pions and a photon can appear between H_W and the left-most EM current J_μ. Unlike the $|\pi\rangle$ or $|\eta\rangle$ intermediate states, the exponentially growing contribution from the $|\gamma\pi\pi\rangle$ state is hard to calculate and remove. Because of the difficulty of dealing with the $|\gamma\pi\pi\rangle$ immediate state, in this work, we first calculate a simpler decay, the $K_L \to \gamma\gamma$ decay. Since the two photons are on-shell, the $|\pi\pi\rangle$ state has to carry momentum $\vec{p}$ that whose magnitude is equal to half of the initial kaon energy,

$$|\vec{p}| = \frac{M_K}{2}. \tag{2.9}$$

Therefore, the energy of the $|\gamma\pi\pi\rangle$ intermediate state is larger than the kaon mass and does not bring in exponential divergence.

In Chapter 5, we develop the formalism to calculate the $K_L \to \gamma\gamma$ decay amplitude in lattice QCD and to deal with these intermediate states.

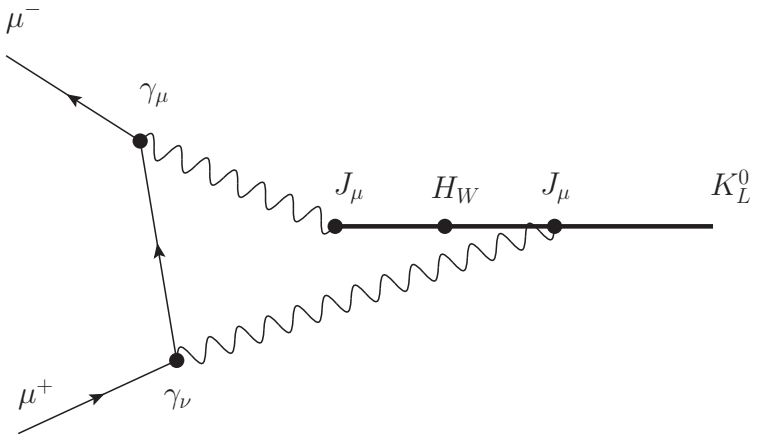

Figure 2.4: Schematic diagram showing the two-photon contribution to $K_L \to \mu^+\mu^-$ decay. The dark solid line represents the hadronic part of the amplitude connecting the two E&M currents, the weak Hamiltonian and the initial kaon, in specific time order.

Chapter 3: General lattice QCD approach

In this chapter, we discuss the general lattice QCD procedures in calculating physical decay amplitudes. In Section 3.1, we present the general lattice QCD framework to compute physical quantities in a non-perturbative way. We introduce the Iwasaki gauge action and the domain wall fermion action which are used to generate gauge configurations in the hybrid Monte Carlo procedure. In Section 3.2, we show how to extract matrix elements and hadron masses from the Euclidean correlators of lattice interpolating operators. In Section 3.3, we explain the calculation of quark propagators on the lattice, which is the most computationally expensive part of the lattice QCD calculation. We also discuss the low-mode inflation and preconditioning techniques to speed up the calculation of quark propagators using the conjugate gradient algorithm. We use a special type of propagator called random volume source propagators to stochastically approximate the self-contracting quark loops. In Section 3.4, we discuss the calculation of the Wilson coefficients and the renormalization of the $\Delta S = 1$ weak Hamiltonian operator. In the last section 3.5, we present the jackknife resampling method which is used in this work to estimate the statistical errors for the physical quantities calculated on the lattice.

3.1 Introduction to lattice QCD

In lattice QCD, we discretize spacetime into a four-dimensional Euclidean grid. The gauge field, denoted by $U_\mu(n)$, takes on the value of a SU(3) matrix for each link that connects the two neighboring lattice sites n and $n + \hat{\mu}$. It can be viewed as the exponential of the continuum gauge field $A_\mu(n)$

$$U_\mu(n) = \exp(iagA_\mu(n)), \tag{3.1}$$

where a is the lattice spacing and g is the QCD coupling constant. Wilson introduced the first lattice gauge action [3]

$$S_G[U] = \frac{\beta}{3} \sum_n \sum_{\mu<\nu} \text{Re tr}[I - U_{P,\mu\nu}(n)], \tag{3.2}$$

where I is the identity matrix and $U_{P,\mu\nu}(n)$ is the 1×1 plaquette formed by four adjacent gauge links

$$U_{P,\mu\nu}(n) = U_\mu(n) U_\nu(n + \hat{\mu}) U_\mu^\dagger(n + \hat{\nu}) U_\nu^\dagger(n). \tag{3.3}$$

It is easy to show that the Wilson gauge action preserves the gauge invariance symmetry, and with the choice of $\beta = \frac{6}{g^2}$ it converges to the following continuum gauge action in the limit of $\beta \to \infty$:

$$S_G^{\text{cont}} = \frac{1}{2} \int d^4x \ \text{tr}[F_{\mu\nu}(x)^2], \ \text{where } F_{\mu\nu}(x) = \partial_\mu A_\nu(x) - \partial_\nu A_\mu(x) + i[A_\mu(x), A_\nu(x)]. \tag{3.4}$$

In this work, we use an improved version of the Wilson gauge action that is called the Iwasaki gauge action [4]. Besides the 1×1 square plaquette, it introduced another term, the 1×2 rectangular plaquette:

$$S_G[U] = \beta \sum_n \left(\left(1 - \frac{c_0}{3}\right) \sum_{\mu<\nu} \text{Re tr}[U_{P,\mu\nu}(n)] + \left(1 - \frac{c_1}{3}\right) \sum_{\mu\neq\nu} \text{Re tr}[U_{R,\mu\nu}(n)] \right), \tag{3.5}$$

where $c_1 = -0.331$ and $c_0 = 1 - 8c_1$ are two constants, and $U_{R,\mu\nu}(n)$ is the 1×2 rectangular plaquette

$$U_{R,\mu\nu}(n) = U_\mu(n) U_\mu(n + \hat{\mu}) U_\nu(n + 2\hat{\mu}) U_\mu^\dagger(n + \hat{\mu} + \hat{\nu}) U_\mu^\dagger(n + \hat{\nu}) U_\nu^\dagger(n). \tag{3.6}$$

Compared to the original Wilson action, the Iwasaki action has better rotation symmetry and chiral symmetry when combined with a chiral fermion action such as the domain wall fermion (DWF)

action.

Fermions on the lattice are represented by anti-commuting Grassman numbers ϕ. The discretization of the fermion action is more complicated than the gauge action since a naive discretization would lead to certain lattice artifacts called doublers. Wilson introduced the so-called Wilson fermion action in which an extra term is added to remove these doublers. However, the additional term explicitly breaks chiral symmetry which plays an important role in quantum field theory. The domain wall fermion (DWF) [5] is a formulation that is free of the fermion doubling problem and has approximate chiral symmetry.

In the domain wall fermion action, we introduce a fifth dimension labeled by s. Let L_s be the number of lattice points in the fifth dimension. Left-handed fermions and right-handed fermions are bounded to the walls $s = 0$ and $s = L_s - 1$. The chiral symmetry breaking effects are exponentially suppressed as the size of the fifth dimension gets larger, and exact chiral symmetry is recovered as L_s goes to infinity. The domain wall fermion action is defined as

$$S_F = \sum_{n,n'} \sum_{s,s'} \bar{\psi}(n,s) D_{\mathrm{DWF}}(n,s;n',s') \psi(n',s') \tag{3.7}$$

$$D_{\mathrm{DWF}}(n,s;n',s') = \delta_{s,s'} D^{\parallel}_{n,n'} + \delta_{n,n'} D^{\perp}_{s,s'}, \tag{3.8}$$

where $D^{\parallel}_{n,n'}$ is basically the Wilson fermion Dirac operator but with negative mass $-M_5$:

$$D^{\parallel}_{n,n'} = (M_5 - 4)\,\delta_{n,n'} + \frac{1}{2} \sum_{\mu} \left[(1-\gamma_\mu) U_\mu(n) \delta_{n+\hat{\mu},n'} + (1+\gamma_\mu) U^{\dagger}_{\mu}(n') \delta_{n-\hat{\mu},n'} \right], \tag{3.9}$$

and

$$D^{\perp}_{s,s'} = \frac{1}{2} \left[(1-\gamma_5)\,\delta_{s+1,s'} + (1+\gamma_5) \delta_{s-1,s'} - 2\delta_{s,s'} \right] \tag{3.10}$$

$$- \frac{m_f}{2} \left[(1-\gamma_5)\,\delta_{s,L_s-1} \delta_{s',0} + (1+\gamma_5) \delta_{s,0} \delta_{s',L_s-1} \right]. \tag{3.11}$$

The new parameter M_5 is called the domain wall height and is not to be confused with the fermion

mass parameter m_f. The DWF action is free of doublers when $0 < M_5 < 2$.

Even though the DWF action solves the fermion doubling problem and recovers chiral symmetry, it is computationally expensive because of the introduction of the fifth dimension. Mobius domain wall fermions [6] is an improved version of the original DWF action that greatly reduces chiral symmetry violations and allows us to use a smaller number of lattice points in the fifth dimension while achieving the same level of chiral symmetry.

Once the actions are defined, the expectation value of any physical observable is calculated from the Euclidean space path integral

$$\langle O\left(U,\psi,\bar{\psi}\right)\rangle = \frac{\int \mathcal{D}[U]\mathcal{D}[\psi]\mathcal{D}[\bar{\psi}]e^{-S_G[U]-S_F[U,\psi,\bar{\psi}]}O\left(U,\psi,\bar{\psi}\right)}{\int \mathcal{D}[U]\mathcal{D}[\psi]\mathcal{D}[\bar{\psi}]e^{-S_G[U]-S_F[U,\psi,\bar{\psi}]}}. \tag{3.12}$$

The integral over the Grassmann variables can be computed analytically and will give us the determinant of the fermion Dirac operator

$$\langle O\left(U,\psi,\bar{\psi}\right)\rangle = \frac{\int \mathcal{D}[U]e^{-S_G[U]}\det(D_{\mathrm{DWF}})\langle O\rangle_{\mathrm{F}}(U)}{\int \mathcal{D}[U]e^{-S_G[U]}\det(D_{\mathrm{DWF}})}, \tag{3.13}$$

where the subscript in $\langle O\rangle_{\mathrm{F}}$ denotes that the fermion fields have been integrated out and $\langle O\rangle_F$ typically consists of a combination of quark propagators and gamma matrices. Because $\det(D) = \exp\left(\mathrm{tr}\left[\ln(D)\right]\right)$, the fermion determinant can be interpreted as an additional term in the gauge action and is called the effective fermion action. Then,

$$\langle O\left(U,\psi,\bar{\psi}\right)\rangle = \frac{\int \mathcal{D}[U]e^{-S[U]}\langle O\rangle_{\mathrm{F}}(U)}{\int \mathcal{D}[U]e^{-S[U]}} \tag{3.14}$$

$$\text{where } S[U] = S_G[U] + S_{\mathrm{eff}}[U] \tag{3.15}$$

$$S_{\mathrm{eff}}[U] = -\mathrm{tr}\left[\ln(D_{\mathrm{DWF}})\right]. \tag{3.16}$$

This path integral can be approximated by importance sampling Monte Carlo integration. In lattice QCD, we first use the Hybrid Monte Carlo (HMC) method to generate a sequence of gauge configurations U_i that are distributed according to $e^{-S[U]}$. Then, the functional integral is approxi-

mated by an average over these gauge configurations

$$\langle O\left(U,\psi,\bar{\psi}\right)\rangle = \lim_{N\to\infty}\frac{1}{N}\sum_{i=1}^{N}\langle O\rangle_{\mathrm{F}}(U_i). \tag{3.17}$$

3.2 Measuring physical quantities on the lattice

In lattice QCD, the measurement of physical quantities is performed through computing the Euclidean correlators of operators. Let O_1 and O_2 be two Euclidean operators. We have

$$\begin{aligned}\langle 0|O_1(t)O_2(0)|0\rangle &= \sum_n \langle 0|O_1(t)|n\rangle\langle n|O_2(0)|0\rangle &(3.18)\\ &= \sum_n \langle 0|e^{Ht}O_1(0)e^{-Ht}|n\rangle\langle n|O_2(0)|0\rangle &(3.19)\\ &= \sum_n \langle 0|O_1(0)|n\rangle\langle n|O_2(0)|0\rangle e^{-E_n t}, &(3.20)\end{aligned}$$

where H is the Hamiltonian, $|n\rangle$ represents a complete set of eigenstates, and E_n is the energy of state $|n\rangle$. In the first line, we insert a complete set of eigenstates that have non-zero overlap with two operators. In the second line, we use the following properties of Euclidean operators under time translation

$$O(t) = e^{Ht}\ O(0)\ e^{-Ht}. \tag{3.21}$$

Because of the exponential factor in Equation 3.20, as time separation of the two operators approaches infinity, the value of the correlator will be dominated by the ground state with lowest energy, denoted by m, and the excited states with higher energies will be exponentially suppressed compared to the ground state

$$\langle 0|O_1(t)O_2(0)|0\rangle \overset{t\to\infty}{\to} \langle 0|O_1(0)|m\rangle\langle m|O_2(0)|0\rangle e^{-E_m t}. \tag{3.22}$$

From this expression, we can extract the energy of ground state E_m, as well as the product of matrix

elements $\langle 0|O_1(0)|m\rangle\langle m|O_2(0)|0\rangle$.

The simplest and most common example is hadron spectroscopy, i.e., computing the masses of hadrons on the lattice. The hadron interpolating operators used in this work are listed in Appendix B.1. The choice of interpolating operator is not unique and any choice is allowed as long as it has the same quantum numbers as the target hadron. We use the K^0 as an example. The point-like K^0 interpolating operator is

$$K^0(x) = i\bar{d}(x)\gamma_5 s(x). \tag{3.23}$$

An improvement of the point-like K^0 operator that has a better overlap with the zero momentum $|K^0\rangle$ ground state is the wall-like interpolating operator that spans the entire time slice

$$K^0(t) = i\sum_{\vec{x}} \bar{d}(\vec{x}, t)\gamma_5 s(\vec{x}, t). \tag{3.24}$$

An even better overlap is achieved by a non-local kaon operator in which the spatial positions of the down and anti-strange quark operators are separated as they are in a physical kaon.

Using Equation 3.22, the kaon mass can be extracted from the two point function

$$C(t) = \langle 0|\overline{K^0}(t)K^0(0)|0\rangle \overset{t\to\infty}{\to} |\langle 0|K^0(0)|m\rangle|^2 e^{-M_K t} \tag{3.25}$$

$$\equiv N_K^2 e^{-M_K t}. \tag{3.26}$$

We impose periodic boundary condition on the lattice which allows mesons to propagate through the boundary. The two-point correlation function then becomes

$$C(t) \overset{t\to\infty}{\to} N_K^2 \left(e^{-M_K t} + e^{-M_K(T-t)}\right), \tag{3.27}$$

where T is the size of the time direction.

Kaon mass can be obtained by directly fitting the two-point correlation function in the above

equation with two unknown parameters N_K and M_K, or by calculating the following effective mass at small time separations t

$$m_{\text{eff}}(t + \frac{1}{2}) = \ln \frac{C(t)}{C(t+1)}. \tag{3.28}$$

By examining the plateau region in an effective mass plot $m_{\text{eff}}(t)$ versus t, we can also learn where the contamination of the higher excited states becomes negligible due to the exponential decaying factor.

The hadronic matrix element involved in the $K_L \to \mu^+\mu^-$ decay and the $K_L \to \gamma\gamma$ decay is $\langle J_\mu(u)J_\nu(v)H_w(x)|K_L\rangle$. It can be extracted from the four-point function

$$\langle J_\mu(u)J_\nu(v)H_w(x)K_L(t_K)\rangle = \sum_n \langle J_\mu(u)J_\nu(v)H_w(x)|n\rangle\langle n|K_L(t_K)\rangle \tag{3.29}$$

$$\overset{t_K\to-\infty}{\longrightarrow} \langle J_\mu(u)J_\nu(v)H_w(x)|K_L\rangle\langle K_L|K_L(t_K)\rangle \tag{3.30}$$

$$= \langle J_\mu(u)J_\nu(v)H_w(x)|K_L\rangle N_K e^{M_K t_K}. \tag{3.31}$$

In this thesis, the normalization of infinite-volume meson states is chosen to be

$$\langle n(p)|n(q)\rangle = (2\pi)^3 2E_p \delta^3(\vec{p} - \vec{q}). \tag{3.32}$$

Under this convention, we have an extra factor of $2M_K$ from the normalization of $|K_L\rangle$ states. So we have

$$\langle J_\mu(u)J_\nu(v)H_w(x)|K_L\rangle = \lim_{t_K\to-\infty} \frac{2M_K V}{N_K} e^{-M_K t_K}\langle J_\mu(u)J_\nu(v)H_w(x)K_L(t_K)\rangle. \tag{3.33}$$

where N_K is the normalization factor of the $\hat{K}_L$ interpolation operator

$$N_K = \langle K_L(p=0)|\hat{K}_L(0)|0\rangle = \sqrt{2M_K V e^{M_K|t|}\langle 0|\hat{K}_L(t)\hat{K}_L(0)|0\rangle}, \tag{3.34}$$

where V is the number of lattice sites on each time slice.

3.3 Quark propagators

On the lattice, Green functions are calculated by contracting quark propagators. The quark propagator from spacetime point y to spacetime point x is defined as the matrix element of the inverse of the Dirac operator:

$$S(x, y) = D^{-1}(x, y), \tag{3.35}$$

where x is called the sink, y is called the source, and we have suppressed the spin and color indices. However, in practice, the lattice Dirac operator is a huge matrix and it is impossible to invert the entire matrix. Let N be the number of lattice sites in five dimensions. The size of the Dirac matrix is then $12N \times 12N$, where the factor 12 arises from the number of spin and color indices. To reduce the computational complexity, we only calculate the propagator for some special sources by solving the linear equation

$$(DS)(x) = \eta(x), \tag{3.36}$$

where $\eta(x)$ is the source vector.

The point source propagator is computed by choosing the source vector to be a delta function

$$(DS)(x) = \delta_{x,x_0}, \text{ where } \delta_{x,x_0} = \begin{cases} 1, \text{ if } x = x_0 \\ \\ 0, \text{ otherwise} \end{cases} . \tag{3.37}$$

Solving this equation gives us one matrix element of the inverse of the Dirac matrix, i.e., $S(x, x_0) = D^{-1}(x, x_0)$.

Another common type of propagator is the Coulomb gauge fixed wall source propagator, which is used in kaon and pion meson interpolating operators so that they have a larger overlap with

meson states. This wall source propagator is defined by summing over all points on the time slice of the sink

$$S(x, t_y) = \sum_{\vec{y}} D^{-1}(x; t_y, \vec{y}). \tag{3.38}$$

To compute the wall source propagator, we set the source for all the space-time points at a specific time t_0 to be 1 and set the source for all other times to be 0

$$(DS)(x) = \delta_{t,t_0}, \text{ where } \delta_{t,t_0} = \begin{cases} 1, \text{ if } t_x = t_0 \\ 0, \text{ otherwise} \end{cases}. \tag{3.39}$$

In addition, when using wall source propagators to calculate contractions, the average over gauge degrees of freedom will make the contraction zero. To solve this problem, we have to fix the gauge of the lattice configuration before computing wall source propagators. In this work, we always calculate Coulomb gauge fixed wall source propagators.

Another type of propagator used in this work is the sequential source propagator, where two propagators are connected at spacetime point z with a sum over z. To compute a sequential source propagator, we choose the source to be another propagator

$$(DS_{\text{seq}})(z) = S(z, y_0). \tag{3.40}$$

Multiplying D^{-1} on both sides, it is easy to see that the sequential propagators are basically two propagators connected together

$$S_{\text{seq}}(x, y_0) = \sum_z D^{-1}(x, z) S(z, y_0) \tag{3.41}$$

$$= \sum_z S(x, z) S(z, y_0). \tag{3.42}$$

3.3.1 CG algorithm, low mode inflation, and preconditioning

The most computationally expensive part of the lattice QCD calculation procedure is solving for the quark propagator in Equation 3.36. The most commonly used method to efficiently solve the equation is the conjugate gradient (CG) algorithm, which is a numerical algorithm for iteratively solving a system of linear equations. The CG algorithm requires that the coefficient matrix must be Hermitian and positive definite. So we convert Equation 3.36 to the following form

$$\left(D^\dagger D\right) S = D^\dagger \eta = \eta'. \tag{3.43}$$

The CG algorithm, unlike many other numerical algorithms for solving linear equations, is guaranteed to converge in N steps where N is the dimension of the matrix and sufficient precision is assumed, and the convergence rate is determined by the condition number

$$\kappa(D^\dagger D) = \frac{\text{Largest eigenvalue of } D^\dagger D}{\text{Smallest eigenvalue of } D^\dagger D}. \tag{3.44}$$

The CG algorithm converges very slowly when the smallest eigenvalue is close to 0 and the condition number is large. Thus, besides the large size of Dirac matrix D, another major difficulty in solving the propagators is the small eigenvalues in D, especially when the fermion mass in Dirac operator is close to physical light quark mass. We use the so-called low-mode-deflation method to directly subtract a certain number of eigenvectors with the smallest eigenvalues from the Dirac operator and compute their contribution to the propagator directly, and hence accelerate the convergence speed of the CG algorithm on the remaining eigenvectors.

Suppose λ_i is the i-th smallest eigenvalues of $D^\dagger D$ and h_i is the corresponding eigenvector.

Then, the matrix $D^\dagger D$ can be split into a low-mode part and a high-mode part

$$(D^\dagger D)_{\text{low}} = \sum_{i=1}^{k} \lambda_i h_i h_i^\dagger \tag{3.45}$$

$$(D^\dagger D)_{\text{high}} = D^\dagger D - \sum_{i=1}^{k} \lambda_i h_i h_i^\dagger. \tag{3.46}$$

Then, the low mode part is straightforward to solve

$$(D^\dagger D)_{\text{low}} S_{\text{low}} = \eta' \quad \rightarrow \quad S_{\text{low}} = \sum_i \frac{1}{\lambda_i} (h_i^\dagger \eta') h_i \tag{3.47}$$

For the high-mode part, the condition number of $(D^\dagger D)_{\text{high}}$ is λ_N/λ_{k+1} which can be much larger than the condition number of the original $(D^\dagger D)$, which is λ_N/λ_1. Therefore, solving the high-mode part can be much faster than solving the original equation.

The smallest eigenvalue of the Dirac operator depends on the fermion mass. In our calculation, we use the low mode deflation method for the computation of light quark propagators, where the fermion mass is small and there is considerable improvement of CG convergence rate after removing the low modes. However, for strange quark propagators whose fermion mass is large, the benefit of low mode deflation is not significant and we use the plain CG algorithm.

Another trick to speed up the calculation of propagators is to use even-odd preconditioning, which is based on the observation that when both x and y are even sites, the domain wall fermion operator $D(x, y)$ is easy to invert.

We first group the matrix elements by the parity of spacetime coordinate, i.e., $(x_1 + x_2 + x_3 + x_4)|2$:

$$D = \begin{pmatrix} M_{ee} & M_{eo} \\ M_{oe} & M_{oo} \end{pmatrix}. \tag{3.48}$$

where e standards for even index and o standard for odd index. Then, the inverse of the Shamir

DWF Dirac operator is

$$D^{-1} = \begin{pmatrix} 1 & -M_{ee}^{-1}M_{eo} \\ 0 & 1 \end{pmatrix} \begin{pmatrix} M_{ee}^{-1} & 0 \\ 0 & D_{oo}^{-1} \end{pmatrix} \begin{pmatrix} 1 & 0 \\ -M_{oe}M_{ee}^{-1} & 1 \end{pmatrix} \tag{3.49}$$

$$= \begin{pmatrix} 1 & -M_{ee}^{-1}M_{eo} \\ 0 & 1 \end{pmatrix} \begin{pmatrix} M_{ee}^{-1} & 0 \\ 0 & \left(D_{oo}^{\dagger}D_{oo}\right)^{-1} \end{pmatrix} \begin{pmatrix} 1 & 0 \\ 0 & D_{oo}^{\dagger} \end{pmatrix} \begin{pmatrix} 1 & 0 \\ -M_{oe}M_{ee}^{-1} & 1 \end{pmatrix}, \tag{3.50}$$

where

$$D_{oo} = M_{oo} - M_{oe}M_{ee}^{-1}M_{eo}. \tag{3.51}$$

Now, instead of inverting the entire Dirac matrix $D^{\dagger}D$, we just need to invert the odd sites $D_{oo}^{\dagger}D_{oo}$, whose size is twice smaller.

In this work, we use the Mobius Dirac operator instead of the Shamir Dirac operator. The only difference in preconditioning turns out to be an extra D_{-} operator

$$D^{-1} = \begin{pmatrix} 1 & -M_{ee}^{-1}M_{eo} \\ 0 & 1 \end{pmatrix} \begin{pmatrix} M_{ee}^{-1} & 0 \\ 0 & \left(D_{oo}^{\dagger}D_{oo}\right)^{-1} \end{pmatrix} \begin{pmatrix} 1 & 0 \\ 0 & D_{oo}^{\dagger} \end{pmatrix} \begin{pmatrix} 1 & 0 \\ -M_{oe}M_{ee}^{-1} & 1 \end{pmatrix} D_{-}. \tag{3.52}$$

It is straightforward to combine the low mode inflation technique with the even-odd preconditioning. Let λ_i be the eigenvalues of $D_{oo}^{\dagger}D_{oo}$ and let h_i be the corresponding eigenvectors. The low-mode and high-mode parts of the inverse Dirac operator are

$$D^{-1} = D_{\text{low}}^{-1} + D_{\text{high}}^{-1} \tag{3.53}$$

$$D_{\text{low}}^{-1} = \begin{pmatrix} 1 & -M_{ee}^{-1}M_{eo} \\ 0 & 1 \end{pmatrix} \begin{pmatrix} 0 & 0 \\ 0 & \sum_i \frac{1}{\lambda_i} h_i h_i^{\dagger} \end{pmatrix} \begin{pmatrix} 1 & 0 \\ 0 & D_{oo}^{\dagger} \end{pmatrix} \begin{pmatrix} 1 & 0 \\ -M_{oe}M_{ee}^{-1} & 1 \end{pmatrix} D_{-} \tag{3.54}$$

$$D_{\text{high}}^{-1} = \begin{pmatrix} 1 & -M_{ee}^{-1}M_{eo} \\ 0 & 1 \end{pmatrix} \begin{pmatrix} M_{ee}^{-1} & 0 \\ 0 & \left(D_{oo}^{\dagger}D_{oo}\right)^{-1} - \sum_i \frac{1}{\lambda_i} h_i h_i^{\dagger} \end{pmatrix} \begin{pmatrix} 1 & 0 \\ 0 & D_{oo}^{\dagger} \end{pmatrix} \begin{pmatrix} 1 & 0 \\ -M_{oe}M_{ee}^{-1} & 1 \end{pmatrix} D_{-}. \tag{3.55}$$

3.3.2 Random volume source propagators

For some diagrams of the matrix element $\left\langle J_\mu(u)J_\nu(v)\mathcal{H}'_W(x)|K\right\rangle$, we have to deal with quark self-loops which represent the propagators whose source and sink are on the same lattice site

$$S(x,x) = \sum_{\vec{y}} D^{-1}(x,x). \tag{3.56}$$

Since it is prohibitively expensive to invert the Dirac matrix for all sources x, we must find a way to calculate these self-loops more efficiently. In this work, we use random volume source propagators to calculate these self-loops in an approximate way.

We first generate a set of independent white noise vectors $\eta_i(x)$ that satisfies

$$\langle \eta_i(x)\eta_i^\dagger(x')\rangle = \delta_{x,x'}, \tag{3.57}$$

where x represents spacetime, color, and spin indices, and $i = 1, 2, \ldots, N_{\text{hits}}$. Here, N_{hits} is the number of white noise random vectors for each configuration and is called the number of random hits. Then, the self-loops can be re-written as

$$D^{-1}(x,x) = \sum_{x'} D^{-1}(x,x')\delta_{x,x'} \tag{3.58}$$

$$\approx \frac{1}{N_{\text{hits}}} \sum_{x'}\sum_{i} D^{-1}(x,x')\eta_i(x)\eta_i^\dagger(x'). \tag{3.59}$$

We introduce the notations of v and w vectors:

$$v_i(x) = D^{-1}(x,x')\eta_i(x') \tag{3.60}$$

$$w_i(x) = \eta_i(x), \tag{3.61}$$

where w vectors are simply the noise vector, and v vectors can be obtained by solving the following

linear equations with noise vectors as sources:

$$D(x, x')v_i(x') = \eta_i(x').$$

Finally, the self-loops can be approximately calculated from v and w vectors

$$D^{-1}(x, x) = \frac{1}{N_{\text{hits}}} \sum_i v_i(x) w_i^\dagger(x). \tag{3.62}$$

To reduce the noise and accelerate the convergence, we use the deflation technique and use the eigenvectors with small eigenvalues to construct the low mode part of the Dirac operator and only approximate the high energy part with random vectors. Let λ_i be the i-th smallest eigenvalue of the Dirac operator, h_i be the corresponding eigenvector, and N_{ev} be the number of eigenvectors used for deflation. We have

$$D^{-1}_{\text{deflate}} \equiv D^{-1} - \sum_{i=1}^{N_{\text{ev}}} \frac{h_i h_i^\dagger}{\lambda_i} \tag{3.63}$$

$$D^{-1} = \sum_{i=1}^{N_{\text{ev}}} \frac{h_i h_i^\dagger}{\lambda_i} + \frac{1}{N_{\text{hits}}} \sum_{x'} \sum_i D^{-1}_{\text{deflate}}(x, x') \eta_i(x) \eta_i^\dagger(x'). \tag{3.64}$$

We define the low modes and high modes of v/w vectors separately and define them as

$$v_{\text{low},i} = \frac{1}{\lambda_i} h_i, \quad w_{\text{low},i} = h_i, \text{ where} 1 \le i \le N_{\text{ev}} \tag{3.65}$$

$$v_{\text{high},i} = D^{-1}_{\text{deflate}} \eta_i, \quad w_{\text{high},i} = \eta_i, \text{ where} 1 \le i \le N_{\text{hits}}. \tag{3.66}$$

Furthermore, with even-odd preconditioning, as discussed in the Section 3.3.1, we calculate eigenvalue and eigenvectors of $D^\dagger_{oo} D_{oo}$, denoted as λ_i and h_i. Then, we define the v and w vectors

based on Equation 3.54 and Equation 3.55. The low modes are

$$v_i = \frac{1}{\lambda_i}\begin{pmatrix} -M_{ee}^{-1} M_{eo} h_i \\ h_i \end{pmatrix} \tag{3.67}$$

$$w_i = D_-^\dagger \begin{pmatrix} -M_{ee}^{-1,\dagger} M_{oe}^\dagger D_{oo} h_i \\ D_{oo} h_i \end{pmatrix}. \tag{3.68}$$

The high modes are

$$v_i = D_{\text{deflate}}^{-1} \eta_i \tag{3.69}$$

$$w_i = \eta_i, \tag{3.70}$$

where the D_{deflate} now is the high-mode part of preconditioned Dirac operator as defined in Equation 3.55.

In this thesis, we use zMobius eigenvectors in place of Mobius eigenvectors, which introduces no bias into the resulting all-to-all propagator. The zMobius Dirac operator is a five-dimensional Dirac operator with complex coefficients appearing in the derivatives in the s direction. It allows us to approximate a large-L_s Mobius domain wall operator by a small-L_s zMobius domain wall operator, achieving nearly a factor of two speedup in the Direc operator inversion. We denote the smaller-L_s space for zMobius operator with label $5'$, and the larger-L_s space for Mobius operator with label 5. Then, the Dirac operator can be decomposed in the following way:

$$\begin{aligned} \left[D^{-1}\right]^4 = &\sum_i V^{45'} \left[\frac{1}{\lambda_i} h_i h_i^\dagger\right]^{5'} U^{5'4} \\ &- \sum_i V^{45'} \left[\frac{1}{\lambda_i} h_i h_i^\dagger\right]^{5'} U^{5'4} \sum_{j=1}^{N_h} \eta_j \eta_j^\dagger \\ &+ V^{45} \left[D^{-1}\right]^5 U^{54} \sum_{j=1}^{N_h} \eta_j \eta_j^\dagger. \end{aligned} \tag{3.71}$$

where h_i is the zMobius eigenvector, N_h is the number of high modes, matrix U^{54} converts a 4D

vector into a 5D vector by projecting out the left and right handed components and poking onto the corresponding walls and matrix V^{45} performs the inverse procedure

$$U^{54}\chi = \begin{pmatrix} P_R \\ 0 \\ \vdots \\ 0 \\ P_L \end{pmatrix} \chi \tag{3.72}$$

$$V^{45}\Psi = (P_L, 0, \ldots, 0, P_R)\,\Psi = P_L\Psi_0 + P_R\Psi_{L_s-1}. \tag{3.73}$$

Equation 3.71 is an unbiased estimation of the Dirac operator because the first two terms cancel each other as the number of high modes becomes large and the equation reduces to

$$\lim_{N_h\to\infty}\left[D^{-1}\right]^4 = V^{45}\left[D^{-1}\right]^5 U^{54}. \tag{3.74}$$

With preconditioning, the low modes are

$$v_i = V^{45'}\frac{1}{\lambda_i}\begin{pmatrix} -M_{ee}^{-1}M_{eo}M_{oo}^{-1}h_i \\ M_{oo}^{-1}h_i \end{pmatrix} \tag{3.75}$$

$$w_i = U^{5'4\dagger}D_-^{\dagger}\begin{pmatrix} -M_{ee}^{-1,\dagger}M_{oe}^{\dagger}D_{oo}h_i \\ D_{oo}h_i \end{pmatrix}. \tag{3.76}$$

The high modes are

$$v_i = V^{45}\left[D^{-1}\right]^5 D_-U^{54}\eta_i \tag{3.77}$$

$$- V^{45'}\begin{pmatrix} 1 & -M_{ee}^{-1}M_{eo} \\ 0 & 1 \end{pmatrix}\begin{pmatrix} 0 & 0 \\ 0 & \sum_i \frac{1}{\lambda_i}h_ih_i^{\dagger} \end{pmatrix}\begin{pmatrix} 1 & 0 \\ -M_{oe}M_{ee}^{-1}D_{oo}^{\dagger} & D_{oo}^{\dagger} \end{pmatrix} D_-U^{5'4}\eta_i \tag{3.78}$$

$$w_i = \eta_i. \tag{3.79}$$

3.4 Wilson coefficients and non-perturbative renormalization

The Wilson coefficients $C_i(\mu)$ in Section 2.2 incorporates the contribution of short-distance interaction from heavy particles. The values of the Wilson coefficients are known in the $\overline{\text{MS}}$ scheme [7]. In this section, we discuss the non-perturbative renormalization (NPR) procedure of determining the conversion matrix from the lattice operators to the operators in the $\overline{\text{MS}}$ scheme.

The first step is to replace the 10, linearly dependent lattice operators Q_{1-10} with a new basis of 7 linearly independent operators Q'_{1-7}. The conventional seven independent operators Q'_{1-7} can be defined in terms of the original ten dependent operators by the equations:

$$Q'_1 = 3Q_1 + 2Q_2 - Q_3 \tag{3.80}$$

$$Q'_2 = \frac{1}{5}(2Q_1 - 2Q_2 + Q_3) \tag{3.81}$$

$$Q'_3 = \frac{1}{5}(-3Q_1 + 3Q_2 + Q_3) \tag{3.82}$$

$$Q'_4 = Q_5 \tag{3.83}$$

$$Q'_5 = Q_6 \tag{3.84}$$

$$Q'_6 = Q_7 \tag{3.85}$$

$$Q'_7 = Q_8. \tag{3.86}$$

As discussed in Section 2.2, we only calculate Q_1 and Q_2 which can be expressed with the 7 linearly independent operators as follows:

$$Q_1 = \frac{1}{5}Q'_1 + Q'_2 \tag{3.87}$$

$$Q_2 = \frac{1}{5}Q'_1 + Q'_3. \tag{3.88}$$

The NPR procedure is performed with the aid of an intermediate scheme, the regularization-independent (RI) scheme [8]. There are four different types of RI/SMOM schemes: the $(\not{q}, \not{q})$ scheme, the (γ_μ, γ_μ), the $(\not{q}, \gamma_\mu)$ scheme, and the $(\gamma_\mu, \not{q})$ scheme. The first $\not{q}$ or γ_μ represents the

projection operator used to define the operator renormalization and the second $\not{q}$ or γ_μ represents the projection operator we use in the wave function renormalization. In this work, we only use the $(\not{q}, \not{q})$ scheme.

The conversion matrix from lattice operators Q'^{lat} to operators in RI/SMOM scheme has to be calculated on the lattice. We denote the conversion matrix as $Z^{\text{RI}\leftarrow\text{lat}}$

$$Q_i^{\text{RI}} = \sum_j \left(Z^{\text{RI}\leftarrow\text{lat}}\right)_{7\times7,ij} Q_j'^{\text{lat}}. \tag{3.89}$$

The RI operators are defined by requiring that when inserted into five point functions with four gauge-fixed off-shell external quark lines the resulting Greens functions when evaluated at an energy scale μ have a specific from, usually equal to the correlation function F that would be obtain in free field theory. The conversion matrix is calculated by

$$Z^{\text{RI}\leftarrow\text{lat}} = Z_q^2 F M^{-1}, \tag{3.90}$$

where Z_q is the quark wave function renormalization constant and is used to renormalize the external quark fields of the four-quark Green's function, and M is the amputated correlation function made up of the lattice operators. Both Z_q and M require numerical calculation on the lattice.

Then, the conversion from RI/SMOM scheme operators to $\overline{\text{MS}}$ scheme operators are worked out in [9]

$$Q_i^{\overline{\text{MS}}} = \sum_j \left[\left(T + \Delta T_I^{\overline{\text{MS}}}\right)_{10\times7} \left(1 + \Delta r^{\overline{\text{MS}}\leftarrow\text{RI}}\right)_{7\times7}\right]_{ij} Q_j^{\text{RI}}, \tag{3.91}$$

where $\Delta r^{\overline{\text{MS}}\leftarrow\text{RI}}$ is computed at one loop and can be found in Tab. XI of the reference [9]. The other two constant matrices T and $\Delta T_I^{\overline{\text{MS}}}$ are used to express the operators in the 10 operator basis in terms of the operators in the 7 operator basis and are given in Equation 59 and 65 of that reference. The expression of $\Delta r^{\overline{\text{MS}}\leftarrow\text{RI}}$ involves the QCD coupling constant $\alpha_s(\mu)$. At two-loop order, the

solution of renormalization group equation for $\alpha_s^f(\mu)$ is [10]

$$\alpha_s^f(\mu) = \frac{4\pi}{\beta_0 \ln\left(\mu^2/\Lambda_f^2\right)}\left(1 - \frac{\beta_1}{\beta_0^2}\frac{\ln\ln\left(\mu^2/\Lambda_f^2\right)}{\ln\left(\mu^2/\Lambda_f^2\right)}\right),$$

where f is the number of flavors, Λ_f is the QCD energy scale and is dependent on the number of flavors, and β_0 and β_1 are two constants

$$\beta_0 = \frac{11N_c - 2f}{3} \tag{3.92}$$

$$\beta_1 = \frac{34}{3}N_c^2 - \frac{10}{3}N_c f - \frac{N_c^2 - 1}{N_c}f. \tag{3.93}$$

The QCD energy scale in five-flavor theory Λ_5 is determined from the known value of the coupling constant in five-flavor theory at the energy scale of M_Z. The value in the PDG table [11] is $\alpha_s^{(5)}(M_Z) = 0.1179$. The four-flavor theory Λ_4 is determined by requiring that the values of coupling constant at the bottom quark mass are the same for four-flavor and five-flavor theories, i.e. $\alpha_s^{(4)}(M_b) = \alpha_s^{(5)}(M_b)$. After obtaining Λ_4, the three-flavor theory Λ_e is determined by requiring that the values of coupling constant at charm quark mass are the same for three-flavor and four-flavor theories, i.e. $\alpha_s^{(3)}(M_c) = \alpha_s^{(4)}(M_c)$. The following set of equations sums up this process

$$\alpha_s^{(5)}(M_Z) = 0.1179 \Rightarrow \Lambda_5 = 0.2250 \text{ GeV} \tag{3.94}$$

$$\alpha_s^{(5)}(M_b) = \alpha_s^{(4)}(M_b) \Rightarrow \Lambda_4 = 0.3217 \text{ GeV} \tag{3.95}$$

$$\alpha_s^{(4)}(M_c) = \alpha_s^{(3)}(M_c) \Rightarrow \Lambda_3 = 0.3673 \text{ GeV}. \tag{3.96}$$

After obtaining Λ_3, the QCD coupling constant $\alpha_s^{(3)}(\mu)$ can be calculated for any energy scale based on Equation 3.92. In this work, we choose to use $\mu = 4.00$ GeV to calculate the Wilson coefficient. So we have

$$\alpha_s^{(3)}(4.00 \text{ GeV}) = 0.2167. \tag{3.97}$$

Table 3.1: Input parameters for the calculation of the QCD coupling constant α_s

M_Z	91.1876 GeV
M_b	4.18 GeV
M_c	1.275 GeV
$\alpha_s^{(5)}(M_Z)$	0.1179
Λ_5	0.2250 GeV
Λ_4	0.3217 GeV
Λ_3	0.3673 GeV
$\alpha_s^{(3)}(4.00\ \text{GeV})$	0.2167

The input constant parameters used for calculating the QCD coupling constant α_s are listed in Table 3.1.

In conclusion, the complete procedure of converting the seven lattice operators $Q_i'^{\text{lat}}$ to the ten operators in the $\overline{\text{MS}}$ scheme can be expressed by the following equation

$$Q_i^{\overline{\text{MS}}} = \sum_j \left[\left(T + \Delta T_I^{\overline{\text{MS}}} \right)_{10\times7} \left(1 + \Delta r^{\overline{\text{MS}}\leftarrow\text{RI}} \right)_{7\times7} \left(Z^{\text{RI}\leftarrow\text{lat}} \right)_{7\times7} \right]_{ij} Q_j'^{\text{lat}} \tag{3.98}$$

$$\equiv \sum_j \left[\left(Z^{\overline{\text{MS}}\leftarrow\text{lat}} \right)_{10\times7} \right]_{ij} Q_j'^{\text{lat}}. \tag{3.99}$$

Therefore, the lattice Wilson coefficients can be calculated from the Wilson coefficients in the $\overline{\text{MS}}$ scheme

$$C_j'^{\text{lat}} = \sum_i C_i^{\overline{MS}} \left[\left(Z^{\overline{MS}\leftarrow\text{lat}} \right)_{10\times7} \right]_{ij}. \tag{3.100}$$

In this work, the ensemble for which we calculated the Wilson coefficients is the 24ID ensemble. We calculate the conversion matrix $Z^{\text{RI}\leftarrow\text{lat}}$ at the energy scale $\mu = 1.24$ GeV. Although the NPR renormalization is meaningful at all energy scales, the switch between NPR and $\overline{\text{MS}}$ and the $\overline{\text{MS}}$ renormalization itself relies on perturbation theory and is thus best done at a high energy scale. Thus, we use another 32IF ensemble to transit the energy scale from 1.24 GeV to 4 GeV. This

procedure is called step scaling. The final conversion matrix is

$$Z^{\mathrm{RI}\leftarrow\mathrm{lat}}(4\ \mathrm{GeV}, 24\mathrm{ID}) = Z^{\mathrm{RI}\leftarrow\mathrm{lat}}(4\ \mathrm{GeV}, 32\mathrm{I}) \left[Z^{\mathrm{RI}\leftarrow\mathrm{lat}}(1.24\ \mathrm{GeV}, 32\mathrm{I})\right]^{-1} Z^{\mathrm{RI}\leftarrow\mathrm{lat}}(1.24\ \mathrm{GeV}, 24\mathrm{ID}). \tag{3.101}$$

Finally, we obtain the following values of Wilson coefficients for the 24ID ensemble and for the RI/SMOM($\not{q}, \not{q}$) scheme

$$C_1 = -0.5746(2) \tag{3.102}$$

$$C_2 = 1.3278(2), \tag{3.103}$$

where the numbers in the parenthesis are the statistical errors.

3.5 Jackknife resampling for estimating statistical errors

The jackknife resampling method is a widely used statistical method for estimating the standard deviation of an estimated parameter.

Suppose we have a sample of n data points, $S = (x_1, \ldots, x_N)$, and get an estimator $\hat{\theta} = f(S)$ of the true parameter θ. The jackknife resampling method works in the following procedure

1. Generate N jackknife samples by leaving out one sample at a time.

$$S_i = (x_1, x_2, \ldots, x_{i-1}, x_{i+1} \ldots, x_N), \text{ for } 1 \leq i \leq N. \tag{3.104}$$

2. Calculate N estimators based on each Jackknife sample

$$\hat{\theta}_i = f(S_i), \text{ for } 1 \leq i \leq N. \tag{3.105}$$

3. The variance of the estimator is then

$$s^2_{\hat{\theta}} = \frac{N-1}{N} \sum_{i=1}^{N} (\hat{\theta}_i - \hat{\theta}_{(.)})^2. \tag{3.106}$$

where

$$\hat{\theta}_{(.)} = \frac{1}{N} \sum_{i=1}^{N} \hat{\theta}_i. \tag{3.107}$$

Chapter 4: Calculating the $\pi^0 \to e^+e^-$ decay amplitude

In this chapter, we discuss the calculation of $\pi^0 \to e^+e^-$ as a first step toward the calculation of the two-photon component of $K_L \to \mu^+\mu^-$ decay. As a step in this direction, we have developed a new method that can be directly applied to the decay $\pi^0 \to e^+e^-$ to compute both the real and imaginary parts of the amplitude of this simper decay process [12].

This chapter is organized as follows. In Section 4.1, we review the basics of the $\pi^0 \to e^+e^-$ decay, including the status of current experimental and theoretical results, and the real and imaginary part of the decay amplitude. The imaginary part of the decay amplitude can be obtained from the optical theorem with an on-shell two-photon state, while the first-principles calculation of the real part requires lattice methods. In Section 4.2, we develop an analytic continuation method to deal with the intermediate two-photon state which is the major difficulty in the lattice calculation of the $\pi^0 \to e^+e^-$ decay. The decay amplitude is then decomposed into a leptonic part and a hadronic part. In Section 4.3, we develop strategies to calculate the hadronic matrix element on the lattice and to handle the disconnected diagram. In Section 4.4, we work out the analytic formula for the leptonic part. In Section 4.5, we present the lattice calculation result of the $\pi^0 \to e^+e^-$ decay amplitude and compare it with experiment values.

4.1 Overview of the $\pi^0 \to e^+e^-$ decay

The neutral pion, as the lightest hadron in the standard model, has played an important role in the development of particle physics. The neutral pion decay is completely dominated by the two-photon mode with branching ratio $B(\pi^0 \to \gamma\gamma) = 0.988$. The theoretical prediction of the

$\pi^0 \to \gamma\gamma$ decay width is

$$\Gamma(\pi^0 \to \gamma\gamma) = \frac{1}{4}\pi\alpha^2 M_\pi^3 F_{\pi\gamma\gamma}^2. \tag{4.1}$$

At the leading order of chiral perturbation theory, the form factor $F_{\pi\gamma\gamma}$ is given by

$$F_{\pi\gamma\gamma} = \frac{\sqrt{2}}{4\pi^2 f_\pi}, \tag{4.2}$$

where $f_\pi \approx 132$ MeV is referred to as the pion decay constant. This formula is exact in the chiral limit where the u and d quarks are massless.

In this chapter, we study the rare decay of the neutral pion into a dielectron. Its decay amplitude is much smaller than the main mode $\pi^0 \to \gamma\gamma$ because it involves a second-order QED process. In addition, the $\pi^0 \to e^+e^-$ decay is helicity-suppressed because the final state electron and positron have the same helicity due to momentum conservation and angular momentum conservation. Thus, the decay amplitude is suppressed by an additional factor of $\frac{m_e}{m_\pi}$.

The $\pi^0 \to e^+e^-$ decay rate was well measured in the KTeV experiment at Fermilab in 2007. After the elaborate reanalysis of radiative corrections [13][14], the experimental branching ratio of this decay is

$$B(\pi^0 \to e^+e^-) = (6.87 \pm 0.36) \times 10^{-8}. \tag{4.3}$$

The theoretical prediction of this decay rate was first proposed in 1958 [15], and has been improved in the later decades. However, so far the experimental result is still larger than many theoretical results [16], like the result from dispersion relations, by the order of 2σ.

The rare pion decay $\pi^0 \to e^+e^-$ decay is dominated by the electromagnetic contribution that is mediated by two virtual photons $\pi^0 \to \gamma^*\gamma^* \to e^+e^-$ as shown in the QED one-loop diagram in Figure 4.1. The $\pi^0 \to e^+e^-$ decay also has weak interactions contributions that is mediated by Z^0 boson. However, these are many orders of magnitude smaller than the electromagnetic two-photon

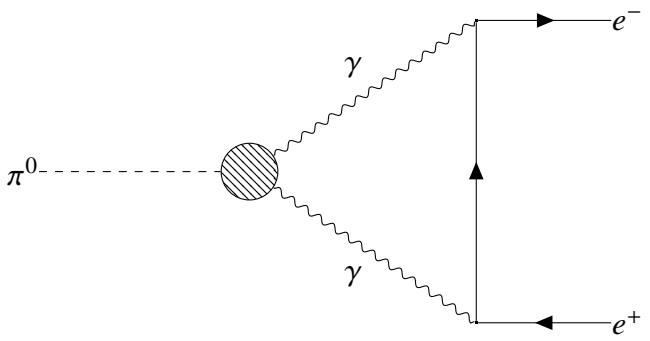

Figure 4.1: The electromagnetic contribution to the $\pi^0 \to e^+e^-$ decay mediated by two photons. The blob represents the pion transition form factor that is not analytically known and requires lattice calculations.

contribution and is negligible [17]

$$\frac{\Gamma_{\pi^0 \to Z^0 \to e^+e^-}}{\Gamma_{\pi^0 \to \gamma\gamma}} = 9\left(\frac{G_F}{4\pi\alpha}\right)(m_e m_\pi)^2 \approx 10^{-15}. \tag{4.4}$$

Therefore, in this work, we only consider the leading-order electromagnetic contribution.

We use $\mathcal{A}$ to denote the $\pi^0 \to e^+e^-$ decay amplitude. The transition amplitude and the decay width are then

$$\langle e^+(k_+)e^-(k_-)|\pi^0(P)\rangle = (2\pi)^4\delta^4(P - k_- - k_+)i\mathcal{A}. \tag{4.5}$$

$$\Gamma(\pi^0 \to e^+e^-) = \frac{\beta}{8\pi M_\pi}|\mathcal{A}|^2, \text{ where } \beta = \sqrt{1 - \frac{4m_e^2}{M_\pi^2}}, \tag{4.6}$$

where m_e is the mass of electron and M_π is the mass of pion.

The decay amplitude is composed of an imaginary part and a real part $\mathcal{A} = \mathcal{A}_{\text{real}} + i\mathcal{A}_{\text{imag}}$. The imaginary part can be obtained using the optical theorem where we cut the two virtual photon lines in Figure 4.1 and split the diagram into two separate diagrams with on-shell photons. Then, the imaginary part of the decay amplitude will be equal to the product of these two diagrams. We obtain the following result

$$\mathcal{A}_{\text{imag}} = \pi m_e M_\pi \alpha^2 F_{\pi\gamma\gamma}\frac{1}{\beta}\ln\frac{1-\beta}{1+\beta}, \tag{4.7}$$

where $F_{\pi\gamma\gamma}$ is the pion transition form factor in Equation 4.2. Plugging it into Equation 4.6, the imaginary part contribution to the decay width is

$$\Gamma(\pi^0 \to e^+e^-)_{\text{imag}} = \frac{1}{8}\pi m_e^2 M_\pi \alpha^4 F^2 \frac{1}{\beta}\left(\ln\frac{1-\beta}{1+\beta}\right)^2. \tag{4.8}$$

The contribution of the imaginary part gives us a lower bound of the branching ratio of the $\pi^0 \to e^+e^-$ decay

$$R \equiv \frac{\Gamma(\pi^0 \to e^+e^-)}{\Gamma(\pi^0 \to \gamma\gamma)} \geq \frac{\Gamma(\pi^0 \to e^+e^-)_{\text{imag}}}{\Gamma(\pi^0 \to \gamma\gamma)} \tag{4.9}$$

$$= \frac{1}{2}\alpha^2\left(\frac{m_e}{M_\pi}\right)^2 \frac{1}{\beta}\left(\ln\frac{1-\beta}{1+\beta}\right)^2 \tag{4.10}$$

$$= 4.75 \times 10^{-8}. \tag{4.11}$$

This lower bound is commonly referred to as the unitarity bound. It is also model-independent because the dependence on the pion transition form factor has been canceled in the ratio.

4.2 Analytic continuation

Even though the imaginary part of the $\pi^0 \to e^+e^-$ decay amplitude can be directly obtained from the optical theorem, the real part is more complicated and requires the lattice method for a first-principles calculation. In this section, we develop an analytic continuation method to calculate the entire decay amplitude including both the real part and the imaginary part on the lattice.

We start by writing down the usual expression for the $\pi^0 \to e^+e^-$ decay in Minkowski space where the assignment of the variables is indicated in Figure 4.2. The conventional Minkowski-space decay amplitude can be decomposed into leptonic and hadronic pieces, explicitly integrated over the average positions of the two hadronic and the two leptonic E&M currents to impose four-momentum conservation and the result written as a combination of position and momentum

integrals:

$$\begin{aligned}\mathcal{A} &= \int d^4w\, \langle 0|T\{J_\mu(\tfrac{w}{2})J_\nu(-\tfrac{w}{2})\}|\pi^0\rangle \\ &\int d^4p e^{-ip\cdot w}\left[\frac{g_{\mu\mu'}}{(p+\frac{P}{2})^2+m_\gamma^2-i\epsilon}\right]\left[\frac{g_{\nu\nu'}}{(p-\frac{P}{2})^2+m_\gamma^2-i\epsilon}\right] \\ &\overline{u}(k_-)\gamma_{\mu'}\left[\frac{\gamma\cdot(p+\frac{P}{2}-k_-)+m_e}{(p+\frac{P}{2}-k_-)^2+m_e^2-i\epsilon}\right]\gamma_{\nu'}v(k_+).\end{aligned} \tag{4.12}$$

Here all expressions, including the matrix element $\langle 0|T\{J_\mu(\frac{w}{2})J_\nu(-\frac{w}{2})\}|\pi^0\rangle$ are intended to be standard Minkowski-space quantities with the metric (1,1,1,-1). We have chosen to hold the average position of the two hadronic E&M currents in Eq. (4.12) fixed at the origin so that the overall energy and momentum conserving delta function has been removed. We have also introduced $k_\pm$ as the four-momenta of the e^+ and e^- while P is the four-momentum of the π^0.

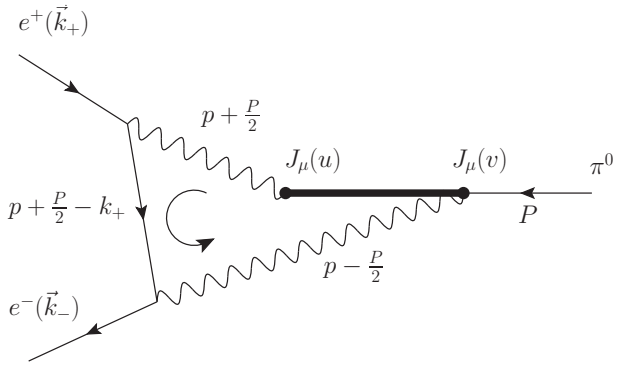

Figure 4.2: The diagram showing the two-photon contribution to the $\pi^0 \to e^+e^-$ decay amplitude. The assignment of momenta corresponds to that used in the expression for the decay amplitude given in Eq. (4.12).

While Eq. (4.12) is a correct expression for the $\pi^0 \to e^+e^-$ decay amplitude $\mathcal{A}$, the appearance of the Minkowski-space hadronic amplitude $\langle 0|T\{J_\mu(\frac{w}{2})J_\nu(-\frac{w}{2})\}|\pi^0\rangle$ prevents a direct evaluation using lattice QCD. However, if the integration contour for the time variable w_0 could be rotated so that instead of w_0 following the real axis, the complex contour $w_0e^{-i\phi}$ is followed where w_0 remains real but the angle ϕ is increased from zero to $\pi/2$, then the hadronic matrix element would become a Euclidean quantity which can be computed in lattice QCD. Because of the simple form

of the hadronic matrix element and the explicit expression given in Eq. (4.12) this transformation from a Minkowski- to a Euclidean-space quantity is not difficult to achieve.

We will first examine the hadronic matrix element by writing out the time ordering explictly and introducing a sum over a complete set of intermediate states:

$$\begin{aligned}
\langle 0|T\left\{J_\mu(u)J_\nu(v)\right\}|\pi^0\rangle &= \sum_n \Big\{\langle 0|J_\mu(u)|n\rangle\,\langle n|J_\nu(v)|\pi^0\rangle\theta(u_0-v_0) \\
&\qquad +\langle 0|J_\nu(v)|n\rangle\,\langle n|J_\mu(u)|\pi^0\rangle\theta(v_0-u_0)\Big\} \\
&= e^{iP\cdot W}\sum_n \Big\{\langle 0|J_\mu(0)|n\rangle\,\langle n|J_\nu(0)|\pi^0\rangle e^{iw\cdot(P_n-P/2)}\theta(w_0) \\
&\qquad +\langle 0|J_\nu(0)|n\rangle\,\langle n|J_\mu(0)|\pi^0\rangle e^{-iw\cdot(P_n-P/2)}\theta(-w_0)\Big\}, \qquad (4.13)
\end{aligned}$$

where we have introduced the Minkowski four-vectors $W = (u+v)/2$ and $w = u - v$ and used P_n to represent the momentum four-vector for the state $|n\rangle$. Note, the hadronic matrix element $\langle 0|T\left\{J_\mu\left(\frac{w}{2}\right)J_\nu\left(-\frac{w}{2}\right)\right\}|\pi^0\rangle$ in Eq. (4.12) can be obtained from Eq. (4.13) if we change the space-time integration variables from u and v to W and w and set $W = 0$.

As can be seen from Eq. (4.13), the time component w_0 enters the hadronic matrix element in the complex exponent $e^{-iw_0(E_n-m_\pi/2)}$ if $w_0 > 0$ and as $e^{iw_0(E_n-m_\pi/2)}$ for $w_0 < 0$. Thus, both factors will fall exponentially for large $|w_0|$ if we rotate the w_0 integration contour as described above. However, we must also consider the second exponential factor that appears in the expression for the complete amplitude given in Eq. (4.12): $e^{ip_0w_0}$. Without taking further steps, this factor will introduce exponential growth which for sufficiently large values of the integration variable p_0 will result in diverging behavior for the integral over w_0.

Of course, this behavior can be avoided if the p_0 contour is Wick rotated with a compensating phase so that for large p_0 the p_0 contour follows the path $p_0e^{i\pi}$, at least for large $|p_0|$. Here the variable p_0 is taken to be real and the angle ϕ is the same as that appearing in the definition of the Wick-rotated w_0 contour: $w_0 \rightarrow w_0e^{-i\phi}$. Increasing ϕ to $\pi/2$ results in an explicit amplitude in which the hadronic matrix element $\langle 0|J_\mu\left(\frac{w}{2}\right)J_\nu\left(-\frac{w}{2}\right)|\pi^0\rangle$ is now evaluated in Euclidean space and can be directly computed using lattice QCD.

The actual p_0 contour C shown in Figure 4.3 does not precisely follow the imaginary axis. This implies that for portions of the p_0 contour the exponent in the factor $e^{iw_0p_0}$ in Eq. (4.12) will not be purely imaginary and an exponentially growing behavior as w_0 increases will appear. For this Wick rotation to be possible, it is necessary that this exponential growth be overcome by the exponential fall-off coming from the w_0 behavior of the Euclidean-space hadronic matrix element. As can be seen from Figure 4.3 this exponential growth of the electron-photon amplitude is minimized when the p_0 contour is routed as close to the poles $m_\pi/2 - |\vec{p}|$ and $-m_\pi/2 + |\vec{p}|$ as possible. Thus, the matrix element $\langle 0|T\{J_\mu(\frac{w}{2})J_\nu(-\frac{w}{2})\}|\pi^0\rangle$ must fall more rapidly than $e^{-m_\pi|w_0|/2}$ for large w_0 if the Wick-rotated integral over w_0 is to converge. Fortunately, the lightest intermediate state which can appear in this hadronic matrix element is the two-pion state so the resulting exponential decrease is $e^{-3m_\pi/2|w_0|}$ which is sufficient to guarantee convergence.

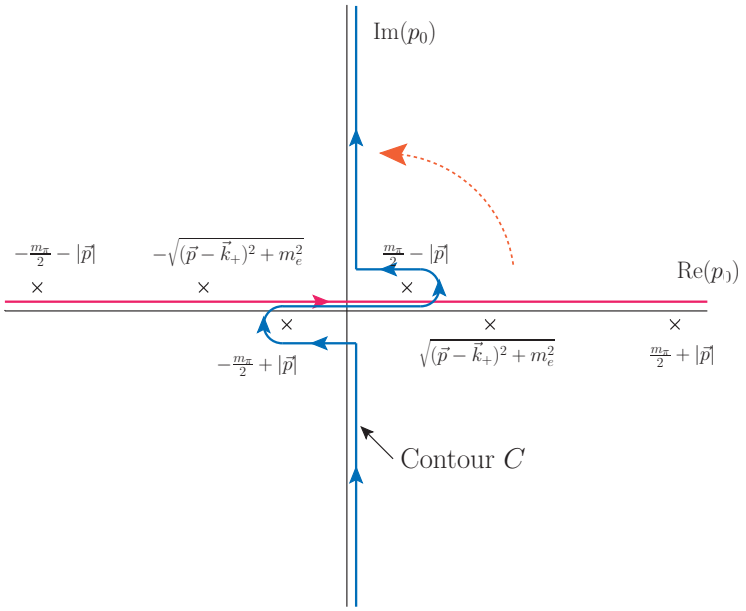

Figure 4.3: A diagram of the complex p_0 plane showing the Minkowski p_0 contour before the analytic continuation (the horizontal black line) and a possible choice of contour after the analytic continuation (the blue line). The six crosses correspond to the six poles of the integrand on the right hand side of Eq. (4.12).

The conventional Minkowski-space amplitude that appears in the second and third lines of Eq. (4.12) is little changed in this procedure. The only effect is that the p_0 contour is rotated from the usual integration along the real axis into the more elaborate contour shown in Figure 4.3. This

procedure does not change the value of the final decay amplitude and the result will continue to be complex with the imaginary part given by the optical theorem. Thus, with what is an application of Cauchy's theorem we have Wick-rotated the integral over w_0 so that the hadronic matrix element is now evaluated in Euclidean space. The result can be written:

$$\begin{aligned}\mathcal{A} &= e^4 \int d^4w \, \langle 0|T\{J_\mu(\frac{w}{2})J_\nu(-\frac{w}{2})\}|\pi^0\rangle_E \\ &\int d^3p \int_C dp_0 e^{-i\vec{p}\cdot\vec{w}} e^{+p_0 w_0} \left[\frac{\widetilde{g}_{\mu\mu'}}{(p+\frac{P}{2})^2 - i\epsilon}\right]\left[\frac{\widetilde{g}_{\nu\nu'}}{(p-\frac{P}{2})^2 - i\epsilon}\right] \\ &\overline{u}(k_-)\gamma_{\mu'}\left[\frac{\gamma\cdot(p+\frac{P}{2}-k_-)+m_e}{(p+\frac{P}{2}-k_-)^2+m_e^2-i\epsilon}\right]\gamma_{\nu'}v(k_+).\end{aligned} \tag{4.14}$$

In this equation, the subscript E on the hadronic matrix element indicates that it is evaluated using Euclidean time dependence and conventions. The diagonal metric tensor $\widetilde{g}_{\mu\mu'}$ with elements $(1, 1, 1, i)$ has been introduced to correctly connect the Minkowski conventions for the E&M currents in the electron and photon part of the expression with the Euclidean conventions used in the hadronic matrix element. The p_0 contour to be used in Eq. (4.14) is that labeled C in Figure 4.3. Note for large p_0 factor $e^{+p_0 w_0}$ in Eq. (4.14) contains an imaginary exponent and oscillates with no exponential growth.

Finally, we should observe that the analytic portion of the result given in Eq. (4.14) appears to be straightforward to evaluate. We begin by expressing the right-hand side of this equation as the space-time integral of the product of leptonic and hadronic factors:

$$\mathcal{A} = \int d^4w L_{\mu\nu}(w) H_{\mu\nu}(w). \tag{4.15}$$

Here the four integration variables are real and integrated over infinite volume. The two factors in

this equation are given by:

$$L_{\mu\nu}(w) = e^4 \int d^3p \int_C dp_0 e^{-i\vec{p}\cdot\vec{w}} e^{+p_0 w_0} \left[\frac{\widetilde{g}_{\mu\mu'}}{(p+\frac{P}{2})^2 - i\epsilon}\right]\left[\frac{\widetilde{g}_{\nu\nu'}}{(p-\frac{P}{2})^2 - i\epsilon}\right] \overline{u}(k_-)\gamma_{\mu'}\left[\frac{\gamma\cdot(p+\frac{P}{2}-k_-)+m_e}{(p+\frac{P}{2}-k_-)^2+m_e^2-i\epsilon}\right]\gamma_{\nu'}v(k_+) \tag{4.16}$$

$$H_{\mu\nu}(w) = \langle 0|T\{J_\mu(\frac{w}{2})J_\nu(-\frac{w}{2})\}|\pi^0\rangle_E. \tag{4.17}$$

Because the integral over w in Equation (4.15) converges exponentially at least as fast as $e^{-m_\pi|w|}$ where $|w| = \sqrt{\sum_\mu w_\mu^2}$, truncating the infinite-volume integral over w, as is needed if $H_{\mu\nu}(w)$ is to be computed using lattice methods, will introduce errors which are exponentially suppressed.

This change of integration contour is an application of Cauchy's theorem which does not change the quantity $\mathcal{A}_{\pi^0\to e^+e^-}$. The amplitude $\mathcal{A}_{\pi^0\to e^+e^-}$ remains a complex, Minkowski-space quantity. Therefore, both the real part and the imaginary part of the decay amplitude $\mathcal{A}_{\pi^0\to e^+e^-}$ can be computed directly on the lattice.

4.3 Calculating the hadronic factor

The hadronic factor $H_{\mu\nu}(w) = \langle 0|T\{J_\mu(\frac{w}{2})J_\nu(-\frac{w}{2})\}|\pi^0\rangle$ can be extracted from the lattice three-point function through the following relationship:

$$\langle 0|T\{J_\mu(x)J_\nu(0)\}|\pi^0\rangle = Z_V^2 \frac{2m_\pi V}{N_\pi} \lim_{t\to-\infty} e^{m_\pi|t|}\langle 0|T\{J_\mu(x)J_\nu(0)\pi^0(t)\}|0\rangle, \tag{4.18}$$

where Z_V is the renormalization factor that relates the non-conserved local lattice currents on the right hand side of the equation to the conserved global currents, V is the number of lattice sites on each time slice, $2m_\pi V$ comes from the normalization of pion state, and N_π is the normalization factor for pion ground state. In this calculation, we use wall-like pion interpolating operator with zero momentum defined as $\pi^0(t) = \sum_{\vec{z}}\ \pi^0(\vec{z},t)$.

There are two diagrams involved in computing the three-point function, a connected diagram and a disconnected diagram, as shown in Figure 4.4 and Figure 4.5. In the next sections, we discuss

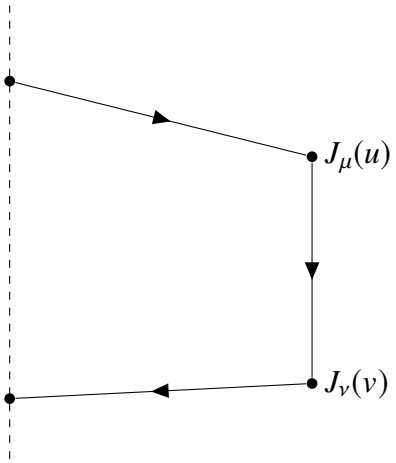

Figure 4.4: The connected diagram involved in the calculation of hadronic three point function. The dashed line on the left represents the location of the wall-like pion interpolating operator.

the strategies of calculating these two diagrams on the lattice.

4.3.1 Connected diagram

The connected diagram involved in the three-point function $\langle 0|T\left\{J_\mu(u)J_\nu(v)\pi^0(t)\right\}|0\rangle$ is shown in Figure 4.4. Let $S(x, y)$ be the propagator from y to x. Then, the contraction can be written as

$$\langle J_\mu(u)J_\nu(v)\pi^0(t_\pi)\rangle_{\text{connected}} = -\frac{2i}{3\sqrt{2}}\text{Re}[\text{tr}(\gamma_5 S(t_\pi, v)\gamma_\mu S(v, u)\gamma_\nu S(u, t_\pi))]. \tag{4.19}$$

Because we use wall-like pion interpolating operator, the contraction comprises two wall source propagators and one point source propagator. The electromagnetic currents must be separated far enough from the pion interpolating operator such that the contamination from excited states with higher energies are small enough. We always keep the time difference from the pion wall source at t to the closer current to be a fixed constant Δt. To put it more concretely, considering the periodic boundary conditions, for every lattice site t_u and t_v in $[0, T)$, we always choose a t_π such that

$$\min\left((t_u - t_\pi + T)\,\%T, (t_v - t_\pi + T)\,\%T\right) = \Delta t. \tag{4.20}$$

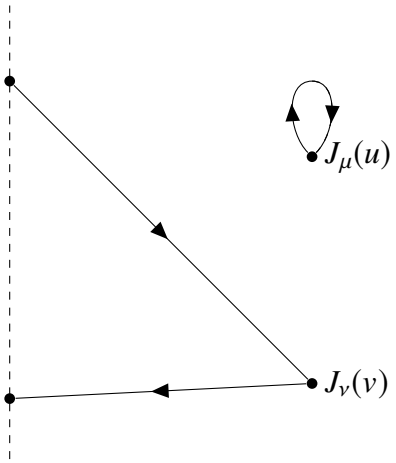

Figure 4.5: The disconnected diagram involved in the calculation of hadronic three point function. The dashed line on the left represents the location of the wall-like pion interpolating operator.

The values of Δt for each ensemble can be found in Table 4.1. In addition, we impose the constraint that the distance from t_u and t_v to pion wall can not exceed $T/2$.

To increase statistics, it is easy to observe that the case where the pion wall is on the left side of electromagnetic currents should describe the same physical process as the case where the pion wall is on the right side. Therefore, we average over these two cases to get more statistics and reduce noise.

4.3.2 Disconnected diagram

Another diagram involved in the three-point function is the disconnected diagram shown in Figure 4.5. Disconnected diagrams typically involve large noise and are more difficult to calculate. In our calculation, we use the random volume source propagators discussed in Section 3.3.2 to compute the quark self-loops formed by one electromagnetic current. The random volume source propagators are computed in the hadronic vacuum polarization calculation carried out by the RBC/UKQCD collaboration [18] [19].

Using the same notations as last section, the contraction of the disconnected diagram is

$$\langle J_\mu(u) J_\nu(v) \pi^0(t) \rangle_{\text{disconnected}} = \frac{2i}{3\sqrt{2}} \text{tr}\Big[\gamma_\mu S(u,u)\Big] \ \text{tr}\Big[\gamma_\nu S(v,t)\gamma_5 S(t,v)\Big]. \tag{4.21}$$

The amplitude from this disconnected diagram can be separated into a function of u and a function of v. We use $F_\mu(u)$ and $G_\nu(v)$ to denote these two functions

$$e^{M_\pi t_v}\langle J_\mu(u)J_\nu(v)|\pi^0\rangle_{\text{disconnected}} = F_\mu(u)G_\nu(v). \tag{4.22}$$

Since the amplitude on the left hand side is independent of v given the relative distance between two electromagnetic $r = u - v$, we can average over the position of one electromagnetic current for a given relative distance r to increase statistics. The average can be efficiently calculated using the convolution theorem and Fourier transformation:

$$\langle J_\mu(r)J_\nu(0)|\pi^0\rangle_{\text{disconnected}} = \frac{1}{N}\sum_v F_\mu(v+r)\cdot G_\nu(v) \tag{4.23}$$

$$= \frac{1}{N}\mathcal{F}^{-1}\left[\widetilde{F_\mu}(k)\cdot\widetilde{G_\nu}(-k)\right], \tag{4.24}$$

where N is the total number of lattice sites, $\mathcal{F}^{-1}$ represents inverse Fourier transform, $\widetilde{F_\mu}(k)$ is the Fourier transform of $F_\mu(u)$, and $\widetilde{G_\nu}(k)$ is the Fourier transform of $G_\nu(v)$. The convention of Fourier transforms is in Appendix B.4. Since the complexity of performing a fast Fourier transform is $O(N\log(N))$, this approach is much faster than directly averaging over v for every r whose time complexity is $O(N^2)$.

Even though the disconnected diagram is much noisier than the connected diagram, we are able to determine the amplitude of the disconnected diagram up to an error of about 60%.

4.3.3 Properties of the hadonic factor

In this section, we derive some important properties of the hadronic factor that will be used to simplify the calculation of the leptonic factor in the next section. The hadronic factor is closely related to the $\pi^0 \to \gamma\gamma$ decay

$$\int d^4x\, e^{-ipx}\langle J_\mu(x)J_\nu(0)|\pi^0(q)\rangle = \epsilon_{\mu\nu\alpha\beta}p_\alpha p'_\beta F_{\pi\gamma\gamma}(p^2), \tag{4.25}$$

where $F_{\pi\gamma\gamma}$ is the pion form factor, q is the momentum of initial pion state, and p and p' are the momentum of two photons. Let $H_{\mu\nu}(x) = \langle 0|T\{J_\mu(x)J_\nu(0)\}|\pi^0\rangle$. We have

$$H_{\mu\nu}(x) = \epsilon_{\mu\nu\alpha\beta}\int \frac{d^4p}{(2\pi)^4}e^{ipx}p_\alpha p'_\beta F_{\pi\gamma\gamma}(p^2) \tag{4.26}$$

$$= \epsilon_{\mu\nu\alpha\beta}\int \frac{d^4p}{(2\pi)^4}e^{ipx}p_\alpha (q-p)_\beta F_{\pi\gamma\gamma}(p^2) \tag{4.27}$$

$$= \epsilon_{\mu\nu\alpha\beta}\int \frac{d^4p}{(2\pi)^4}e^{ipx}p_\alpha q_\beta F_{\pi\gamma\gamma}(p^2), \tag{4.28}$$

where we used $\epsilon_{\mu\nu\alpha\beta}p_\alpha p_\beta = 0$ from the second line to the last line. If we assume that the initial poin is stationary, i.e., $q = (M_\pi, 0, 0, 0)$, then

$$H_{\mu\nu}(x) = \epsilon_{0\mu\nu\alpha}M_\pi \int \frac{d^4p}{(2\pi)^4}e^{ipx}p_\alpha F_{K_L\gamma\gamma}(p^2). \tag{4.29}$$

Based on the formula in Equation 4.29, the hadronic factor should have the following properties

- The hadronic factor is 0 at time components where $\mu = 0$ or $\nu = 0$
- The hadronic factor at each lattice site is an antisymmetric matrix, i.e., $H_{\mu\nu}(x) = -H_{\nu\mu}(x)$
- Using the property of Fourier transform, because $p_\alpha F_{K_L\gamma\gamma}(p^2)$ is an odd function of p, the hadronic factor is an odd function of x, i.e., $H_{\mu\nu}(x) = -H_{\mu\nu}(-x)$

4.4 Calculating leptonic factor

In this section, we evaluate the leptonic factor in Equation 4.16. We first calculate the factor that involves spinors and Gamma matrices

$$\widetilde{M}_{\mu\nu} = \widetilde{g}_{\mu\mu'}\widetilde{g}_{\nu\nu'}\gamma_{\mu'}\left[\gamma\cdot(p+\frac{P}{2}-k_-)+m_e\right]\gamma_{\nu'}v(k_+). \tag{4.30}$$

Because the hadronic part $H_{\mu\nu}$ is antisymmetric in μ and ν, we only need to calculate the antisymmetric part $M_{\mu\nu} = (\widetilde{M}_{\mu\nu} - \widetilde{M}_{\nu\mu})/2$, which turns out to be much simpler than the original matrix.

Using the conventions in Appendix B.2 and B.3, we can analytically calculate the matrix $M_{\mu\nu}$. If the spin of electron is positive and the spin of positron is negative, we get

$$M_{\mu\nu} = 2im_e \begin{pmatrix} 0 & p_3 & k_{-,2} - p_2 & 0 \\ -p_3 & 0 & p_1 - k_{-,1} & 0 \\ p_2 - k_{-,2} & k_{-,1} - p_1 & 0 & -\frac{M_\pi}{2} \\ 0 & 0 & \frac{M_\pi}{2} & 0 \end{pmatrix}, \tag{4.31}$$

where we assume that the last row and last column is for the time direction. On the other hand, if the spin of electron is negative and the spin of positron is positive, the matrix $M_{\mu\nu}$ is the same except that time components have opposite signs

$$M_{\mu\nu} = 2im_e \begin{pmatrix} 0 & p_3 & k_{-,2} - p_2 & 0 \\ -p_3 & 0 & p_1 - k_{-,1} & 0 \\ p_2 - k_{-,2} & k_{-,1} - p_1 & 0 & \frac{M_\pi}{2} \\ 0 & 0 & -\frac{M_\pi}{2} & 0 \end{pmatrix}. \tag{4.32}$$

In Section 4.3.3, we showed that the time components of the hadronic factor $H_{\mu\nu}$ are 0. So we can ignore the time components in $M_{\mu\nu}$ where $\mu = 0$ or $\nu = 0$. In addition, the amplitude in Equation 4.16 would be odd in $\vec{k}_-$ when $M_{\mu\nu}$ contains $k_{-,i}$. Therefore, these parts do not contribution to the final amplitude and we can ignore the k_- in $M_{\mu\nu}$. Finally, the spinor part $M_{\mu\nu}$ can be effective written as $M_{\mu\nu} = 2im_e\epsilon_{0\mu\nu\rho}p_\rho$, and the leptonic factor can be written as

$$\begin{aligned} L_{\mu\nu}(w) &= 2im_e\epsilon_{0\mu\nu\rho} \int d^3\vec{p} \int_C dp_0 e^{-i\vec{p}\cdot\vec{w}} e^{+p_0 w_0} \left[\frac{1}{(p + \frac{P}{2})^2 + m_\gamma^2 - i\epsilon}\right] \left[\frac{1}{(p - \frac{P}{2})^2 + m_\gamma^2 - i\epsilon}\right] \\ &\quad \left[\frac{1}{(p + \frac{P}{2} - k_-)^2 + m_e^2 - i\epsilon}\right] p_\rho. \end{aligned} \tag{4.33}$$

The next step in the evaluation of $L_{\mu\nu}(w)$ is to perform the p_0 integral using Cauchy's theorem. Because of the factor of $e^{p_0 w_0}$ appearing in Eq. (4.17) we must close the p_0 contour in the left-

half plane when w_0 is positive and obtain three terms coming from the poles at $\pm m_\pi/2 - |\vec{p}|$ and $-\sqrt{(\vec{p}-\vec{k}_+)^2+m_e^2}$. If w_0 is negative then we must close the contour in the right-half plane and pick the residues of the poles at $\pm m_\pi/2 + |\vec{p}|$ and $\sqrt{(\vec{p}-\vec{k}_+)^2+m_e^2}$. The result can be written as

$$\begin{aligned} L_{\mu\nu}(w) =& \frac{1}{\pi}\alpha^2 2m_e\epsilon_{0\mu\nu\rho}\int d^3\vec{p}\,\left[\frac{e^{-|\vec{p}||w_0|}e^{\frac{1}{2}M_\pi|w_0|}}{M_\pi|\vec{p}|(M_\pi-2|\vec{p}|)(-M_\pi|\vec{p}|+2\vec{p}\cdot\vec{k}_-)}\right. \\ &+\frac{e^{-|\vec{p}||w_0|}e^{-\frac{1}{2}M_\pi|w_0|}}{M_\pi|\vec{p}|(M_\pi+2|\vec{p}|)(M_\pi|\vec{p}|+2\vec{p}\cdot\vec{k}_-)} \\ &\left.+\frac{e^{-E_{pe}|w_0|}}{E_{pe}(M_\pi|\vec{p}|+2\vec{p}\cdot\vec{k}_-)(-M_\pi|\vec{p}|+2\vec{p}\cdot\vec{k}_-)}\right]p_\rho e^{-i\vec{p}\cdot\vec{w}}, \end{aligned} \tag{4.34}$$

where $E_{pe} = \sqrt{\left(\vec{k}_- - \vec{p}\right)^2 + m_e^2}$ is the energy of the virtual electron.

To obtain the final amplitude, we need to sum over all possible directions of the momentum of the outgoing electron and positron. Thus, to simplify the expression of the leptonic factor, we can average of the direction of $\vec{k}_-$ in three-dimensional space

$$\frac{1}{4\pi}\int d\Omega(\vec{k}_-)\, L_{\mu\nu}(w), \tag{4.35}$$

where $\Omega(\vec{k}_-)$ is the solid angle of $\vec{k}_-$. Let θ' be the angle between $\vec{p}$ and $\vec{k}_-$. Then, using the integrals in Equation C.1 and Equation C.2 in Appendix C,

$$\begin{aligned} L_{\mu\nu}(w) =& 2m_e\frac{\alpha^2}{\pi}\epsilon_{0\mu\nu\rho}\int d^3\vec{p}\,\frac{1}{|\vec{p}|^2}\left[-\frac{e^{-|\vec{p}||w_0|}e^{\frac{1}{2}M_\pi|w_0|}}{M_\pi(M_\pi-2|\vec{p}|)}\frac{1}{4|\vec{k}_-|}\ln(\frac{1+\beta}{1-\beta})\right. \\ &+\frac{e^{-|\vec{p}||w_0|}e^{-\frac{1}{2}M_\pi|w_0|}}{M_\pi(M_\pi+2|\vec{p}|)}\frac{1}{4|\vec{k}_-|}\ln(\frac{1+\beta}{1-\beta}) \\ &\left.+\frac{1}{2}\int \mathrm{d}\cos\theta'\,\frac{e^{-E_{pe}|w_0|}}{E_{pe}(M_\pi+2|\vec{k}_-|\cos\theta')(-M_\pi+2|\vec{k}_-|\cos\theta')}\right]\times p_\rho e^{-i\vec{p}\cdot\vec{w}}. \end{aligned} \tag{4.36}$$

Note that because $E_{pe} = \sqrt{\left(\vec{k}_- - \vec{p}\right)^2 + m_e^2}$ is also dependent on the angle θ' because $\vec{k}_-$ and p, the integration over $\cos\theta'$ in the third term can not be analytically calculated out.

Using Equation C.5 in Appendix C, we integrate out the direction of $\vec{p}$ in three-dimensional space and simplify the leptonic part to the following form

$$
\begin{aligned}
L_{\mu\nu}(w) = 2m_e\alpha^2\epsilon_{0\mu\nu\rho}\frac{w^\rho}{|\vec{w}|^2}\Bigg(&-\frac{e^{\frac{M_\pi}{2}|w_0|}}{M_\pi|\vec{k}_-|}\ln\left(\frac{1+\beta}{1-\beta}\right)\int_0^\infty \mathrm{d}|\vec{p}|\frac{e^{-|\vec{p}||w_0|}}{M_\pi - 2|\vec{p}|}\left[\cos(|\vec{p}||\vec{w}|) - \frac{\sin(|\vec{p}||\vec{w}|)}{|\vec{p}||\vec{w}|}\right] \\
&+ \frac{e^{-\frac{M_\pi}{2}|w_0|}}{M_\pi|\vec{k}_-|}\ln\left(\frac{1+\beta}{1-\beta}\right)\int_0^\infty \mathrm{d}|\vec{p}|\frac{e^{-|\vec{p}||w_0|}}{M_\pi + 2|\vec{p}|}\left[\cos(|\vec{p}||\vec{w}|) - \frac{\sin(|\vec{p}||\vec{w}|)}{|\vec{p}||\vec{w}|}\right] \\
&+ 2\int_0^\infty \mathrm{d}|\vec{p}|\,\mathrm{d}\cos\theta'\frac{e^{-E_{pe}|w_0|}}{E_{pe}(-M_\pi + 2|\vec{k}_-|\cos\theta')(M_\pi + 2|\vec{k}_-|\cos\theta')}\left[\cos(|\vec{p}||\vec{w}|) - \frac{\sin(|\vec{p}||\vec{w}|)}{|\vec{p}||\vec{w}|}\right]\Bigg).
\end{aligned}
\tag{4.37}
$$

The leptonic factor has a pole at $|\vec{p}| = \frac{M_\pi}{2}$, which corresponds to the case where two virtual photons are on-shell. The real part of the decay amplitude is obtained by taking the principal value of the integral. In this work, we use the CUBA library [20] to numerically calculate the integrals in Equation 4.37 for every lattice site w. On the other hand, the imaginary part is obtained by replacing the pole $\frac{1}{|\vec{p}|-M_\pi/2}$ with a delta function $i\pi\delta(|\vec{p}| - M_\pi/2)$, which gives us

$$
L^{\mathrm{im}}_{\mu\nu}(w) = 2\pi\alpha^2\frac{m_e}{M_\pi^2}\epsilon_{0\mu\nu\rho}\frac{w^\rho}{|\vec{w}|^2}\frac{1}{\beta}\ln\left(\frac{1+\beta}{1-\beta}\right)\left[\cos(\frac{M_\pi}{2}|\vec{w}|) - \frac{\sin(\frac{M_\pi}{2}|\vec{w}|)}{\frac{M_\pi}{2}|\vec{w}|}\right]. \tag{4.38}
$$

4.5 Lattice results of the $\pi^0 \to e^+e^-$ decay amplitude

The hadronic matrix element is calculated on four different ensembles, whose parameters are listed in Tab. 4.1. All ensembles use Möbius domain wall fermions, which can achieve good chiral symmetry with a much smaller size in the 5th dimension compared to Shamir domain wall fermions. All ensembles are generated with the Iwasaki gauge action. In addition, the 24ID, 32ID, and 32IDF ensembles use the Dislocation Suppressing Determinant Ratio (DSDR) action term to suppress chiral symmetry breaking effects. For every configuration, we have 1024 or 2048 point source propagators with randomly distributed sources and Coulomb gauge-fixed wall source propagators with sources on every time slice where the source for each propagators lies on a single

time slice. The number of point source propagators for each ensemble is listed in Tab. 4.1.

	24ID	32ID	32IDF	48I	64I
a^{-1} (GeV)	1.015	1.015	1.37	1.73	2.36
M_π (MeV)	140	140	143	135	135
size	$24^3 \times 64$	$32^3 \times 64$	$32^3 \times 64$	$48^3 \times 96$	$64^3 \times 128$
L_S	24	24	12	24	12
Z_V	0.72672(35)	0.7260(19)	0.77700(8)	0.71076(25)	0.74293(14)
Configuration separation	10	10	10	10	20
Number of Configurations	47	47	61	32	49
Point Sources	1024	2048	1024	1024	1024
Δt	10	10	14	16	22

Table 4.1: Table of lattice ensembles used in this work. All ensembles are generated by the RBC/UKQCD collaborations [21][22][23] . Here, Δt is the time difference from the pion wall source at t to the closer current, as explained in Section 4.3.1. For the ensemble names, "I" stands for Iwasaki action and "ID" means Iwasaki action + DSDR. To distinguish between two 32ID ensembles, a trailing "F" is added to the name of the finer ensemble.

The calculated real and imaginary parts of the decay amplitude are listed in Table 4.2. The experimental value for the imaginary part is evaluated using the optical theorem and the experimental pion lifetime; the experimental real part is obtained by subtracting the imaginary part contribution from the total experimental decay rate. In Figure 4.6 and Figure 4.7, we plot the calculated amplitude as a function of the upper limit of the sum over the Euclidean relative time w_0 for the imaginary part and real part, respective. We see a good plateau for all ensembles as the cutoff increases. In the table and the plots, only the contribution from the connected diagram is included, while the contribution from the disconnected diagram will be treated as a source of systematic error.

Source	Im $\mathcal{A}$ (eV)	Re $\mathcal{A}$ (eV)	Re $\mathcal{A}$ / Im $\mathcal{A}$
24ID	38.58(54)	23.06(40)	0.5976(24)
32ID	39.80(36)	23.88(29)	0.6000(20)
32IDF	36.17(47)	21.48(33)	0.5939(22)
48I	35.19(81)	20.70(66)	0.5881(52)
64I	33.99(54)	19.73(42)	0.5803(35)
Experiment	35.07(37)	21.51(2.02)	0.68(6)

Table 4.2: Table for comparison between the lattice results and experimental results. The error in parenthesis is statistical or experimental.

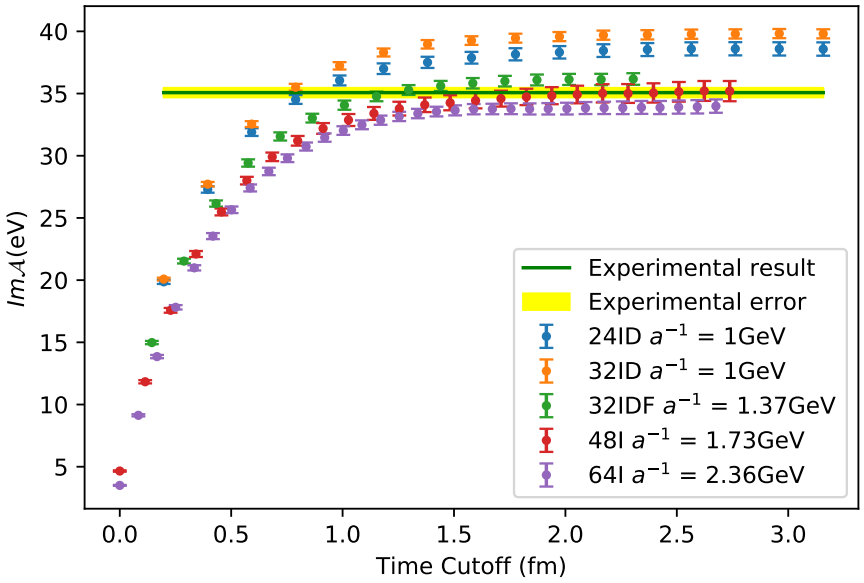

Figure 4.6: Plot of lattice results for the imaginary part of the $\pi^0 \to e^+e^-$ decay amplitude. The x-axis is the upper limit of the sum over the relative time w_0. The green line and yellow band are the experimental results with errors.

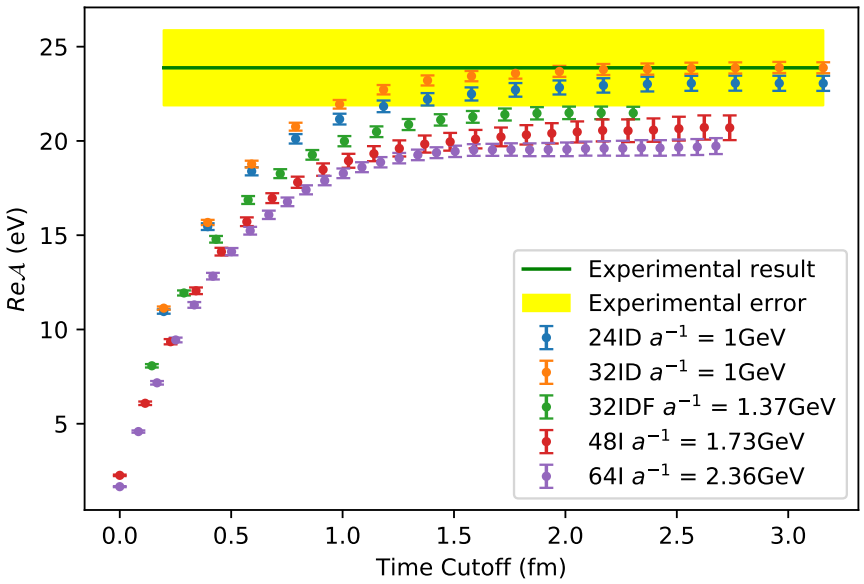

Figure 4.7: Plot of lattice results for the real part of the $\pi^0 \to e^+e^-$ decay amplitude. The x-axis is the upper limit of the sum over the relative time w_0. The green line and yellow band are the experimental results with errors.

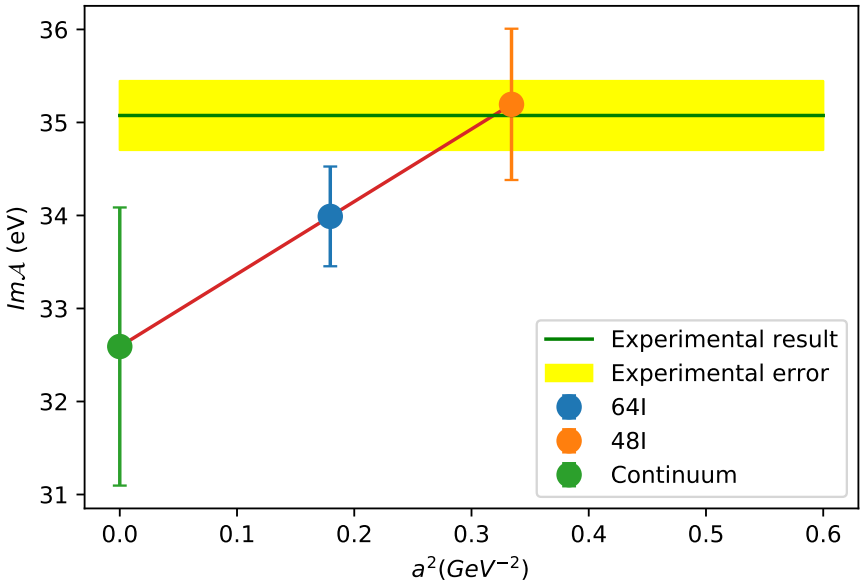

Figure 4.8: Plot of continuum limit extrapolation for the imaginary part of the amplitude. The horizontal green line and yellow band represent experimental value and error. From left to right, the three points are respectively the continuum limit, 64I, and 48I results. The errors shown in the plot are statistical.

The 48I and 64I are the two ensembles with the finest lattice spacing and therefore should have the smallest finite lattice spacing errors. Therefore, we use the continuum limit extrapolation from the 48I and 64I ensembles as our final result. Figure 4.8 and Figure 4.9 show the process of extrapolation assuming that finite lattice spacing error is proportional to a^2, where a is lattice spacing.

The estimation of a variety of systematic errors is presented in Table 4.4. The finite volume error is estimated by evaluating the difference between the 24ID and 32ID results and assuming that the finite volume error behaves as $e^{-M_\pi L}$, where L is the size of the lattice in the spatial direction. We treat this volume dependence as a physical effect and neglect the varying finite lattice spacing when determining this estimate. The error of omitting the disconnected diagram is estimated by comparing the contributions of connected and disconnected diagrams for the 24ID ensemble. We again neglect any dependence of this estimate on the lattice spacing. The disconnected diagrams are calculated using the convolution method discussed in Section 4.3.2. The contributions of the

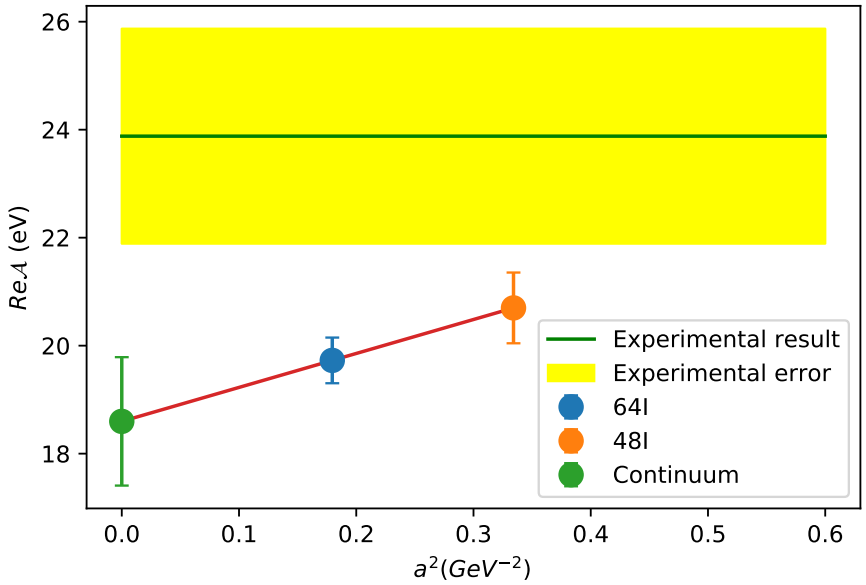

Figure 4.9: Plot of continuum limit extrapolation for the real part of the amplitude. The horizontal green line and yellow band represent experimental value and error. From left to right, the three points are respectively the continuum limit, 64I, and 48I results. The errors shown in the plot are statistical.

connected diagrams and disconnected diagrams for the 24ID ensemble are listed in Table 4.3. As shown in the table, the amplitude of the disconnected diagrams is much smaller than the amplitude of the connected diagrams, and we are able to determine the amplitude of the disconnected diagram up to an error of about 60% which makes this error estimate correspondingly uncertain. The renormalization factor for local electromagnetic current Z_V is measured in Ref. [21], where the error is also estimated. Finally, the errors in the numeral integrals including the leptonic factor are easy to control and are ignored.

Diagram	Im$\mathcal{A}$ (eV)	Re$\mathcal{A}$ (eV)
Connected	38.58(54)	23.06(40)
Disconnected	-1.11(55)	-0.62(40)

Table 4.3: The contribution to the amplitude from the connected and disconnected diagrams for the 24ID ensemble. The errors in parenthesis are statistical.

Sources	Im $\mathcal{A}$ (eV)	Re $\mathcal{A}$ (eV)	Re $\mathcal{A}$ / Im $\mathcal{A}$
Finite volume	1.33	0.89	0.0026
Disconnected diagram	0.98	0.53	0.0031
Z_V	0.013	0.074	0
Total systematic error	1.65	1.04	0.0040

Table 4.4: Sources of systematic error for the imaginary and real part of the amplitude.

Our final result is

$$\mathrm{Im}\mathcal{A} = 32.59(1.50)(1.65)\ \mathrm{eV} \tag{4.39}$$

$$\mathrm{Re}\mathcal{A} = 18.60(1.19)(1.04)\ \mathrm{eV}, \tag{4.40}$$

where the error in the first parenthesis is statistical and the error in the second parenthesis is systematic.

The real and imaginary parts of the decay amplitude are computed from the same hadronic matrix element and are significantly correlated on each lattice configuration. Therefore, the ratio $\mathrm{Re}\mathcal{A}/\mathrm{Im}\mathcal{A}$ will have smaller statistical and systematic errors and give a more precise continuum limit[1]. We could then use the very accurate experimental value for the imaginary part to obtain a more accurate prediction for the real part. In Table 4.2, we list the calculated ratio $\mathrm{Re}\mathcal{A}/\mathrm{Im}\mathcal{A}$ from each ensemble, where the statistical errors are estimated with the jackknife method. The continuum extrapolation from the 48I and 64I ensembles is shown in Figure 4.10. The systematic errors of the ratio are estimated in the same way as the real and imaginary parts and are shown in Table 4.4. Our final result for the ratio is

$$\frac{\mathrm{Re}\mathcal{A}}{\mathrm{Im}\mathcal{A}} = 0.571(10)(4), \tag{4.41}$$

where the error in the first parenthesis is statistical and the error in the second parenthesis is systematic.

[1]The author would like to thank Amarjit Soni for the suggestions about reducing errors by calculating the ratio of the real and imaginary part.

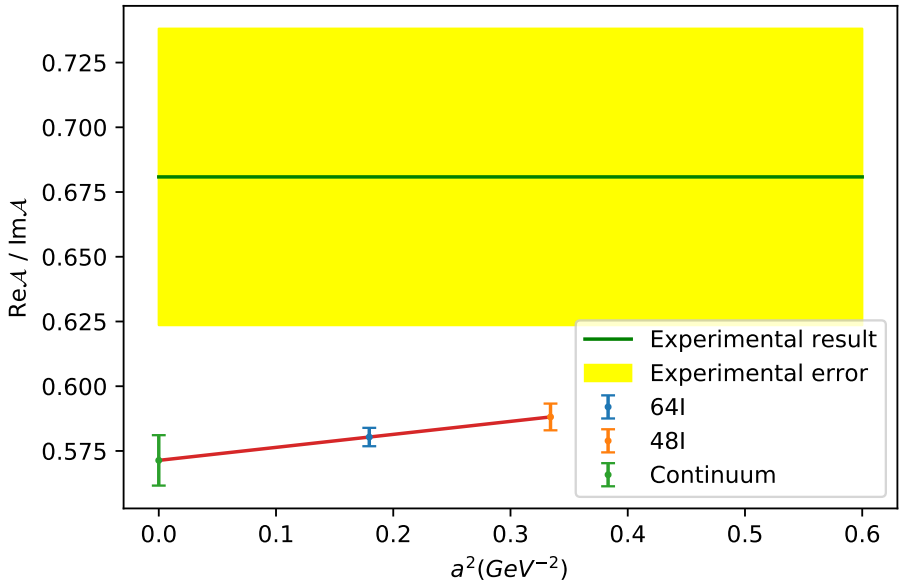

Figure 4.10: Plot of continuum limit extrapolation for the ratio of the imaginary part to real part of the decay amplitude. The horizontal green line and yellow band represent experimental value and error. From left to right, the three points are respectively the continuum limit, 64I, and 48I results. The errors shown in the plot are statistical.

Combining the optical theorem and the lattice result for the ratio of the real to imaginary parts, we obtain the branching ratio $B\left(\pi^0 \to e^+e^-\right) = 6.30(5)(2) \times 10^{-8}$, where the error in the first parenthesis is statistical and the error in the second parenthesis is systematic. This result falls within two standard deviations of the experimental branching ratio $B\left(\pi^0 \to e^+e^-\right)_{\text{exp}} = 6.87(36) \times 10^{-8}$.

Chapter 5: Calculating the $K_L \to \gamma\gamma$ decay amplitude

In this chapter, we present a general strategy for the calculation of the CP conserving part of the rare kaon decay $K_L \to \gamma\gamma$ together with further details of possible methods for computing each of the four types of connected diagram. We then apply these strategies to a physical-mass lattice QCD calculation of this decay amplitude. The two emitted photons are treated in infinite volume while the hadronic portion of the calculation is carried out in finite volume in a fashion that insures that all finite volume errors vanish exponentially in the size of this finite volume.

In Section 5.1, we review the experimental results of the $K_L \to \gamma\gamma$ decay rate as well as the properties of its decay amplitude. The only unknown quantity in the decay amplitude is a scalar factor $F_{K_L\gamma\gamma}$. In Section 5.2, we develop a strategy to decompose the scalar factor $F_{K_L\gamma\gamma}$ into an analytically known electromagnetic part $E_{\mu\nu}(r)$ and a hadronic part $H_{\mu\nu}(u, v)$ which is a matrix element that can be calculated on the lattice. Calculating the hadronic part is much more complicated than the calculation of the hadronic amplitude that enters the $\pi^0 \to e^+e^-$ decay because of the presence of the additional weak Hamiltonian operator and intermediate states whose energies are lower than kaon mass. In Section 5.3, we discuss the general strategy of calculating the hadronic matrix element, with an emphasis on demonstrating the successful removal of the contribution from these intermediate states which grows exponentially as the time increases between the creation of the kaon and the absorption of the two final-state photons. In Section 5.4, we discuss the direct subtraction of the exponentially-growing contribution from the $|\pi^0\rangle$ intermediate state and the use of the $\bar{s}d$ term to remove the $|\eta\rangle$ intermediate state. In Section 5.5, we present the strategies of calculating each type of diagram in more detail. In Section 5.6, we show the results from the lattice calculation of the $K_L \to \gamma\gamma$ decay amplitude on the 24ID ensemble from connected diagrams and compare it with the experimental values. The calculated amplitude is incomplete because the disconnected diagrams have been omitted because of their large statistical noise. In Section 5.7,

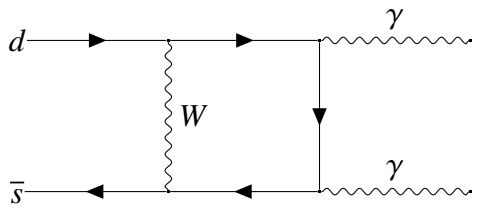

Figure 5.1: Feynman diagram for the $K_L \to \gamma\gamma$ decay.

we show the amplitude for disconnected diagrams and discuss attempts to reduce the statistical noise. In Section 5.8, we discuss the removal of the η intermediate state with the total divergence term $c_s\left(\bar{s}d + \bar{d}s\right)$.

5.1 Overview of the $K_L \to \gamma\gamma$ decay

In this section, we review the basics of the flavor changing radiative transition $K_L \to \gamma\gamma$. This decay is dominated by the long-distance contribution of order $O\left(\alpha_{\rm EM} G_F\right)$ as shown by the diagram in Figure 5.1, while the other contributions are much smaller and neglected here [24][25][26]. The branching ratio for the $K_L \to \gamma\gamma$ decay is well measured in experiment [11]:

$$B(K_L \to \gamma\gamma) = \frac{\Gamma(K_L \to \gamma\gamma)}{\Gamma_{K_L}} = (5.47 \pm 0.04) \times 10^{-4} \tag{5.1}$$

$$\Gamma(K \to \gamma\gamma) = 7.03(6) \times 10^{-12}\ \text{eV}. \tag{5.2}$$

We will neglect CP violation so the final two-photon state will be parity odd and the most general form of the decay amplitude compatible with gauge invariance and the CP odd property of K_L is

$$\langle\gamma(p)\gamma(q)|H_w|K_L(q)\rangle = (2\pi)^4\delta^{(4)}(p + p' - q)i\mathcal{M}, \tag{5.3}$$

where the amplitude $\mathcal{M}$ is can be written as

$$i\mathcal{M} = \epsilon_{\mu\nu\alpha\beta}\epsilon^*_\mu(p)\epsilon^*_\nu(p')p_\alpha p'_\beta\left[e^2\frac{G_F}{\sqrt{2}}V_{us}V_{ud}F_{K_L\gamma\gamma}\right]. \tag{5.4}$$

Here $p = \left(i\frac{M_K}{2}, \vec{p}\right)$ and $p' = \left(i\frac{M_K}{2}, -\vec{p}\right)$ are the momenta of the two on-shell photons in the final state, $q = (iM_K, \vec{0})$ is the momentum of the initial stationary kaon state, G_F is the Fermi constant, V_{us} and V_{ud} are the CKM matrix element, and $F_{K_L\gamma\gamma}$ is a scalar factor and is the only unknown quantity in the expression for decay amplitude. The tensor structure factor $\epsilon_{\mu\nu\alpha\beta}$ reflects the fact that the two photons have perpendicular polarization because K_L is CP odd. The decay rate can be written as a function of the scalar factor $F_{K_L\gamma\gamma}$

$$\Gamma(K_L \to \gamma\gamma) = \frac{M_K^3}{64\pi}\left[e^2\frac{G_F}{\sqrt{2}}V_{us}V_{ud}F_{K_L\gamma\gamma}\right]^2 \tag{5.5}$$

$$= \frac{\pi}{4}M_K^3\left[\alpha\frac{G_F}{\sqrt{2}}V_{us}V_{ud}F_{K_L\gamma\gamma}\right]^2, \tag{5.6}$$

where $\alpha = \frac{1}{137}$ is the fine-structure constant of electromagnetic interaction. Then, it is easy to work out the experimental value of the scalar factor $F_{K_L\gamma\gamma}$

$$F_{K_L\gamma\gamma} = 0.02047(9)\ \text{GeV}. \tag{5.7}$$

In the next sections, we develop the lattice method to calculate $F_{K_L\gamma\gamma}$ whose result can be compared with the experimental value.

5.2 Position space calculation of the $K_L \to \gamma\gamma$ decay amplitude

In this section, we develop a method to calculate the $K_L \to \gamma\gamma$ decay amplitude in position space, where we separate the scalar factor $F_{K_L\gamma\gamma}$ into an electromagnetic part and a hadronic part. We will directly use the Euclidean-space formulation that underlies lattice QCD calculations, following a different approach than was used in Chapter 4. In that chapter we began with a conventional Minkowski-space formulation of the $\pi^0 \to e^+e^-$ decay amplitude and then used Cauchy's theorem to express the hadronic portion of the amplitude as a Euclidean-space quantity. In the present section we begin with an $O(4)$-symmetric Euclidean evaluation of the $K_L \to \gamma\gamma$ transition amplitude. The real exponential time dependence of the Euclidean-space Green's func-

tions that we evaluate then lead to the imaginary energies which appear in Equation 5.4. As has been discussed, this Euclidean-space evaluation is complicated by the presence of easily-identified unphysical terms with exponential growth in the time separation between the kaon source and the two-photon sink. These exponentially growing terms must be explicitly subtracted caused to vanish by some other mechanism.

We denote the relative distance between two electromagnetic currents as $r = u - v$ and define the hadronic part of the amplitude as

$$H_{\mu\nu}(r) = \left\langle J_\mu(r) J_\nu(0) H'_w | K_L \right\rangle, \tag{5.8}$$

where $H'_w = C_1 Q_1 + C_2 Q_2$ is weak Hamiltonian without the constant coefficients.

Then, we have

$$\int d^4 r e^{-ipr} H_{\mu\nu}(r) = \epsilon_{\mu\nu\alpha\beta} p_\alpha p'_\beta F_{K_L\gamma\gamma} \tag{5.9}$$

$$= \epsilon_{\mu\nu\alpha\beta} p_\alpha q_\beta F_{K_L\gamma\gamma}, \tag{5.10}$$

where $p = \left(i\frac{M_K}{2}, \vec{p}\right)$ and $p' = \left(i\frac{M_K}{2}, -\vec{p}\right)$ are the momenta of the two on-shell photons in the final states, $q = (iM_K, \vec{0})$ is the momentum of initial kaon state, and we use momentum conservation $q = p' + p$ from the first line to the second line. We multiply both sides by $\epsilon_{\mu\nu\rho\sigma} p_\rho q_\sigma$ and sum over μ and ν,

$$\epsilon_{\mu\nu\alpha\beta}\epsilon_{\mu\nu\rho\sigma} p_\alpha q_\beta p_\rho q_\sigma F_{K_L\gamma\gamma} = \epsilon_{\mu\nu\rho\sigma} p_\rho q_\sigma \int d^4 r e^{-ipr} H_{\mu\nu}(r). \tag{5.11}$$

Using the property of the Euclidean-space Levi-Civita symbol and the two photons and kaon being on-shell ($p^2 = 0$ and $q^2 = -M_K^2$), it is easy to show that

$$\epsilon_{\mu\nu\alpha\beta}\epsilon_{\mu\nu\rho\sigma} p_\alpha q_\beta p_\rho q_\sigma = 2(p \cdot q)^2 = \frac{M_K^4}{2}. \tag{5.12}$$

Thus, we have

$$F_{K_L\gamma\gamma} = \frac{2}{M_K^4}\epsilon_{\mu\nu\alpha\beta}p_\alpha q_\beta \int d^4r e^{-ipr} H_{\mu\nu}(r) \tag{5.13}$$

$$= \frac{2}{M_K^4}\epsilon_{\mu\nu\alpha\beta}q_\beta \int d^4r e^{-ipr}\left(-i\frac{\partial}{\partial r^\alpha}\right) H_{\mu\nu}(r). \tag{5.14}$$

Because the initial kaon is stationary and $q = (iM_K, \vec{0})$,

$$F_{K_L\gamma\gamma} = \frac{2}{M_K^3}\epsilon_{\mu\nu\alpha 0} \int d^4r e^{-ipr}\frac{\partial}{\partial r^\alpha} H_{\mu\nu}(r) \tag{5.15}$$

$$= \frac{2}{M_K^3}\epsilon_{\mu\nu\alpha 0} \int dt e^{M_K t/2} \int d^3\vec{r} e^{-i\vec{p}\cdot\vec{r}}\frac{\partial}{\partial r^\alpha} H_{\mu\nu}(r). \tag{5.16}$$

Averaging over the spatial direction of final-state photon $\vec{p}$, we obtain

$$F_{K_L\gamma\gamma} = \frac{4}{M_K^3}\epsilon_{\mu\nu\alpha 0} \int dt e^{M_K t/2} \int d^3\vec{r}\frac{\sin(M_K|\vec{r}|/2)}{|\vec{r}|}\frac{\partial}{\partial r^\alpha} H_{\mu\nu}(r) \tag{5.17}$$

$$= \frac{2}{M_K^4}\epsilon_{\mu\nu\alpha 0} \int dt e^{M_K t/2} \int d^3\vec{r} r^\alpha \frac{-M_K|\vec{r}|\cos(M_K|\vec{r}|/2) + 2\sin(M_K|\vec{r}|/2)}{|\vec{r}|^3} H_{\mu\nu}(r) \tag{5.18}$$

$$= \int d^4r \left(\frac{2}{M_K^4} e^{M_K t/2}\epsilon_{\mu\nu\alpha 0} r^\alpha \frac{-M_K|\vec{r}|\cos(M_K|\vec{r}|/2) + 2\sin(M_K|\vec{r}|/2)}{|\vec{r}|^3}\right) H_{\mu\nu}(r). \tag{5.19}$$

We refer to the expression in the parenthesis as the electromagnetic factor and denote it as $E_{\mu\nu}(r)$. Then, the scalar factor $F_{K_L\gamma\gamma}$ can be written as the product of the electromagnetic factor and the hadronic factor

$$F_{K_L\gamma\gamma} = \int d^4r E_{\mu\nu}(r) H_{\mu\nu}(r) \tag{5.20}$$

$$E_{\mu\nu}(r) = \frac{2}{M_K^4} e^{M_K t/2}\epsilon_{\mu\nu\alpha 0} r^\alpha \frac{-M_K|\vec{r}|\cos(M_K|\vec{r}|/2) + 2\sin(M_K|\vec{r}|/2)}{|\vec{r}|^3} \tag{5.21}$$

$$H_{\mu\nu}(r) = \left\langle J_\mu(r) J_\nu(0) H_w | K_L \right\rangle. \tag{5.22}$$

We can also fix the position of the weak Hamiltonian and sum over the position of two EM

currents. Using the time translation property of Euclidean operators, we get

$$F_{K_L\gamma\gamma} = \int d^4u \int d^4v \; e^{M_K v_0} E_{\mu\nu}(u-v)\Big\langle J_\mu(u) J_\nu(v) \mathcal{H}_w(0) | K_L \Big\rangle, \tag{5.23}$$

where $\mathcal{H}_w(x)$ is the weak Hamiltonian density and $H_w = \int d^4x \; \mathcal{H}_w(x)$.

5.3 Computational strategy

Based on Equation 5.23 from last section, the $K_L \rightarrow \gamma\gamma$ decay amplitude can be computed from the following integrated product of the known amplitude $E_{\mu\nu}(u-v)$ and the infinite-volume Euclidean-space four-point function:

$$F_{K_L\gamma\gamma} = \frac{2M_K V}{N_K} \sum_{u,v} e^{M_K(v_0 - t_K)} E_{\mu\nu}(u-v)\Big\langle J_\mu(u) J_\nu(v) \mathcal{H}_w(\vec{x}, x_0) K_L(t_K) \Big\rangle, \tag{5.24}$$

where $E_{\mu\nu}(u-v)$ is the infinite-volume electromagnetic factor representing the coupling to the two final-state photons, $J_\mu(u)$ and $J_\nu(v)$ two electromagnetic currents, $H_w(x)$ the weak Hamiltonian density, $K_L(t_K)$ a wall-source interpolating operator which creates a long-lived K meson, and N_K is the normalization factor for the K_L operator. The desired decay amplitude can be obtained from the Green's function in this equation provided time difference $x_0 - t_K$ is sufficiently large that only a kaon intermediate state between the operators $H(\vec{x}, x_0)$ and $K_L(t_K)$ contributes and the component of the amplitude coming from a pion intermediate state appearing between the current-current product $J_\mu(u)J_\nu(v)$ and $H(\vec{x}, x_0)$ has been removed. After the exponentially growing contribution of this π^0 state has been removed, the sums over u and v in Equation 5.24 are exponentially convergent and the infinite-volume hadronic Green's function can be replaced by a finite volume expression, introducing errors which vanish exponentially in the linear size of this finite volume. Increased precision might be achieved by summing over the position $\vec{x}$ and averaging data for different values of x_0 and t_K, provided the difference $x_0 - t_K$ is kept sufficiently large.

While in principle keeping $x_0 - t_K$ sufficiently large and subtracting a single-pion intermediate contribution is all that is required to obtain a physical result, in an exploratory lattice calculation

such as this it is critical to examine the dependence on various time separations to demonstrate that sufficiently large values of $x_0 - t_K$ have been chosen, that the contribution from the single-pion intermediate state has been successfully removed and that any limitations in the range of the sums over u and v have not omitted non-zero data.

There are many techniques available to reduce the large number of operations suggested by the sums over u and v required by Equation 5.24 as well as those in possible selective averages over $\vec{x}$ and x_0 and t_K introduced to reduce the statistical noise. These include the introduction of sequential sources and convolution methods as well omitting regions from which the contribution is negligible or theoretically redundant terms that do not lead to a reduction the statistical errors. In Section 5.5, we discuss the details of the strategies for calculating each type of diagram.

It is clearly desirable that the methods used to evaluate each type of graph be chosen to provide the same high-level information so that the result of the calculation is not only the physical decay amplitude which can be obtained from Equation 5.24 but also the complete physical amplitude as a function of various time separations that can be used to identify the plateaus necessary to justify the choices made when evaluating the physical amplitudes. This motivates choosing evaluation strategies for the various types of graphs that will yield results for the same treatments (either summed over or fixed) of the times entering the four operators in Equation 5.24.

To that end, we begin by deciding the temporal regions in which we wish to evaluate Equation 5.24. These choices will then constrain the detailed methods used to evaluate each type of diagram.

1. Since we need to study the effects of the exponentially growing contribution for a single pion intermediate state that appears between $H_w(\vec{x}, x_0)$ and the current-current product $J_\mu(u)J_\nu(v)$, we will break the symmetry between the positions u and v and assume that $u_0 \geq v_0$. This will ensure that when $v_0 > x_0$ we can identify a contribution to Equation 5.24 in which a single pion state can be inserted between these two sets of operators and consistently identify and remove the expected exponentially growing behavior $e^{(M_K - M_\pi)(v_0 - x_0)}$.

   To implement the constraint $u_0 \geq v_0$ or equivalently $r_0 \geq 0$ on the lattice, we transform

$E_{\mu\nu}(r)$ in the following way

$$E_{\mu\nu}(r) \rightarrow \begin{cases} E_{\mu\nu}(r), & \text{where } r_0 = 0 \\ 2E_{\mu\nu}(r), & \text{where } r_0 > 0 \\ 0, & r_0 < 0 \end{cases} \tag{5.25}$$

2. When u_0 and v_0 are far separated, phenomenology (*e.g.* vector meson dominance) suggests a suppression factor of $e^{-|u_0-v_0|m_\rho}$. Therefore will treat the range of the variable $u_0 - v_0$ as safe to simply make large without further study and will ensure that for each diagram the region $10 \geq (u_0 - v_0)\%T \geq 0$ is included. Here we are accommodating the details needed for our periodic lattice with T lattice units in the time direction and the usual convention that the time coordinate is a positive number between 0 and $T - 1$.

3. In order to demonstrate that we are computing the decay rate of a kaon without contamination from a kaon excited state, we need to show a plateau as the separation $x_0 - t_K$ is increased. Thus, we propose to calculate the amplitude in Equation 5.24 for the following values of $x_0 - t_K$: $\{6, 8, 10, 12, 14\}$. These choices should both allow us to demonstrate the necessary plateau as $x_0 - t_K$ is increased and to provide a sufficient number of points in the plateau region to allow an error-weighted average to reduce that statistical errors on the final result.

4. Finally if we are to show control over the challenging exponentially growing contribution of a single pion intermediate state appearing between the current-current product and H_w we need to examine how the result depends on the time separation $v_0 - x_0$ both before and after the subtraction of the single-pion contribution. Of course, our final result requires a sum over all positive and negative values of $v_0 - x_0$ after that subtraction has been performed. Thus, we plan to compute the resulting amplitude in Equation 5.24 for all possible value of $(v_0 - x_0)\%T$.

In Section 5.5, we will describe how this is to be accomplished for each type of diagram. Finally, we should be able to obtain the amplitude $\mathcal{A}(t_K, x_0 = 0, v_0)$ and study the amplitude as a function of $x_0 - t_K$ and $v_0 - x_0$.

5.4 Removing unphysical contribution from intermediate states

The matrix element $\left\langle J_\mu(u)J_\nu(v)\mathcal{H}_w(x)K(t_K)\right\rangle$ has two intermediate states whose energies can be lower than or close to that of the initial kaon mass, the single pion state $|\pi^0\rangle$ and the single eta state $|\eta\rangle$, as shown in Figure 5.2(a). These states have unphysical contributions that increase exponentially (or decrease too slowly) as we regulate the time direction integral by an increasing finite cutoff T in Euclidean space. In this section, we show how the removal of these two intermediate states can be achieved on the lattice.

Of the possible intermediate states with energy less than M_K that should be considered, the vacuum and two-pion state do not appear because we are studying the decay of a K_L and neglecting the small CP violating contribution. Likewise the $\pi\pi\gamma$ intermediate state shown in Figure 5.2(b) must have an energy above M_K because the two pions are not at rest but carry the momentum of the photon with a magnitude $M_K/2$ which implies $E_{\pi\pi\gamma} \geq 2\sqrt{(M_K/4)^2 + M_\pi^2} + M_K/2 = 616\text{MeV} > M_K$. While this inequality implies that for large T the unphysical term coming from the $\pi\pi\gamma$ intermediate state will vanish, the size of its actual contribution should be investigated carefully. For our present study this term will be ignored.

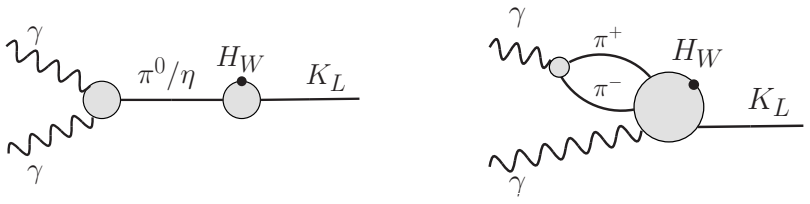

(a) (b)

Figure 5.2: Schematic representations of three possible intermediate states which may have lower energy than that of the kaon and contribute unphysical terms which grow exponentially in the difference between the time when the two final-state photons are absorbed and the time at which the weak operator $\mathcal{H}_W$ is inserted.

5.4.1 Single pion intermediate state

The π^0 intermediate state dominates the Euclidean correlation function being studied but its unphysical contribution can be accurately computed because it only involves connected diagrams. In this work, we directly calculate the unphysical contribution of the π^0 intermediate state and subtract it from the total amplitude. The contribution of the pion intermediate state is

$$\frac{1}{2m_\pi}\int_{\substack{u_0\geq v_0\\ v_0\geq 0}} du dv\ e^{m_K v_0} E_{\mu\nu}(u-v)\langle J_\mu(u)J_\nu(v)|\pi^0\rangle\langle\pi^0|H(0)|K_L\rangle \tag{5.26}$$

$$=\frac{1}{2m_\pi}\int_0^\infty dv_0\ e^{(m_K-m_\pi)v_0}\int_{r_0\geq 0} dr\ E_{\mu\nu}(r)\langle J_\mu(r)J_\nu(0)|\pi^0\rangle\langle\pi^0|H(0)|K_L\rangle, \tag{5.27}$$

where the factor $\frac{1}{2m_\pi}$ comes from the normalization of the $|\pi^0\rangle$ state. There is an explicit exponential factor $e^{(m_K-m_\pi)v_0}$ in the above formula, which is consistent with the our expectation that the contribution of $|\pi^0\rangle$ grows exponentially with the behavior $e^{(m_K-m_\pi)v_0}$ as the two electromagnetic currents are separated farther from the weak Hamiltonian. Regulating the time integral by introducing a finite upper limit T on the v_0 integral, the pion contribution can be written as

$$\frac{1}{2m_\pi}\left[\frac{e^{(m_K-m_\pi)T}-1}{m_K-m_\pi}\right]\int_{r_0\geq 0} dr\ E_{\mu\nu}(r)\langle J_\mu(r)J_\nu(0)|\pi^0\rangle\langle\pi^0|H(0)|K_L\rangle, \tag{5.28}$$

where the "-1" term inside the square bracket is the physical contribution of the π^0 intermediate state to the $K_L\to\gamma\gamma$ decay amplitude while the term that grows exponentially with increasing T is not of physical interest and must be removed from the Euclidean expression. After subtracting this unphysical contribution of the $|\pi^0\rangle$ intermediate state, the decay amplitude should be well-defined on finite volume lattice with exponentially suppressed errors.

In a lattice calculation the subtraction of the unphysical pion intermediate state contribution must be performed more carefully to avoid introducing $O(a)$ errors. We introduce the notation

$$A_\pi = \frac{1}{2m_\pi}\sum_{r,r_0\geq 0} E_{\mu\nu}(r)\langle J_\mu(r)J_\nu(0)|\pi^0\rangle\langle\pi^0|H(0)|K_L\rangle. \tag{5.29}$$

We first subtract the entire pion contribution on each time slice

$$\mathcal{F}^{\text{sub}}_{K_L\gamma\gamma}(v_0) = \mathcal{F}_{K_L\gamma\gamma}(v_0) - A_\pi f(v_0), \tag{5.30}$$

where $\mathcal{F}_{K_L\gamma\gamma}(v_0)$ is the original amplitude without subtracting pion state, and $f(v_0)$ is the exponential factor

$$f(v_0) = \begin{cases} e^{(M_K - M_\pi)v_0}, & v_0 > 0 \\ \frac{1}{2}, & v_0 = 0 \\ 0, & v_0 < 0 \end{cases} . \tag{5.31}$$

Then, we must add back the physical part of the pion intermediate state contribution

$$\mathcal{F}^{\text{final}}_{K_L\gamma\gamma} = \sum_{v_0=-\infty}^{T} \mathcal{F}^{\text{sub}}_{K_L\gamma\gamma}(v_0) - \frac{\cosh((M_K - M_\pi)/2)}{2\sinh((M_K - M_\pi)/2)} A_\pi, \tag{5.32}$$

where the second term is the physical contribution of pion state that should not be subtracted. It is easy to show that the second term converges to the physical contribution in continuum limit in Equation 5.28, i.e. $-\frac{1}{M_K - M_\pi} A_\pi$, in the limit of $a \to 0$.

Since this procedure of removing the unphysical single-pion contribution may be unfamiliar and the present case somewhat more complicated that the similar problem of removing unphysical single-pion contribution from the calculation of the $K_K - K_S$ mass difference, we will provide the logic behind the method described above. We begin with the continuum amplitude specified in Equation 5.23. As worked out above, a single pion at rest makes a contribution to the right hand side of Equation 5.23 given by Equation 5.28 where the two terms in square brackets are easy to recognize. The exponentially growing term corresponds precisely to the contribution to the Euclidean path integral from the process in which the operator $H_W(0)$ and the product of the two currents are separated by a large time and an intermediate pion travels between them. This term is not part of the process we are studying and should be removed. The second "-1" term is the

standard contribution of the pion to the decay process of interest and should be retained.

Since the contribution of the single-pion state is well understood, there is no difficulty distinguishing these two terms analytically in the continuum and this procedure can be carried out analytically on the lattice as well since the product $A_\pi e^{(M_K - M_\pi)T}$ is known. While T may be large, we need not take the limit $T \to \infty$ since T should only be sufficiently large that a similar, exponentially converging term $A_X e^{(M_K - M_X)T}$ can be neglected, where X labels the lightest intermediate state whose (vanishing) unphysical contribution has not been removed. For example, if we have removed the contribution of the η state entirely by a choice of the $\overline{s}d$ term in H_W, then $X = \eta'$ or another energetic three-pion state.

However, we must take care that we do not introduce $O(a)$ errors when we remove the continuum $A_\pi e^{(M_K - M_\pi)T}$ contribution. This can be done in two ways. The most easily derived approach is to recognize that the integral defining the expression in Equation 5.23 must be performed carefully on the lattice since an upper limit T must be introduced and the presence of the pion intermediate state implies that the contribution to the integral does not vanish near the end point $v_0 = T$. However, this is easily done if we evaluate the integral using a trapazoidal rule and include the final $v_0 = T$ term with a coefficient of 1/2. Then we are calculating the cut-off integral without $O(a)$ errors and can safely subtract the continuum term $A_\pi e^{(M_K - M_\pi)T}$, introducing finite lattice spacing errors that begin at $O(a^2)$.

In a second approach we might simply perform the sum over lattice time up to and including the upper limit T. However, since we know the time-dependence of the single-pion contribution to such a lattice sum, we would then subtract, the T-dependent part of that geometric series sum. The geometric series sum is

$$A_\pi \sum_{t=n}^{T} e^{(M_K - M_\pi)t} = A_\pi \frac{e^{(M_K - M_\pi)(T+1/2)} - e^{-(M_K - M_\pi)(1/2-n)}}{2 \sinh\left[\frac{M_k - M_\pi}{2}\right]}. \tag{5.33}$$

where n is an arbitrary lower bound of the summation, and, as elsewhere in this thesis, all quantities

are expressed in lattice units. The T-dependent part that we should subtract is

$$A_\pi \frac{e^{(M_K - M_\pi)(T+1/2)}}{2\sinh\left[\frac{M_k - M_\pi}{2}\right]} \tag{5.34}$$

Both methods give the same result to $O(a)$ and we expect the second method may be more accurate.

The presentation given in this thesis involves an extra step with an additional issue. We would like to examine the explicit sum over v_0 in our lattice calculation after we have subtracted the π^0 contribution to show that the subtracted integrand has reached zero by the time we have reached the upper limit T. This may give a more precise estimate for the size of the terms discarded by our finite time integration than would be learned from looking for a plateau in the integrated result as the upper limit T is varied. In order to do this we subtract the "contribution of the single-pion state" for each value of v_0, $0 \leq v_0 \leq T$. Here we must be careful that this new procedure does not change the subtraction that has been justified above.

This "single-integration" procedure is used to reveal the systematic errors introduced by the finite integration range T and does not provide further insight into the $O(a)$ errors. The concept of subtracting the single-pion contribution when $v_0 = 1$ or 2 lattice units has no continuum limit and $O(a)$ errors cannot be recognized this level of detail. Instead we are free to introduce a reasonable *ansatz* for the v_0-dependent single-pion subtraction that has the correct continuum behavior for large v_0 where it is actually being used. Our procedure for doing this is defined in Equation 5.31. We then evaluated the sum of the terms we have subtracted and introduced a correction so that the final subtraction is only that determined by the lattice treatment of the upper limit, *i.e.* the subtraction shown in Equation 5.34 above, appropriate for the choice in Equation 5.31. This is the origin of the right-hand term appearing in the right-had side of Equation 5.32.

The two matrix elements in Equation 5.27 can be extracted from the following three-point

correlation functions on the lattice

$$\langle \pi^0 | H_w(0) | K^0 \rangle = \lim_{\substack{t_K \to -\infty \\ t_\pi \to \infty}} \frac{2M_K V}{N_K} \frac{2M_\pi V}{N_\pi} \frac{1}{V} \sum_{\vec{x}} e^{M_K(t_w - t_K)} e^{M_\pi(t_\pi - t_w)} \langle 0 | \pi^0(t_\pi) H_w(\vec{x}, t_w) K^0(t_K) | 0 \rangle \tag{5.35}$$

$$\langle 0 | J_\mu(r) J_\nu(0) | \pi^0 \rangle = \lim_{t_\pi \to -\infty} Z_V^2 \frac{2M_\pi V}{N_\pi} e^{M_\pi |t_\pi|} \langle 0 | J_\mu(r) J_\nu(0) \pi(t_\pi) | 0 \rangle, \tag{5.36}$$

where $N_\pi = \langle \pi^0 | \pi^0(t_\pi = 0) | 0 \rangle$ and $N_K = \langle K^0 | K^0(t_K = 0) | 0 \rangle$ are the normalization constants of pion and kaon interpolating operators, and V is the number of lattice sites on each time slice. The average over spatial component $\vec{x}$ in the first equation is not necessary but can increase statistics and reduce noise. The contraction diagrams involved in computing the two three-point functions are in Figure D.6, Figure D.7, and Figure D.8 in Appendix D. We do not include the disconnected diagrams in the calculation of $\langle 0 | J_\mu(r) J_\nu(0) | \pi^0 \rangle$, because their contribution is much smaller than the connected diagram as shown in Section 4.4, and because we also ignored all diagrams where an electromagnetic current contracts with itself in later calculation of the $K_L \to \gamma\gamma$ amplitude.

5.4.2 Single eta intermediate state

The unphysical contribution of η state is more difficult to remove. While $M_\eta > M_K$ their difference is not large making the exponential fall-off of the unwanted term slow and the $M_K - M_\eta$ energy denominator, similar to the $M_K - M_\pi$ in Equation 5.28, is also small. Since disconnected diagrams play a large role in this $K_L - \eta$ amplitude, this term also has a large statistical uncertainty and we expect that it is best to add an extra $c_s(\bar{s}d + \overline{d}s)$ term to $\mathcal{H}_W$ with the coefficient c_s adjusted to make the matrix element $\langle \eta | \mathcal{H}_W | K_L \rangle = 0$. This was the most effective strategy for dealing with the η intermediate state in the calculation of ΔM_K [27].

The $\bar{s}d$ term is a total divergence term [28][29] and can be written as

$$\bar{s}d = \frac{-i}{m_s - m_d} \frac{\partial}{\partial x_\mu} \left(\bar{s} \gamma_\mu d \right). \tag{5.37}$$

Thus, adding the $\bar{s}d$ term into the Hamiltonian does not change the integral of the Hamiltonian in the entire spacetime

$$\int d^4x \, (H_w(x) + c_s \bar{s}d(x)) = \int d^4x \, H_w(x), \tag{5.38}$$

where c_s is any constant number and the subscript s represents that the operator $\bar{s}d$ is a scalar rather than a pseudo-scalar. We should observe that Equation 5.37 is valid for the combination of QCD and QED so that the presence of the two electromagnetic currents in our matrix element do not invalidate this lack of dependence on c_s.

The $|\eta\rangle$ intermediate state can be removed by properly choosing the coefficient c_s such that the transition matrix element from kaon to eta is zero

$$\langle \eta | H_w(x) + c_s \bar{s}d(x) | K^0 \rangle = 0. \tag{5.39}$$

Then, the desired value of c_s can be solved from the above equation

$$c_s = -\frac{\langle \eta | H_w(x) | K^0 \rangle}{\langle \eta | \bar{s}d(x) | K^0 \rangle}. \tag{5.40}$$

The two matrix elements in the above equation can be extracted from the three-point Green functions

$$\langle \eta | H_w(x) | K^0 \rangle = \lim_{\substack{t_K \to -\infty \\ t_\eta \to \infty}} \frac{2M_K V e^{m_K |t_K|}}{N_K} \frac{2M_\eta V e^{m_\eta |t_\eta|}}{N_\eta} \langle 0 | \eta(t_\eta) H_w(x) K^0(t_K) | 0 \rangle \tag{5.41}$$

$$\langle \eta | \bar{s}d(x) | K^0 \rangle = \lim_{\substack{t_K \to -\infty \\ t_\eta \to \infty}} \frac{2M_K V e^{m_K |t_K|}}{N_K} \frac{2M_\eta V e^{m_\eta |t_\eta|}}{N_\eta} \langle 0 | \eta(t_\eta) \bar{s}d(x) K^0(t_K) | 0 \rangle. \tag{5.42}$$

Since the values of the matrix elements are not dependent on the spatial coordinate $\vec{x}$, we can average over all $\vec{x}$ on each time slice to increase the statistics and reduce noise. The diagrams involved in calculating the two matrix elements in c_s are listed in Appendix D.4 and Appendix D.5. After determining c_s, we need to calculate an additional correlator $\langle J_\mu(u) J_\nu(v) \bar{s}d(x) K_L(t_K) \rangle$, whose dia-

grams are listed in Appendix D.6. It is worth noting that these correlators all involve disconnected diagrams which contain large noise but play an important role in the dynamics associated with the η particle.

5.5 Strategies for each type of the diagrams

The leading order diagrams for calculating the four-point correlator $\left\langle J_\mu(u)J_\nu(v)H_w(\vec{x}, x_0)K_L(t_K)\right\rangle$ are listed in Appendix D.1. We divide the diagrams into 5 types based on their topologies, where each type may contain one or multiple diagrams. In addition, because we break the symmetry between two electromagnetic currents u and v and always assume $u_0 \geq v_0$, the two diagrams with u and v swapped are different and we must calculate them separately. In this work, the diagrams with label (a) and the diagrams with label (b) are identical except that (u, μ) and (v, ν) are exchanged. Calculating these diagrams is not a trivial task, and more complicated techniques are often required besides simple combinations of propagators. In this section, we discuss the strategies of calculating each type of diagram and demonstrate how to obtain the amplitude as of function of the $x_0 - t_K$ and $v_0 - x_0$ as discussed in Section 5.3.

5.5.1 Type I and type II diagrams

The type I diagrams are shown in Figure D.1. We choose the position of the weak Hamiltonian x as the source of point source propagators and put the kaon wall at a fixed distance from the weak Hamiltonian. Suppose x is fixed at 0, these diagrams can be factored into a sum of products of a function of u multiplied by a function of v

$$H_{\mu\nu}(r) = \sum_{v,\rho} F_{\mu\rho}(u = v + r)G_{\nu\rho}(v). \tag{5.43}$$

Combining it with the electromagnetic factor, we obtain

$$\mathcal{A} = \sum_r H_{\mu\nu}(r) E_{\mu\nu}(r) \tag{5.44}$$

$$= \sum_r \left(\sum_v F_{\mu\rho}(v+r) G_{\nu\rho}(v) \right) E_{\mu\nu}(r). \tag{5.45}$$

Since we want to obtain the amplitude as a function of v_0, we can sum over r first, and then sum over the spatial directions of v, i.e.,

$$\mathcal{A}(v_0) = \sum_{\vec{v}} \left(\sum_r F_{\mu\rho}(v+r) E_{\mu\nu}(r) \right) G_{\nu\rho}(v). \tag{5.46}$$

Directly summing over r for every lattice site v has computational cost of order V^2 where V is the spatial volume and is prohibitively expensive. However, we can use the convolution theorem and fast Fourier transform to reduce the computational cost to one of order $V \ln(V)$

$$\sum_r E_{\nu\mu}(r) F_{\mu\rho}(v+r) \tag{5.47}$$

$$= \mathcal{F}^{-1}[\widetilde{E_{\nu\mu}}(-k) \cdot \widetilde{F}_{\mu\rho}(k)], \tag{5.48}$$

where $\mathcal{F}^{-1}$ represents inverse Fourier transform, $\widetilde{F}_{\mu\rho}(k)$ is the Fourier transform of $F_{\mu\rho}(u)$, and $\widetilde{E_{\nu\mu}}(k)$ is the Fourier transform of $E_{\nu\mu}(r)$.

The type II diagrams are shown in Figure D.2. These are evaluated using the same convolution strategy as was employed for type I. As is the case for type I, three point-source propagators are needed with the point source located at the position of the weak operator x, and the amplitude can factored into a sum of products of a function of u multiplied by another function of v. For the case of type II, one of those point-source propagators is evaluated at the location of the weak operator forming the closed loop.

5.5.2 Type III diagrams

The type III diagrams are shown in Figure D.3. These are difficult to calculate because of the loop formed by three point source propagators as shown in the diagram. If we choose v as the source for point source propagators, the propagator from u to x will be hard to calculate. To deal with this problem, we compute a sequential source propagator from v to u to x. The calculation of a sequential source propagator is discussed in Section 3.3 and is typically performed by choosing the source to be another propagator. In our calculation, in addition to another propagator, the source also contains the electromagnetic factor

$$(D_{\text{dwf}} S_{\text{seq}})(u) = \sum_{\mu,\nu} \gamma_\mu L(u, v) \gamma_\nu \; E_{\mu\nu}(u, v), \tag{5.49}$$

where $L(u, v)$ represents the light quark point source propagator from v to u. Solving this equation would give us the following sequential propagator

$$S_{\text{seq}}(x, v) = \sum_{u} \sum_{\mu,\nu} L(x, u) \gamma_\mu L(u, v) \gamma_\nu \; E_{\mu\nu}(u, v). \tag{5.50}$$

It is worth noting that point u has been implicitly summed over the allowed region on the lattice when solving the sequential source propagators. The allowed region of u is controlled by transforming $E_{\mu\nu}(u, v)$ in the way shown in Equation 5.25.

After computing the sequential source propagator, we sum the position of weak Hamiltonian x over each time slice x_0, and average over all point sources v over each time slice v_0. Then, we get the amplitude $\mathcal{A}'(t_K, x_0, v_0)$ as a function of t_K, x_0, and v_0. Finally, we use translational invariance to average over the center of mass time coordinate

$$\mathcal{A}(t_K, x_0 = 0, v_0) = \frac{1}{T} \sum_{x_0} \mathcal{A}'(t_K + x_0, x_0, v_0 + x_0). \tag{5.51}$$

5.5.3 Type IV diagrams

The type IV diagrams are shown in Figure D.4. The type IV diagrams contain a quark self-loop $S(x, x)$ in which the weak Hamiltonian contracts with itself. The self-loops $S(x, x)$ must be calculated on all lattice sites x but directly solving them by inverting the Dirac matrix on specific sources is prohibitively expensive. As discussed in Section 3.3.2, we use random volume source propagators to stochastically approximate the quark self-loop.

Diagram 1(a) and diagram 2(a) are easy to calculate. We choose v as the source of point source propagators. Point u is summed over the entire spacetime with constraint $u_0 \geq v_0$. We also sum the position of weak Hamiltonian x over each time slice x_0, and average over all point sources v over each time slice v_0. Then, we get the amplitude $\mathcal{A}'(t_K, x_0, v_0)$ as a function of t_K, x_0, and v_0. Finally, similar to the type III diagrams, we use translational invariance to average over the center of mass time coordinate

$$\mathcal{A}(t_K, x_0 = 0, v_0) = \frac{1}{T} \sum_{x_0} \mathcal{A}'(t_K + x_0, x_0, v_0 + x_0). \tag{5.52}$$

Diagram 1(b) and diagram 2(b) are a little more complicated. We choose u as the source of point source propagators. Then, both v and x are summed over each time slice, and the point source u is averaged over each time slice. We obtain amplitude $\mathcal{A}''(t_K, x_0, v_0, u_0)$. Finally as for the other diagrams we sum over all u_0 within the allowed region with $u_0 \geq v_0$

$$\mathcal{A}'(t_K, x_0, v_0) = \sum_{u_0} \mathcal{A}''(t_K, x_0, v_0, u_0). \tag{5.53}$$

Finally, similar to the type III diagrams, we can average over the center of mass coordinate

$$\mathcal{A}(t_K, x_0 = 0, v_0) = \frac{1}{T} \sum_{x_0} \mathcal{A}'(t_K + x_0, x_0, v_0 + x_0). \tag{5.54}$$

5.5.4 Type V diagrams

The type V diagrams are shown in Figure D.5 and are calculated in the same way as the type IV (a) diagrams. However, type V diagrams are disconnected and are subject to large noise. In the next section, we show the lattice calculation results for the $K_L \to \gamma\gamma$ decay without considering the contribution from the disconnected diagrams. In Section 5.7, we discuss our attempts to calculate the disconnected diagram and to reduce noise.

5.6 Lattice results for the $K_L \to \gamma\gamma$ decay amplitude

In this section, we show the lattice calculation results for the $K_L \to \gamma\gamma$ amplitude and compare it with experimental values. The calculation is performed on the 24ID ensemble that is introduced in Section 4.5 with parameters listed in Table 4.1. For each configuration, we have 512 point source propagators with randomly distributed sources for both the light quark and strange quark and Coulomb gauge-fixed wall source propagators with sources on every time slice. We generate 512 sequential source propagators for every configuration, one for each point source propagator. We also compute random volume source propagators with 2000 low modes and 768 high modes (64 hits with spin and color dilution). The calculation is performed on 117 gauge configurations with the separation between two configurations being 10 Molecular Dynamics time units.

We ignore all disconnected diagrams in this section because they contain uncontrollably large noise on the 24ID ensemble and we have been unable to obtain a meaningful result. Also, based on the Okubo-Zweig-Iizuka rule [30][31][32], the contributions of disconnected diagrams are suppressed and we can often obtain a reasonably accurate decay amplitude from only the connected diagrams. For the $K_L \to \gamma\gamma$ decay, the connected diagrams are the type I to type IV diagrams in Appendix D.1.

We perform an error-weighted average of multiple values of the distance between the kaon wall and weak Hamiltonian $x_0 - t_K$ to gather more statistics for the amplitude and control the distance between electromagnetic currents and the weak Hamiltonian $v_0 - x_0$. The statistical errors are

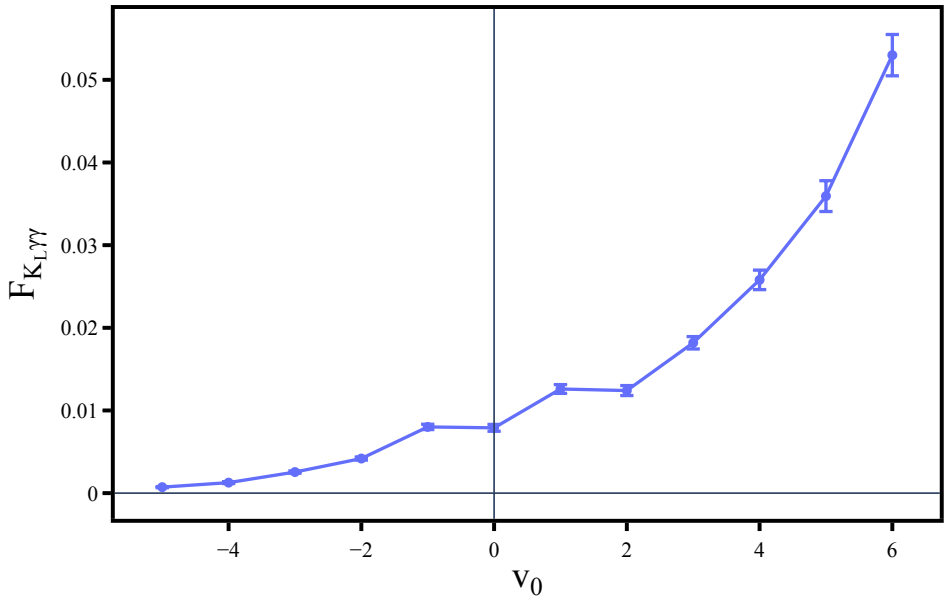

Figure 5.3: Amplitude $F_{K\gamma\gamma}$ v.s. v_0 before subtracting the pion intermediate state. The position of the weak Hamiltonian is fixed at $x_0 = 0$.

estimated with the aid of the double jackknife method, where the inner jackknife resampling is used to calculate the errors for each position of kaon wall, and different positions of kaon wall are averaged with weights proportional to the inverse of the square of estimated errors.

Although we must ultimately sum over the earliest time coordinate v_0 appearing in the product of the electromagnetic currents, it is important to begin by obtaining this correlation function for each value of $v_0 - x_0$. This will allow us to identify the exponentially increasing contribution of the π^0 intermediate state and demonstrate that this contribution has been removed when the independently computed π^0 contribution has been subtracted. We plot the amplitude as a function of v_0 with weak Hamiltonian fixed at origin in Figure 5.3, where there is evident exponential growth in the amplitude as the electromagnetic currents and weak Hamiltonian are separated farther from each other.

To demonstrate that the exponential increase in the amplitude is indeed caused by the pion intermediate state, we directly fit the amplitude for $v_0 \in [4, 14]$ with the following exponential

M	0.365(7) GeV
C	0.0060(5)
b	-0.004(18)

Table 5.1: Result of fitting the amplitude v.s. v_0 with an exponential function to demonstrate that the exponential increase caused by the pion intermediate state. The errors in parenthesis are statistical.

function

$$\mathcal{A}(v_0) = C \exp(M v_0) + b, \tag{5.55}$$

where C, M and b are three parameters to fit. We start from $v_0 = 4$ because for small values of v_0 the pion intermediate state is not dominant and the amplitude is affected by the contributions of other states with higher energies. Based on the plot of amplitude after subtracting pion contribution in Figure 5.7 that we will discuss later, the exponentially decaying physical amplitude gets very close to 0 at $v_0 \geq 2$. The parameters are fitted by minimizing the chi-squared value. The fitted curve is shown in Figure 5.4, where the exponential function agrees well with the growth pattern. The results of fitted parameters are listed in Table 5.1. It is worthwhile to note that the fitted mass parameter $M = 0.365(7)$ GeV is consistent with our expected exponential growth rate which is $M_K - M_\pi = 0.364$ GeV.

Because all disconnected diagrams are ignored, there will be both $I = 0$ and $I = 1$ neutral pseudoscalar mesons with the same mass. It is only when the disconnected diagrams are included that this $I = 0$ state combines with the $i\bar{s}\gamma^5 s$ contribution to become the η and η' mesons. Effectively, we have two independent "pion" intermediate states with the same mass, $i\bar{u}\gamma_5 u$ and $i\bar{d}\gamma_5 d$ [33]. The contributions of both states can be calculated from Equation 5.27 and their unphysical contributions are directly subtracted. The first half in the equation $\int_{r_0>0} dr\ E_{\mu\nu}(r)\langle J_\mu(r) J_\nu(0)|\pi^0\rangle$ is essentially the same as the calculation of $\pi^0 \to \gamma\gamma$ decay amplitude, except that the exponential factor in electromagnetic part $E_{\mu\nu}(r)$ involves the kaon rather than the pion mass. In Figure 5.5, we plot its amplitude against the cutoff in time direction, where r_0 is summed within the cutoff. We choose the cutoff as $r_0 = 10$ where the plateau is formed and the statistical error is small

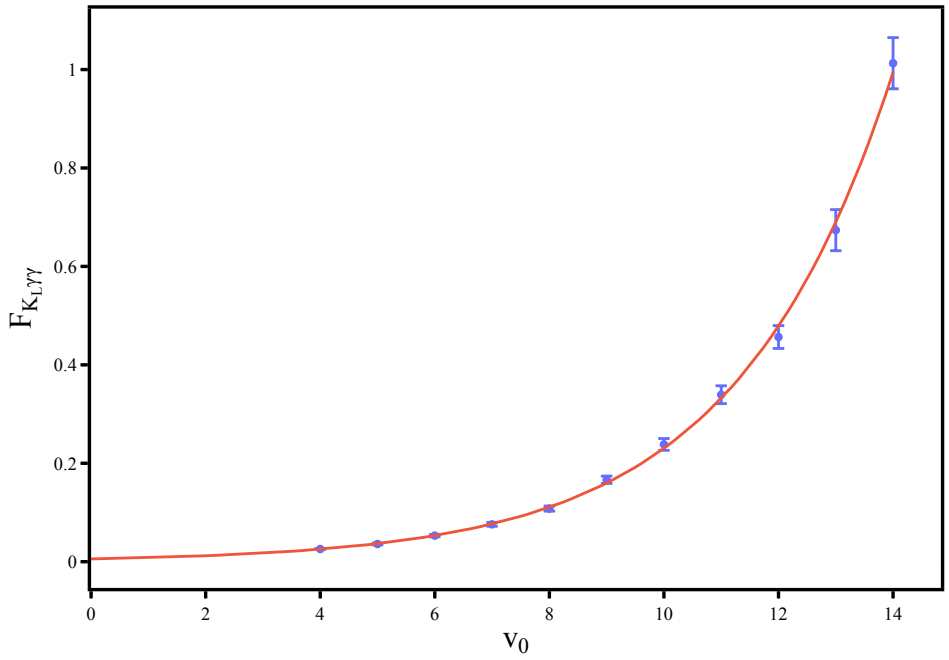

Figure 5.4: Fitting the amplitude v.s. v_0 with an exponential function. The red line is the fitted curve. The chi-square per degree of freedom is 0.41.

compared to what would be obtained had we integrated over the entire lattice. The second factor $\langle \pi^0 | H_w(0) | K_L \rangle$ is extracted from three point function $\langle \pi^0(t_\pi) H_w(x_0) K_L(t_K) \rangle$ whose diagrams are listed in Appendix D.3. In Figure 5.6, we plot matrix element $\langle i\bar{u}\gamma_5 u | H_w | K_L \rangle$ and $\langle i\bar{d}\gamma_5 d | H_w | K_L \rangle$ as a function of the separation between H_w and K_L. We also perform an error-weighted average of multiple positions of kaon wall to increase statistics. As shown in the plot, we fit the plateau for $x_0 - t_K \in [8, 15]$ and mean values and errors of the plateau are plotted as three straight lines extending over the fitting range.

After subtracting the pion intermediate state, the exponential increase in the amplitude vanishes, and the amplitude of connected diagrams converges rapidly to 0 at small values of v_0, as shown in Figure 5.7. The total decay amplitude is obtained by summing over v_0 from -8 to 4, where the upper and lower limits are selected based on Figure 5.7. In addition, the physical part of pion contribution in Equation 5.28 must be added back.

In Table 5.2, we list the amplitude for each type of diagram and for Q_1 and Q_2 separately

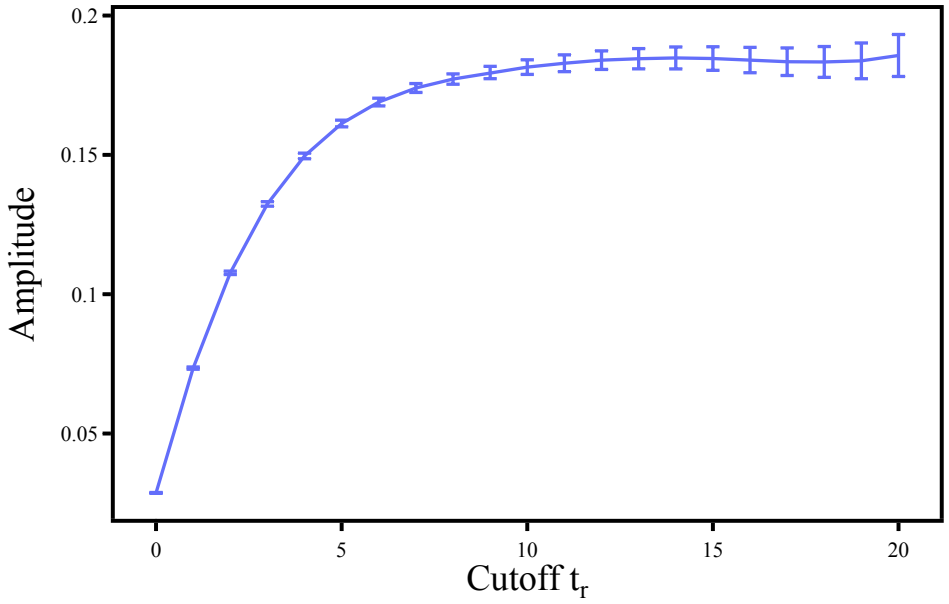

Figure 5.5: Plot of the amplitude $\sum_{\vec{r},t_r>0} E_{\mu\nu}(r)\langle J_\mu(r)J_\nu(0)|i\bar{u}\gamma_5 u\rangle$ against cutoff in t_r.

	Q_1	Q_2
Type I	0.1624(13)	-0.1077(10)
Type II	0.00006(14)	0.0010(7)
Type III	0.0146(6)	-0.0055(11)
Type IV	0.0036(5)	0.0256(14)

Table 5.2: Amplitude for each type of diagram and for Q_1 and Q_2 separately. The errors in parenthesis are statistical.

before subtracting the unphysical contribution from the pion intermediate state. The amplitudes in the table include the factor of the Wilson coefficients.

The systematic errors from different sources are listed in Table 5.3. The finite lattice spacing error is estimated by comparing the real part of the $\pi^0 \to e^+e^-$ decay amplitude calculated on the 24ID ensemble with its continuum limit extrapolation. The finite volume error is estimated by comparing the $\pi^0 \to e^+e^-$ decay amplitude calculated on the 24ID and 32ID ensembles. The error from choosing $v_0 = 4$ as the integration upper limit is computed as the difference between cutting off at $v_0 = 4$ and cutting off at $v_0 = 5$. We can get approximate estimate of the systematic errors for Wilson coefficients from those that were estimated in an earlier work [34] done at a similar but somewhat smaller lattice spacing and with two of the same operators. The error from

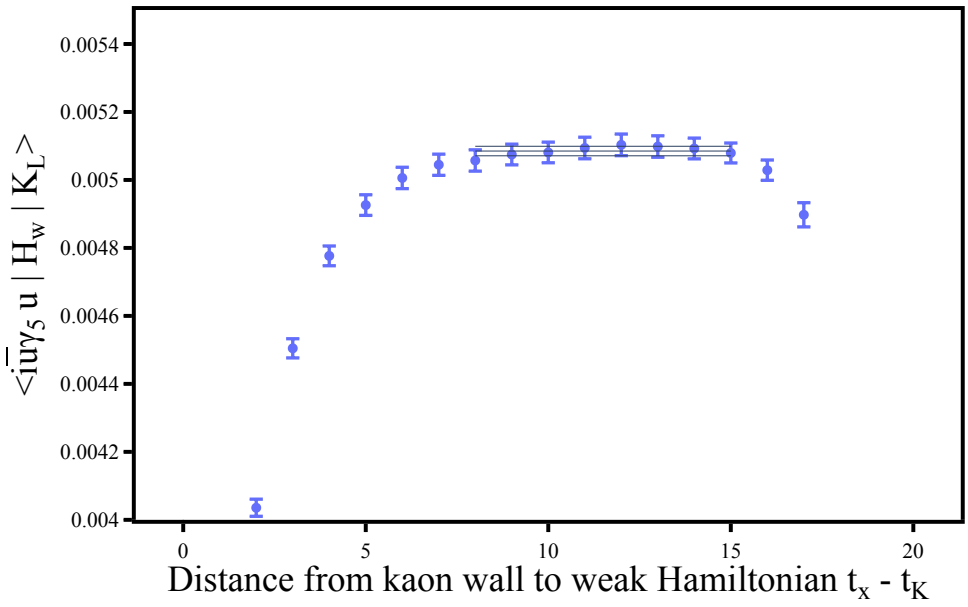

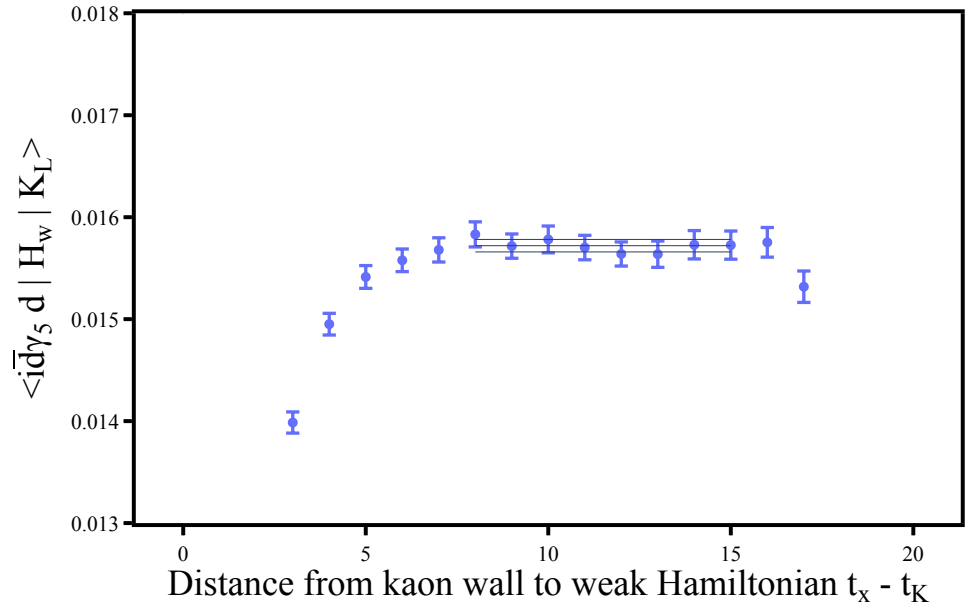

Figure 5.6: The matrix elements $\langle i\bar{u}\gamma_5 u|H_w|K_L\rangle$ and $\langle i\bar{d}\gamma_5 d|H_w|K_L\rangle$ plotted as a function of the time separation between H_w and K_L. The plateau is formed between 8 and 15 whose mean value and errors are plotted as three straight lines extending over the fitting range.

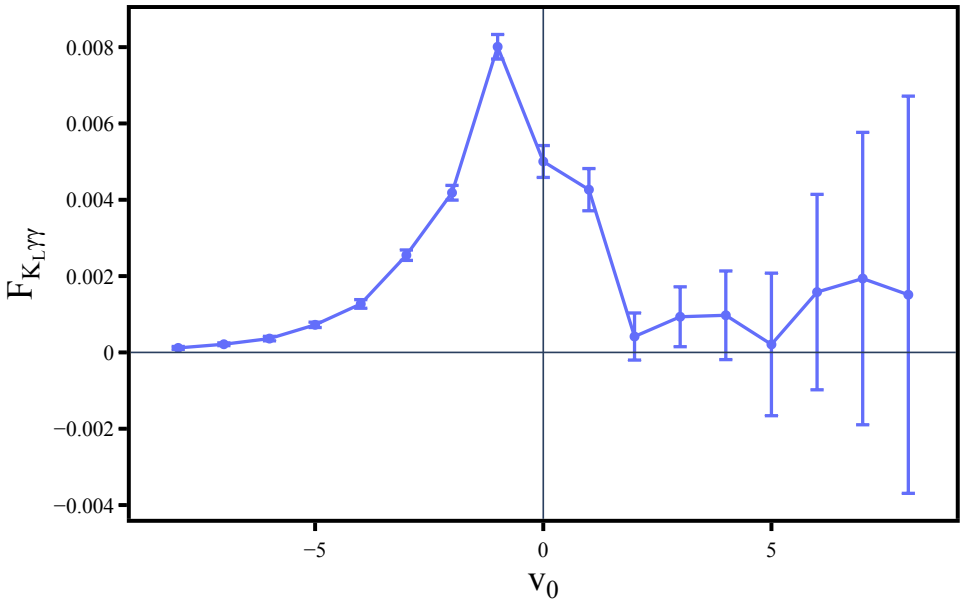

Figure 5.7: Amplitude $F_{K\gamma\gamma}$ v.s. v_0 after subtracting the pion intermediate state. Weak Hamiltonian is fixed at $x_0 = 0$. The positions of kaon wall are averaged in an error weighted-way with the requirement that the separation between electromagnetic current and kaon wall is at least 5 lattice spacings.

omitting the disconnected diagrams is difficult to estimate especially because of the presence of the eta intermediate state.

Our final result is

$$F_{K_L\gamma\gamma} = 0.0129(27)(30)\ \text{GeV}, \tag{5.56}$$

Source	Error
Finite lattice spacing	0.0025
Finite volume	0.00069
Cutoff of v_0	0.00021
Wilson Coefficients	0.0016
Disconnected diagram	-
Total systematic error	0.0030

Table 5.3: Table of systematic errors in $F_{K_L\gamma\gamma}$. The error from disconnected diagrams is hard to estimate and omitted in this table.

where the error in the first parenthesis is the statistical error estimated with the double jack-knife method, and the error in the second parenthesis is the systematic error excluding the error arising from omitting disconnected diagrams. Considering both statistical and systematic errors, the calculated result is about two standard deviations away from the experimental value $F_{K_L\gamma\gamma} = 0.02047(9)\text{GeV}$.

5.7 Disconnected diagrams

The leading order diagrams for the matrix element $\left\langle J_\mu(u)J_\nu(v)H_w(x)K(t_K)\right\rangle$ involve two kinds of disconnected diagrams: the diagrams with one electromagnetic current contracted with itself, and the diagrams with two electromagnetic currents contracted with each other. The latter are referred to as type V diagrams and is shown in Figure D.5.

For the disconnected diagrams with one electromagnetic current contracted with itself, because the electromagnetic current $J_\mu(u)$ or $J_\nu(v)$ is charge conjugation odd and does not carry color charge, it must be connected with the rest of the diagram through at least 3 gluons. Thus, these diagrams are suppressed by a factor of α_s^3, where α_s is the coupling constant of strong interaction. On the other hand, the type V diagrams have two electromagnetic currents contracted with each other which is charge-even and thus can be connected with the rest of the diagram through only 2 gluons. In addition, the diagrams with one electromagnetic current contracted with itself vanish in the leading order of chiral perturbation theory where the masses of quarks are ignored, because the sum of the charges of up, down, and strange quarks is 0. Moreover, in Section 4.5 we calculated the diagrams with one electromagnetic current contracted with itself for the $\pi^0 \to e^+e^-$ decay, where these diagrams are very noisy and their contribution is only about 3% of the connected diagrams. Because of these reasons, we ignore the disconnected diagrams with one electromagnetic current contracted with itself, and only consider the type V diagrams.

The amplitude from the type V diagrams, computed as a function of the time separation between the electromagnetic currents and weak Hamiltonian, is shown in Figure 5.8. If we sum over v_0 from -8 to 4, as was done for the connected diagrams in Section 5.6, the total type V

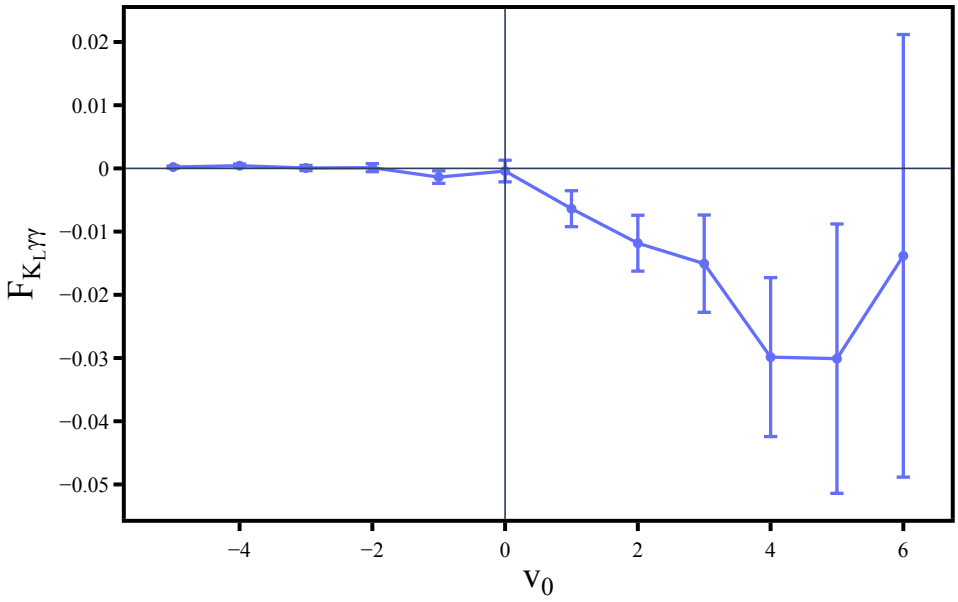

Figure 5.8: Type V diagram contribution to amplitude $F_{K\gamma\gamma}$ v.s. v_0. Weak Hamiltonian is fixed at $x_0 = 0$. The positions of kaon wall are averaged in an error-weighted way with the requirement that the separation between electromagnetic current and kaon wall is at least 5 lattice spacings.

diagram amplitude is -0.057(23), where the error in the parenthesis is statistical. The statistical error is too large to obtain a meaningful result for the total decay amplitude. Thus, we ignored the disconnected diagrams in Section 5.6.

It would be interesting to examine the dependence of the amplitude on the spatial distance between electromagnetic and weak Hamiltonian $R = |\vec{v} - \vec{x}|$. The region with large R contains large noise but small signal. Therefore, if the amplitude forms a plateau at a small value of R, we can set a cutoff at this value to reduce the noise. The plot of type V diagram amplitude against cutoff in R is shown in Figure 5.9, where the position of electromagnetic is integrated to the upper limit $v_0 = 4$. A plateau is formed at roughly $R = 13$ where the amplitude is -0.067(19). and the statistical error is reduced by about 20% compared to the error of total amplitude 0.023. A possible improvement to this method is to subtract the pion intermediate state contribution in the amplitude v.s. R plot, which might make the plateau form at a smaller value of R and thus reduce the statistical error in the cutoff quantity. We can add one-half of the connected diagram amplitude which contains two copies of pion intermediate states into the disconnected diagram amplitude to cancel its pion

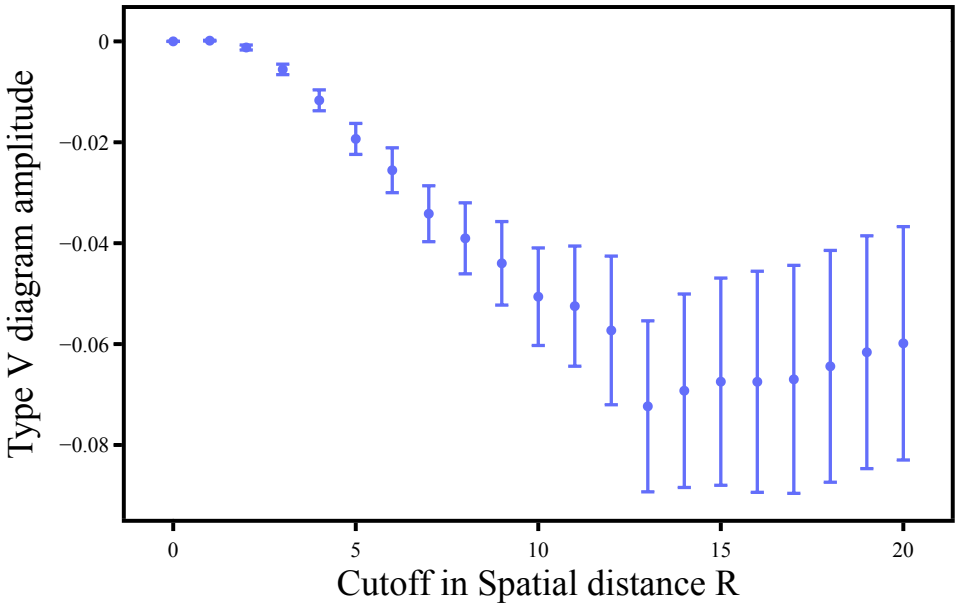

Figure 5.9: Type V diagram contribution to amplitude $F_{K\gamma\gamma}$ v.s. cutoff in $R = |\vec{v} - \vec{x}|$. The x-axis is the cutoff of the spatial distance between weak Hamiltonian and electromagnetic current $J_\nu(v)$. The position of electromagnetic is integrated to upper limit $v_0 = 4$.

intermediate state contribution. The result is shown in Figure 5.10, where the plateau is formed at approximately the same position as the case without subtracting pion intermediate state. Thus, at least for our kinematics, little appears be gained even from this well-implemented introduction of a spatial cutoff.

5.8 Removing the η state

Because of the small difference between eta mass and kaon mass, the unphysical part of the eta state contribution decays with a slow rate behaving as $\exp\left(-(M_\eta - M_K)\,T\right)$ and will bring large errors into the calculation when disconnected diagrams are included. As discussed in Section 5.4.2, we add a total divergence term $c_s(\bar{s}d + \bar{d}s)$ term into the Hamiltonian to remove the η intermediate state. Calculations that involve the η state typically contain large statistical noise because of the presence of the disconnected diagrams. The effective mass plot for η is shown in Figure 5.11, where we use Coulomb gauge-fixed wall source propagators for the η and average over all time

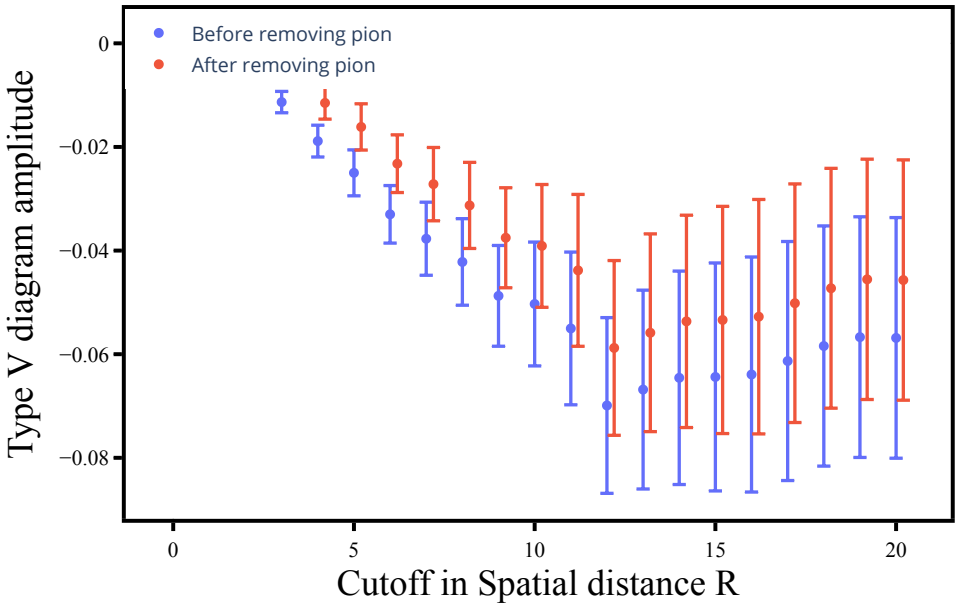

Figure 5.10: Type V diagram contribution to amplitude $F_{K\gamma\gamma}$ v.s. cutoff in $R = |\vec{v} - \vec{x}|$. The position of electromagnetic is integrated to upper limit $v_0 = 4$. The blue points are the amplitude before removing pion, while the red points are the amplitude after removing pion.

slices. The effective mass is calculated as

$$M_{\text{eff}}(t) = \cosh^{-1}\left[\frac{C(t+1) + C(t-1)}{2C(t)}\right], \tag{5.57}$$

where $C(t)$ is the two-point eta-eta correlator function $C(t) = \langle \eta(t)\eta(0)\rangle$. The effective mass at $t = 4$ is 0.546(88) GeV and is close to the actual physical eta mass. The range of fitting is often determined based on the plateau in the plot of effective mass. However, in Figure 5.11 we see a very short "plateau" of 1 or 2 lattice sites at around $t = 4$, which implies that a finer lattice with a smaller lattice spacing is required to obtain a better plateau for the calculations involving the eta state.

5.8.1 Calculating c_s

The coefficient c_s is calculated based on Equation 5.40 from the two three-point correlators $\langle \eta(t_\eta) H_w(x) K^0(t_K)\rangle$ and $\langle \eta(t_\eta) \bar{s}d(x) K^0(t_K)\rangle$. We average $\vec{x}$ on each time slice to increase the statis-

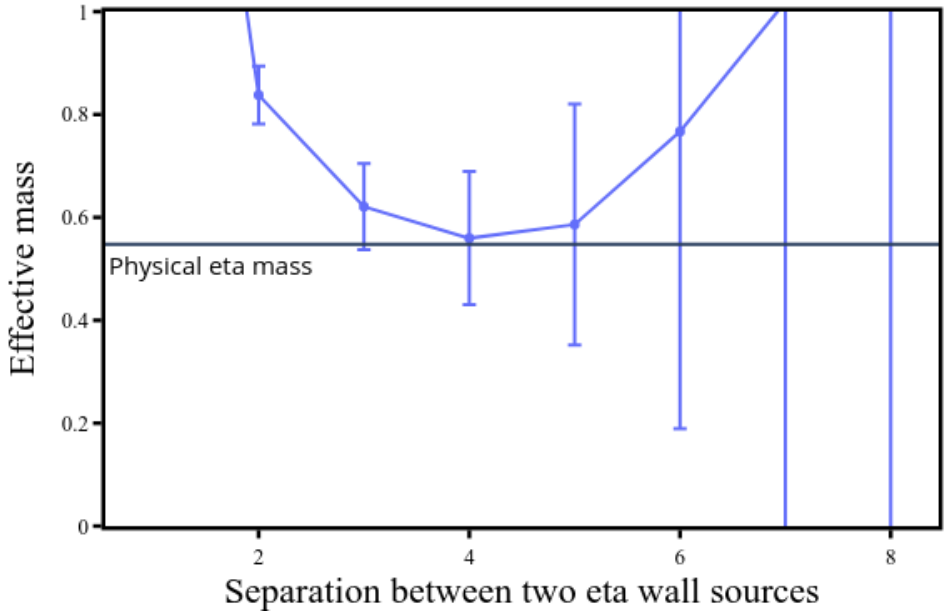

Figure 5.11: Effective mass plot for η state from the $\langle \eta(t)\eta(0)\rangle$ correlator. The black line represents physical eta mass.

tics, and denote the resulting three-point function as $C(t_\eta, t_x, t_K)$. Because the eta state carries large statistical noise, we preserve the distance between eta interpolating operator and t_x and average over other variables to further increase the statistics. Let $\delta = t_\eta - t_x$, we have

$$\overline{C}(\delta) = \left\langle C(t_\eta, t_\eta + \delta, t_K)\right\rangle_{t_\eta, t_K}, \tag{5.58}$$

where the subscript of the right bracket represents that we average over all allowed values of t_η and t_K. In practice, we first average over the center of mass coordinate of three positions t_η, t_x, and t_K, and then perform an error-weighted average of the following values of source-sink separation

$$t_\eta - t_K = \{10, 12, 14, 16, \ldots, 24\}. \tag{5.59}$$

For the 24ID ensemble used in this work, the weights are completely dominated by $t_\eta - t_K = 14, 16, 18, 20$.

The contraction diagrams involved in these two three-point correlators are listed in Appendix D.4

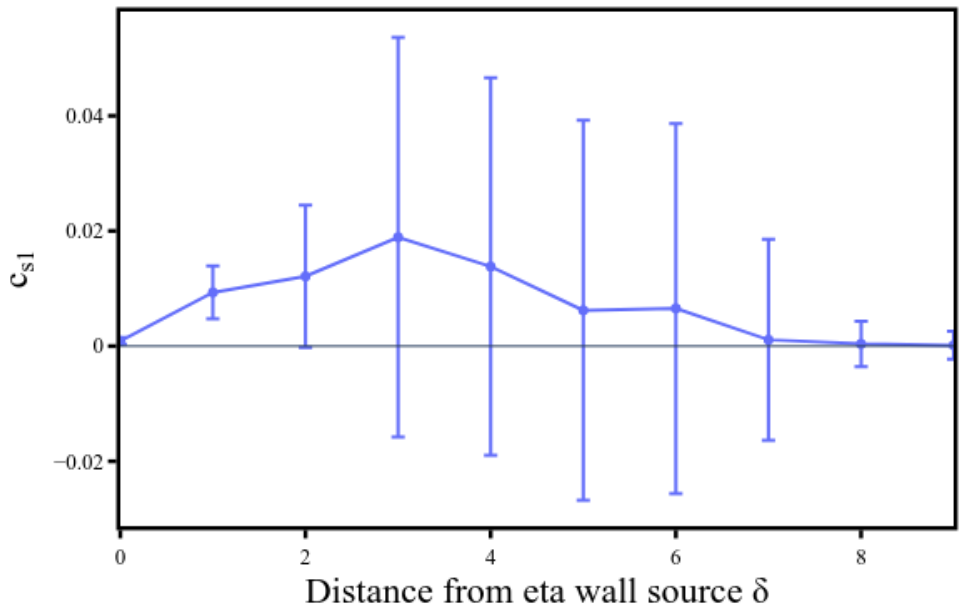

Figure 5.12: Calculated value of c_{s1} plotted as a function of the separation between the $H_w/\bar{s}d$ operator and eta source δ. The positions of the kaon interpolating operator have been averaged in an error-weighted way.

and Appendix D.5. In Figure 5.12 and Figure 5.13, we plot the calculated values of c_{s1} and c_{s2} against $\delta = t_\eta - t_x$ which is the distance from the $H_w/\bar{s}d$ operator to eta interpolating operator

$$c_{s1} = -\frac{\langle \eta | Q_1(x) | K^0 \rangle}{\langle \eta | \bar{s}d(x) | K^0 \rangle} \tag{5.60}$$

$$c_{s2} = -\frac{\langle \eta | Q_2(x) | K^0 \rangle}{\langle \eta | \bar{s}d(x) | K^0 \rangle}. \tag{5.61}$$

Both c_{s1} and c_{s2} contain large statistical noise because of the presence of the disconnected diagrams. At $\delta = 4$, we obtain $c_{s1} = 0.014(33)$ and $c_{s2} = 0.002(13)$. Similar to the type V diagrams, we would need more gauge configuration or a lattice ensemble with smaller lattice spacing to fit the plateau and obtain a meaningful result for c_s.

5.8.2 Calculating amplitude from the $\bar{s}d + \bar{d}s$ operator

After the introduction of the $c_s\left(\bar{s}d + \bar{d}s\right)$ term, we need to calculate an additional contribution to the amplitude from the matrix element $\left\langle J_\mu(u) J_\nu(v) \bar{s}d(0) | K_L \right\rangle$. The leading order diagrams for

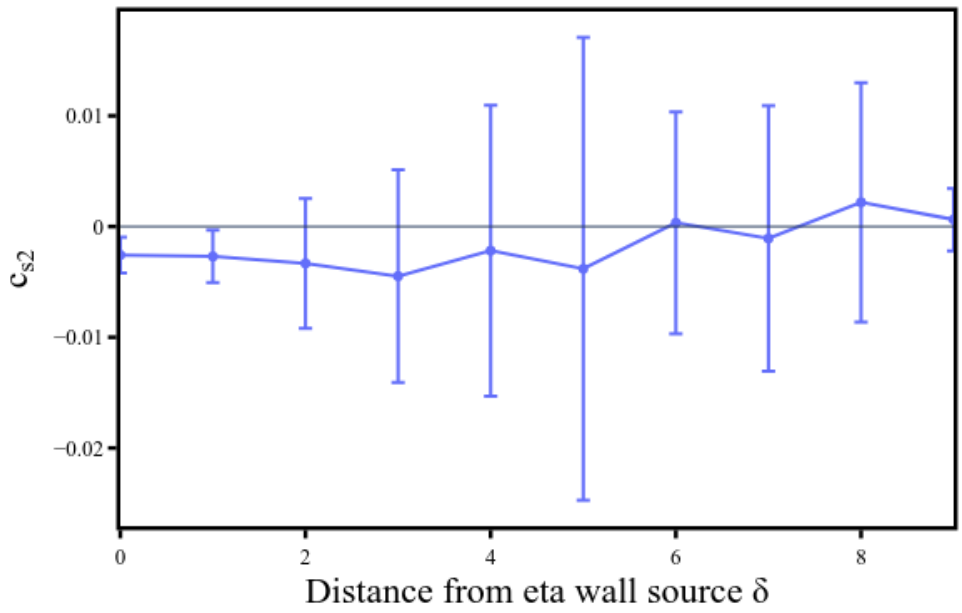

Figure 5.13: Calculated value of c_{s2} plotted as a function of the separation between the $H_w/\bar{s}d$ operator and eta source δ. The positions of the kaon interpolating operator have been averaged in an error-weighted way.

this matrix element are listed in Appendix D.6. The type I, type II, and type III diagrams of $\left\langle J_\mu(u)J_\nu(v)\bar{s}d(0)|K_L\right\rangle$ are calculated in the same way as the type II, type IV, and type V diagrams of $\left\langle J_\mu(u)J_\nu(v)H_w(0)|K_L\right\rangle$, respectively.

If we ignore the disconnected diagrams, we can compute the contribution of this new $\bar{s}d$ operator to the decay $K_L \to \gamma\gamma$ in the same way as our earlier calculation of the contribution of H_W. This will also require dealing with the unphysical contribution of the pion intermediate state as discussed in Section 5.4.1. The $K \to \gamma\gamma$ amplitude resulting from the $\bar{s}d$ operator alone plotted against v_0 is shown in Figure 5.14, where there is clear exponential increase arising from the unphysical pion intermediate state contribution. Note we expect a non-zero $\bar{s}d$ contribution to the unphysical pion intermediate state amplitude because this amplitude does not conserve energy. After subtracting the pion intermediate state contribution on each time slice, the exponential increase is removed and the plot of amplitude is shown in Figure 5.15. This also shows a non-zero value because although this is now a part of the physical, energy-conserving $K_L \to \gamma\gamma$ decay we have also removed the physical contribution of the π^0 intermediate state to that decay, as discussed in

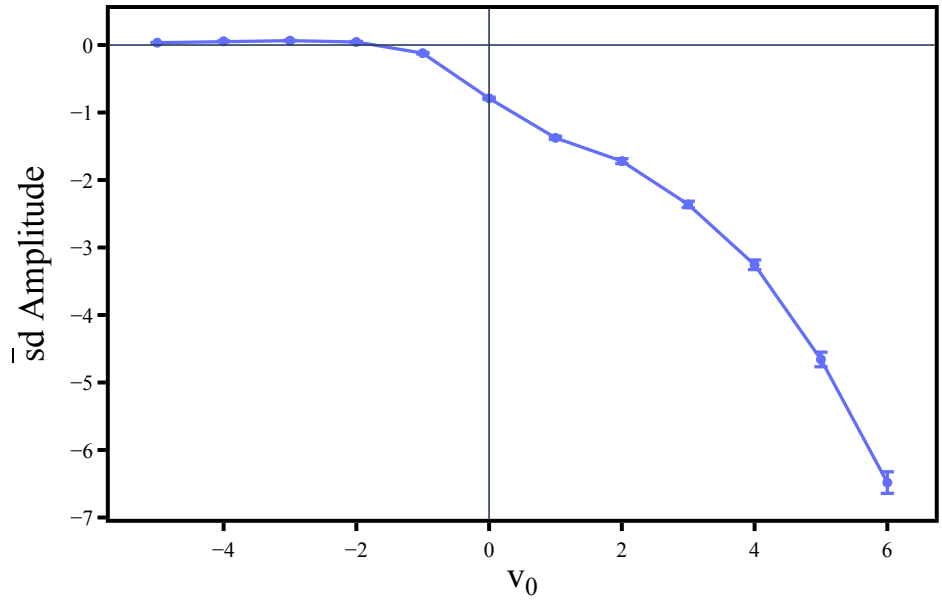

Figure 5.14: Connected diagram amplitude from the $\bar{s}d$ term plotted as a function of v_0.

Section 5.4.1. Finally, we add back the physical part of the pion intermediate state contribution calculated to be 1.93(3), and obtain the final amplitude -0.95(90) by summing over v_0 with the upper limit $v_0 = 8$. The amplitude from the $\bar{s}d$ term should be 0 because it is a total divergence term. Therefore, this calculation serves as a test of our procedure of removing the unphysical part of the pion contribution.

The amplitude of the disconnected diagram, as shown in Figure 5.16, again contains large statistical noise, and requires more gauge configurations and a finer lattice to calculate it.

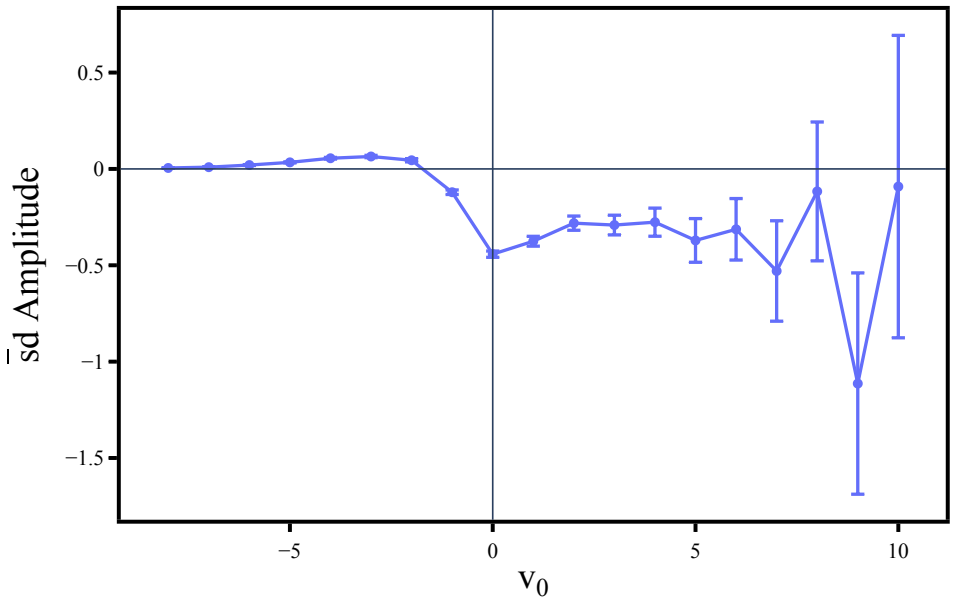

Figure 5.15: Amplitude from the $\bar{s}d$ term plotted as a function of v_0, after subtracting the pion intermediate state contribution on each time slice.

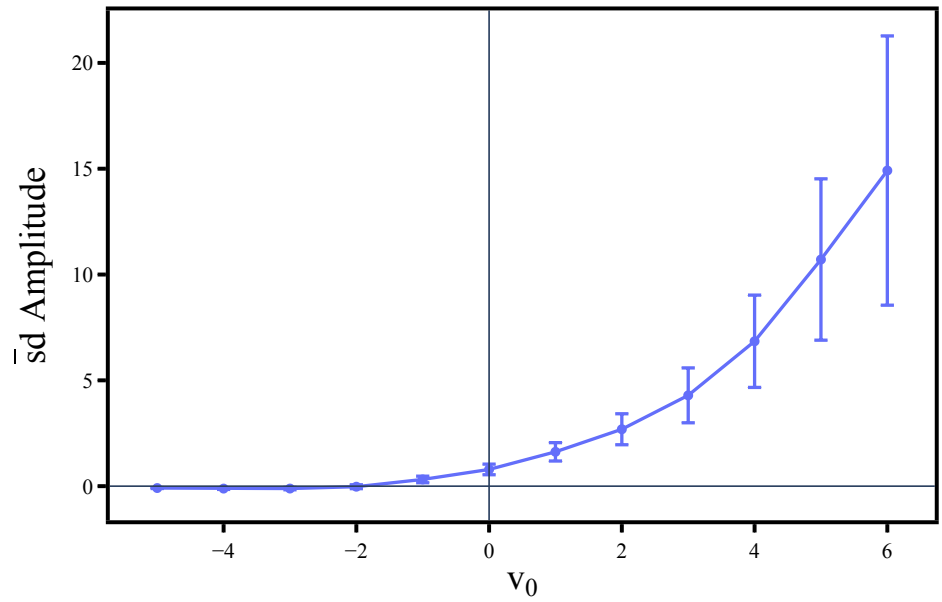

Figure 5.16: Disconnected diagram amplitude of the $\bar{s}d$ term plotted as a function of v_0.

Conclusion and outlook

In this work, we develop computational strategies and perform the first first-principles calculation of the $\pi^0 \to e^+e^-$ and $K_L \to \gamma\gamma$ decay amplitudes. The successful lattice calculation of these two processes establishes a theoretical foundation for the future calculation of a more complicated process, the two-photon contribution to the rare kaon decay $K_L \to \mu^+\mu^-$, which should serve as an important test of the standard model at one-loop.

In the calculation of the $\pi^0 \to e^+e^-$ decay, we develop a general computational strategy for dealing with the two-photon intermediate state. By combining Minkowski- and Euclidean-space methods we are able to calculate the complex amplitude describing this decay directly from the underlying theories of QCD and QED. The leading connected and disconnected diagrams that enter this decay are computed. A continuum limit amplitude is extrapolated from two ensembles 48I and 64I with an inverse lattice spacing $a^{-1} = 1.73$ GeV and $a^{-1} = 2.36$ GeV, respectively. The systematic errors in the calculation include finite volume error, error from Z_V, and estimated error from omitting disconnected diagrams. We find $\mathrm{Re}\mathcal{A} = 18.60(1.19)(1.04)$ eV, $\mathrm{Im}\mathcal{A} = 32.59(1.50)(1.65)$ eV and a more precise value for their ratio $\frac{\mathrm{Re}\mathcal{A}}{\mathrm{Im}\mathcal{A}} = 0.571(10)(4)$ where $\mathcal{A}$ is the decay amplitude, the error in the first parenthesis is statistical, and the error in the second parenthesis is systematic. Using the more precise ratio of amplitudes we obtain the branching ratio $B\left(\pi^0 \to e^+e^-\right) = 6.30(5)(2)\times 10^{-8}$ which falls within two standard deviations of the experimental branching ratio $B\left(\pi^0 \to e^+e^-\right)_{\mathrm{exp}} = 6.87(36)\times 10^{-8}$.

Next, we compute the $K_L \to \gamma\gamma$ decay amplitude. The emitted photons are treated in infinite volume and the decay amplitude is decomposed into an analytically known electromagnetic part

and a hadronic part given by the matrix element of the product of two electromagnetic currents and weak Hamiltonian evaluated between the K_L state and the vacuum. The matrix element is computed using lattice methods, with the unphysical part of the pion intermediate state contribution directly subtracted. We obtain calculated decay amplitude $\mathcal{F}_{K_L\gamma\gamma} = 0.0129(27)(30)$ GeV where the error in the first parenthesis is statistical and the error in the second parenthesis is the systematic error that includes finite lattice spacing and finite volume error but does not include the error from leaving out the disconnected diagrams. Considering both statistical and systematic errors, this result is about two standard deviations lower than the experimental value $\mathcal{F}^{\text{exp}}_{K_L\gamma\gamma} = 0.02047(9)$ GeV. The calculated amplitude is incomplete because the contribution of the disconnected diagrams has not been included. While we have computed what we expect to be the leading disconnected diagram, the type V diagram shown in Figure D.5, the results have large statistical errors. Because of the near degeneracy of the kaon and η mesons, we must also remove the η intermediate state by adding an $\overline{s}d + \overline{d}s$ term to H_W, an added complication made more difficult by the large statistical noise from disconnected diagrams.

A more extensive calculation will be needed to determine the disconnected diagram contribution in the $K_L \to \gamma\gamma$ decay. We may need to add more gauge configurations to the current calculation or to work at a much smaller lattice spacing, as has been done in the calculation of ΔM_K where meaningful results for the disconnected diagrams have been obtained [27]. Our goal of computing the two-photon contribution to $K_L \to \mu^+\mu^-$ decay will also require that the statistical noise present in the disconnected parts be controlled.

In addition, it will also be necessary to develop additional techniques to treat the $\pi\pi\gamma$ intermediate state. While in the $K_L \to \gamma\gamma$ case the two-pion state must carry the momentum of one of the photons and has energy greater than the initial kaon, this is no longer true for the two-muon decay and the effects of this three-particle state must be understood. These effects include both the unphysical exponentially growing terms that arise because the energy of the $\pi\pi\gamma$ can be less than M_K and the potentially large finite-volume errors that can arise from kinematics where the $\pi\pi\gamma$ has energy close to M_K. Treating this second effect will require a generalization of the two-particle

analysis given in Ref. [35]. Thus, considerable further effort will be needed before the two-photon contribution to $K_L \to \mu^+\mu^-$ can be computed.

References

[1] M. Tanabashi *et al.*, "Review of Particle Physics," *Phys. Rev.*, vol. D98, no. 3, p. 030 001, 2018.

[2] V. Cirigliano, G. Ecker, H. Neufeld, A. Pich, and J. Portoles, "Kaon Decays in the Standard Model," *Rev. Mod. Phys.*, vol. 84, p. 399, 2012. arXiv: 1107.6001 [hep-ph].

[3] K. G. Wilson, "Confinement of quarks," *Phys. Rev. D*, vol. 10, pp. 2445–2459, 8 1974.

[4] Y. Iwasaki, "Renormalization group analysis of lattice theories and improved lattice action: Two-dimensional non-linear O(N) sigma model," *Nuclear Physics B*, vol. 258, pp. 141–156, 1985.

[5] D. B. Kaplan, "A method for simulating chiral fermions on the lattice," *Physics Letters B*, vol. 288, no. 3-4, pp. 342347, 1992.

[6] R. C. Brower, H. Neff, and K. Orginos, "The möbius domain wall fermion algorithm," 2014. arXiv: 1206.5214 [hep-lat].

[7] G. Buchalla, A. J. Buras, and M. E. Lautenbacher, "Weak decays beyond leading logarithms," *Reviews of Modern Physics*, vol. 68, no. 4, pp. 11251244, 1996.

[8] G. Martinelli, C. Pittori, C. Sachrajda, M. Testa, and A. Vladikas, "A general method for non-perturbative renormalization of lattice operators," *Nuclear Physics B*, vol. 445, no. 1, pp. 81105, 1995.

[9] C. Lehner and C. Sturm, "Matching factors for $\Delta S = 1$ four-quark operators in RI/SMOM schemes," *Physical Review D*, vol. 84, no. 1, 2011.

[10] G. Buchalla, A. J. Buras, and M. E. Lautenbacher, "Weak decays beyond leading logarithms," *Reviews of Modern Physics*, vol. 68, no. 4, pp. 11251244, 1996.

[11] P. Zyla *et al.*, "Review of Particle Physics," *PTEP*, vol. 2020, no. 8, p. 083C01, 2020.

[12] Y. Zhao, N. H. Christ, X. Feng, L. Jin, and C. Tu, "Calculating the Two-photon Contribution to $\pi^0 \to e^+e^-$ Decay Amplitude," in *Proceedings, 37th International Symposium on Lattice Field Theory (Lattice 2019)*, vol. LATTICE2019, 2019, p. 097.

[13] J. Vaško Petrand Novotný, "Two-loop qed radiative corrections to the decay $\pi^0 \to e^+e^-$: The virtual corrections and soft-photon bremsstrahlung," *Journal of High Energy Physics*, vol. 2011, no. 10, p. 122, 2011.

[14] T. Husek, K. Kampf, and J. Novotný, "Rare decay $\pi^0 \to e^+e^-$: On corrections beyond the leading order," *The European Physical Journal C*, vol. 74, no. 8, p. 3010, 2014.

[15] S. D. Drell, "Direct decay $\pi^0 \to e^+e^-$," *Il Nuovo Cimento (1955-1965)*, vol. 11, no. 5, pp. 693–697, 1959.

[16] E. Weil, G. Eichmann, C. S. Fischer, and R. Williams, "Electromagnetic decays of the neutral pion," *Phys. Rev. D*, vol. 96, p. 014 021, 1 2017.

[17] A. E. Dorokhov, "Rare decay $\pi^0 \to e^+e^-$ as a test of standard model," *Physics of Particles and Nuclei Letters*, vol. 7, pp. 229–234, 2009.

[18] T. Blum, P. A. Boyle, T. Izubuchi, L. Jin, A. Jüttner, C. Lehner, K. Maltman, M. Marinkovic, A. Portelli, and M. Spraggs, "Calculation of the hadronic vacuum polarization disconnected contribution to the muon anomalous magnetic moment," *Phys. Rev. Lett.*, vol. 116, no. 23, p. 232 002, 2016. arXiv: 1512.09054 [hep-lat].

[19] M. A. Clark, C. Jung, and C. Lehner, "Multi-Grid Lanczos," *EPJ Web Conf.*, vol. 175, p. 14 023, 2018. arXiv: 1710.06884 [hep-lat].

[20] T. Hahn, "Cuba - a library for multidimensional numerical integration," *Computer Physics Communications*, vol. 168, no. 2, pp. 7895, 2005.

[21] T. Blum *et al.*, "Domain wall QCD with physical quark masses," *Phys. Rev.*, vol. D93, no. 7, p. 074 505, 2016. arXiv: 1411.7017 [hep-lat].

[22] P. A. Boyle, N. H. Christ, N. Garron, C. Jung, A. Jüttner, C. Kelly, R. D. Mawhinney, G. McGlynn, D. J. Murphy, S. Ohta, A. Portelli, and C. T. Sachrajda, "Low energy constants of $SU(2)$ partially quenched chiral perturbation theory from $N_f = 2 + 1$ domain wall qcd," *Phys. Rev. D*, vol. 93, p. 054 502, 5 2016.

[23] J. Tu, "Lattice QCD Simulations towards Strong and Weak Coupling Limits," PhD thesis, Columbia U., 2020.

[24] E. Ma and A. Pramudita, "$K_L \to \gamma\gamma$: Theory and phenomenology," *Phys. Rev. D*, vol. 24, pp. 2476–2480, 9 1981.

[25] M. K. Gaillard and B. W. Lee, "Rare decay modes of the K mesons in gauge theories," *Phys. Rev. D*, vol. 10, pp. 897–916, 3 1974.

[26] A. Pramudita, "QCD short-distance enhancement in $K_L \to \gamma\gamma$," *Phys. Rev. D*, vol. 38, pp. 3522–3524, 11 1988.

[27] B. Wang, "Calculation of the $K_L - K_S$ mass difference for physical quark masses," *PoS*, vol. LATTICE2019, p. 093, 2019. arXiv: 2001.06374 [hep-lat].

[28] C. Bernard, T. Draper, A. Soni, H. D. Politzer, and M. B. Wise, "Application of chiral perturbation theory to $K \to 2\pi$ decays," *Phys. Rev. D*, vol. 32, pp. 2343–2347, 9 1985.

[29] G. Feinberg, P. Kabir, and S. Weinberg, "Transformation of muons into electrons," *Phys. Rev. Lett.*, vol. 3, pp. 527–530, 11 1959.

[30] S. Okubo, "ϕ-meson and unitary symmetry model," *Physics Letters*, vol. 5, no. 2, pp. 165–168, 1963.

[31] G Zweig, "An SU_3 model for strong interaction symmetry and its breaking; Version 2," 80 p, 1964.

[32] J. Iizuka, "A Systematics and Phenomenology of Meson Family," *Progress of Theoretical Physics Supplement*, vol. 37-38, pp. 21–34, Mar. 1966. eprint: https://academic.oup.com/ptps/article-pdf/doi/10.1143/PTPS.37.21/5215468/37-38-21.pdf.

[33] N. H. Christ, T. Izubuchi, C. T. Sachrajda, A. Soni, and J. Yu, "Long distance contribution to the $K_L - K_S$ mass difference," *Physical Review D*, vol. 88, no. 1, 2013.

[34] R. Abbott, T. Blum, P. Boyle, M. Bruno, N. Christ, D. Hoying, C. Jung, C. Kelly, C. Lehner, R. Mawhinney, D. Murphy, C. Sachrajda, A. Soni, M. Tomii, and T. Wang, "Direct CP violation and the $\Delta i = 1/2$ rule in $K \to \pi\pi$ decay from the standard model," *Physical Review D*, vol. 102, no. 5, 2020.

[35] N. H. Christ, X. Feng, G. Martinelli, and C. T. Sachrajda, "Effects of finite volume on the K_L-K_S mass difference," *Phys. Rev. D*, vol. 91, no. 11, p. 114 510, 2015. arXiv: 1504.01170 [hep-lat].

Appendix A: Physical constants

Parameter	Value
M_{K_L}	497.611(13) MeV
τ_{K_L}	$(5.116 \pm 0.021) \times 10^{-8}$ s
M_{π^0}	134.9768(5) MeV
τ_{π^0}	$(8.52 \pm 0.18) \times 10^{-17}$ s
M_W	80.379(12) GeV
M_Z	91.1876(21) GeV
G_F	$1.1663787(6) \times 10^{-5} GeV^{-2}$
V_{ud}	0.97446(10)
V_{us}	0.22452(44)
$\alpha = \frac{e^2}{4\pi}$	$\frac{1}{137}$

Table A.1: Physical constants that we used in this work. All values are from the 2020 PDG tables.

Appendix B: Conventions

B.1 Conventions for interpolating operators and states

The interpolating operators used in this work are defined as

$$\pi^0 = \frac{i}{\sqrt{2}}\left(\bar{u}\gamma_5 u - \bar{d}\gamma_5 d\right) \tag{B.1}$$

$$\eta = \frac{i}{\sqrt{6}}\left(\bar{u}\gamma_5 u + \bar{d}\gamma_5 d - 2\bar{s}\gamma_5 s\right) \tag{B.2}$$

$$J_\mu = \frac{2}{3}\bar{u}\gamma_\mu u - \frac{1}{3}\bar{u}\gamma_\mu u - \frac{1}{3}\bar{s}\gamma_\mu s \tag{B.3}$$

$$K^0 = i\bar{d}\gamma_5 s \tag{B.4}$$

$$\overline{K}^0 = i\bar{s}\gamma_5 d \tag{B.5}$$

$$K_L \approx \frac{K^0 + \overline{K}^0}{\sqrt{2}} = i\frac{\bar{d}\gamma_5 s + \bar{s}\gamma_5 d}{\sqrt{2}}. \tag{B.6}$$

For the case of the interpolating operators for the four pseudoscalar operators defined above only their spin and color structure are represented with the individual quark sources taken to be Coulomb gauge fixed wall sources making the interpolating operators non-local in space.

The normalization convention for meson states, using pion as an example, is

$$\langle \pi(p)|\pi(q)\rangle = (2\pi)^3 2E_p \delta^3(\vec{p} - \vec{q}), \tag{B.7}$$

where E_p is the energy of the pion state with momentum p.

B.2 Conventions and properties of gamma matrices

In this work, Euclidean gamma matrices are defined as:

$$\gamma_1 = \begin{pmatrix} 0 & 0 & 0 & i \\ 0 & 0 & i & 0 \\ 0 & -i & 0 & 0 \\ -i & 0 & 0 & 0 \end{pmatrix}, \quad \gamma_2 = \begin{pmatrix} 0 & 0 & 0 & -1 \\ 0 & 0 & 1 & 0 \\ 0 & 1 & 0 & 0 \\ -1 & 0 & 0 & 0 \end{pmatrix} \tag{B.8}$$

$$\gamma_3 = \begin{pmatrix} 0 & 0 & i & 0 \\ 0 & 0 & 0 & -i \\ -i & 0 & 0 & 0 \\ 0 & i & 0 & 0 \end{pmatrix}, \quad \gamma_4 = \begin{pmatrix} 0 & 0 & 1 & 0 \\ 0 & 0 & 0 & 1 \\ 1 & 0 & 0 & 0 \\ 0 & 1 & 0 & 0 \end{pmatrix} \tag{B.9}$$

$$\gamma_5 = \gamma_1\gamma_2\gamma_3\gamma_4 = \begin{pmatrix} 1 & 0 & 0 & 0 \\ 0 & 1 & 0 & 0 \\ 0 & 0 & -1 & 0 \\ 0 & 0 & 0 & -1 \end{pmatrix}. \tag{B.10}$$

In addition, we define

$$\gamma_{L,\mu} = \gamma_\mu(1 - \gamma_5) \tag{B.11}$$

$$\gamma_{R,\mu} = \gamma_\mu(1 + \gamma_5). \tag{B.12}$$

Some important properties of the gamma matrices that are used in this work:

$$\{\gamma_\mu, \gamma_\nu\} = 2\delta_{\mu\nu} I, \ \forall \mu, \nu = 1, 2, 3, 4 \tag{B.13}$$

$$\gamma_\mu^\dagger = \gamma_\mu \tag{B.14}$$

$$\gamma_5^\dagger = \gamma_5 \tag{B.15}$$

$$\gamma_L^\dagger = \gamma_R \tag{B.16}$$

$$\gamma_5 \gamma_L = \gamma_L \tag{B.17}$$

$$\gamma_L \gamma_5 = -\gamma_L. \tag{B.18}$$

B.3 Conventions for Dirac spinors

Let $\chi_+ = (1, 0)^T$ and $\chi_- = (0, 1)^T$. The conventions for spinors are

$$u_+ = \begin{pmatrix} \sqrt{E - p}\chi_+ \\ \sqrt{E + p}\chi_+ \end{pmatrix}, \ u_- = \begin{pmatrix} \sqrt{E + p}\chi_- \\ \sqrt{E - p}\chi_- \end{pmatrix}, v_+ = \begin{pmatrix} \sqrt{E - p}\chi_- \\ -\sqrt{E + p}\chi_- \end{pmatrix}, \ v_- = \begin{pmatrix} \sqrt{E + p}\chi_+ \\ -\sqrt{E - p}\chi_+ \end{pmatrix}, \tag{B.19}$$

where "+" denotes spin $\frac{1}{2}$ and "−" denotes spin $-\frac{1}{2}$.

The normalization conventions for spinors are

$$\bar{u}^r(p) u^s(p) = 2m\delta^{rs} \tag{B.20}$$

$$\bar{v}^r(p) v^s(p) = -2m\delta^{rs}. \tag{B.21}$$

B.4 Conventions of Fourier transform

In this thesis, the conventions of Fourier transform and inverse Fourier transform are

$$\tilde{f}(k) = \sum_x f(x) e^{-i\frac{2\pi}{N}kx} \tag{B.22}$$

$$f(x) = \frac{1}{N} \sum_k \tilde{f}(k) e^{i\frac{2\pi}{N}kx}. \tag{B.23}$$

Appendix C: Useful integrals

In this section, we show some integrals that are used in calculating the leptonic factor of the $\pi^0 \to e^+e^-$ decay in Section 4.4.

From Equation 4.34 to Equation 4.36, we average over the direction of $\vec{k}_-$ in three-dimensional space using the following integrals

$$\frac{1}{4\pi}\int d\Omega' \frac{1}{-M_\pi + 2|\vec{p}_-|\cos\theta'} = -\frac{1}{4|\vec{p}_-|}\ln(\frac{1+\beta}{1-\beta}) \tag{C.1}$$

$$\frac{1}{4\pi}\int d\Omega' \frac{1}{M_\pi + 2|\vec{p}_-|\cos\theta'} = \frac{1}{4|\vec{p}_-|}\ln(\frac{1+\beta}{1-\beta}), \tag{C.2}$$

where $d\Omega' = d\cos\theta' d\phi'$ is the surface area element on the unit sphere, and β is a constant defined as

$$\beta = \frac{2|\vec{k}_-|}{M_\pi} = \sqrt{1 - \frac{4m_e^2}{M_\pi^2}}. \tag{C.3}$$

From Equation 4.36 to Equation 4.37, we integrate out the direction of $\vec{p}$ in three-dimensional space and need to calculate an integral of the following form

$$\int d^3\vec{p} f(|\vec{p}|) p_i e^{-i\vec{p}\cdot\vec{w}}, \tag{C.4}$$

where $f(|\vec{p}|)$ is a function of the norm of $\vec{p}$. We write $p_i e^{-i\vec{p}\cdot\vec{w}}$ as a derivative of $e^{-i\vec{p}\cdot\vec{w}}$ with respect

to w_i and then exchange the order of integration and differentiation

$$\begin{aligned}
\int d^3\vec{p} f(|\vec{p}|) p_i e^{-i\vec{p}\cdot\vec{w}} &= i\frac{\partial}{\partial w_i}\int d^3\vec{p} f(|\vec{p}|) e^{-i\vec{p}\cdot\vec{w}} \\
&= 2\pi i\frac{\partial}{\partial w_i}\int d|\vec{p}| d\cos\theta\ |\vec{p}|^2 f(|\vec{p}|) e^{-i|\vec{p}||\vec{w}|\cos\theta} \\
&= 2\pi i\frac{\partial}{\partial w_i}\int d|\vec{p}|\ |\vec{p}|^2 f(|\vec{p}|)\frac{2\sin(|\vec{p}||\vec{w}|)}{|\vec{p}||\vec{w}|} \\
&= 4\pi i\frac{w_i}{|\vec{w}|^2}\int d|\vec{p}|\ |\vec{p}|^2 f(|\vec{p}|)\left(\cos(|\vec{p}||\vec{w}|) - \frac{\sin(|\vec{p}||\vec{w}|)}{|\vec{p}||\vec{w}|}\right). \qquad \text{(C.5)}
\end{aligned}$$

Appendix D: Diagrams

In this Appendix, we list the diagrams involved in the calculation of the $K_L \to \gamma\gamma$ decay. The diagrams are drawn with the following conventions

- The dotted line is the position of the kaon/pion/eta wall. When there are two mesons in the diagram, the kaon wall is always on the left.
- The dark lines with label s represent strange quark propagators, and the dark lines without label s represent light quark propagators.
- The circle with a cross inside represents the position of the weak Hamiltonian or the $\bar{s}d$ operator.
- Diagram (a) and Diagram (b) are identical except that the positions of two electromagnetic currents u and v are exchanged.

D.1 Diagrams for $\langle J_\mu(u)J_\nu(v)H(x)K_L(t_K)\rangle$

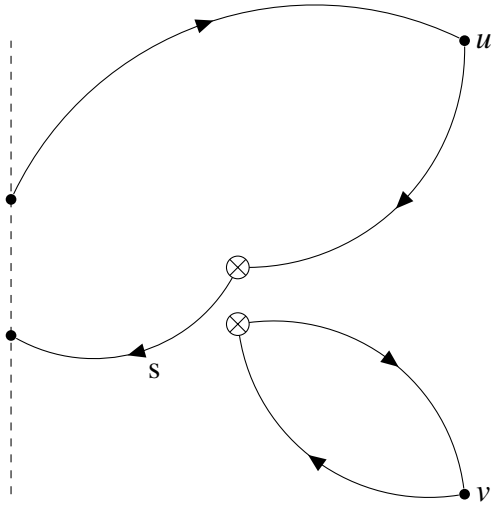

(a) Type I diagram 1(a)

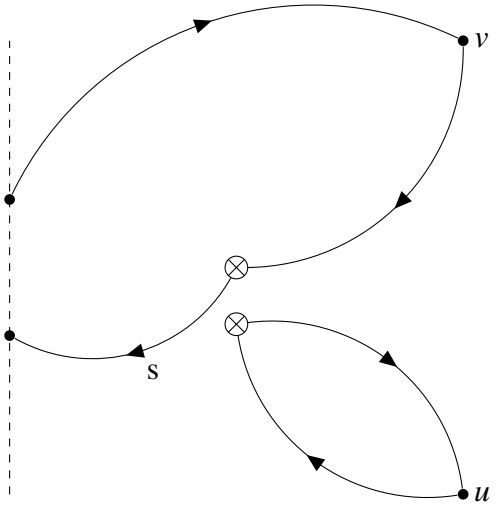

(b) Type I diagram 1(b)

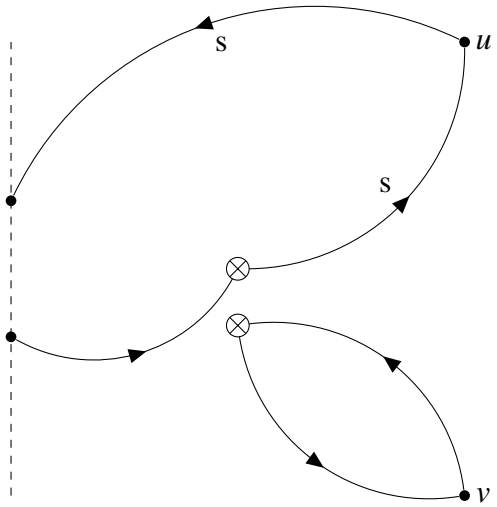

(c) Type I diagram 2(a)

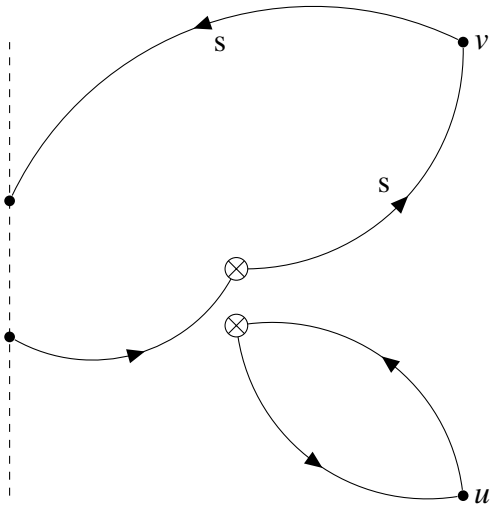

(d) Type I diagram 2(b)

Figure D.1: $\langle J_\mu(u)J_\nu(v)H_w(x)K^0(t_K)\rangle$ Type I diagrams

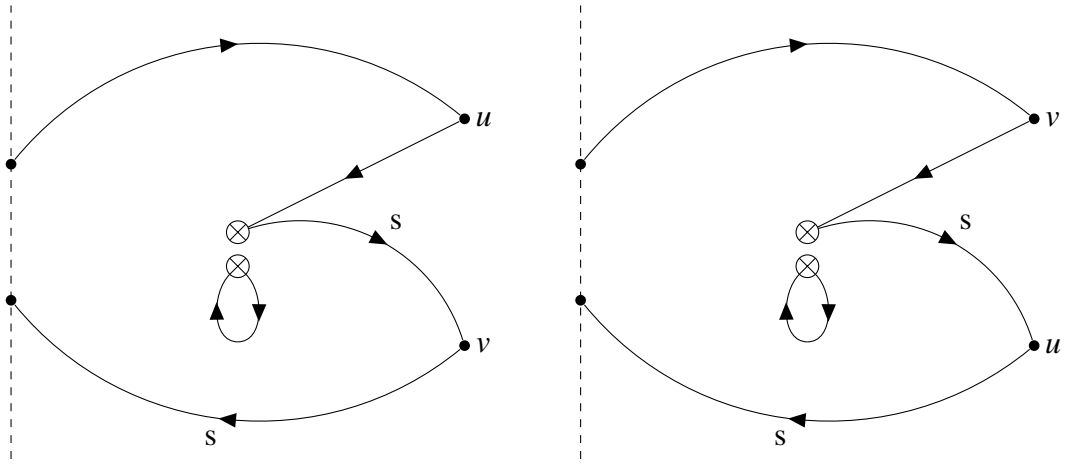

(a) Type II diagram 1(a) (b) Type II diagram 1(b)

Figure D.2: $\langle J_\mu(u)J_\nu(v)H_w(x)K^0(t_K)\rangle$ Type II diagrams

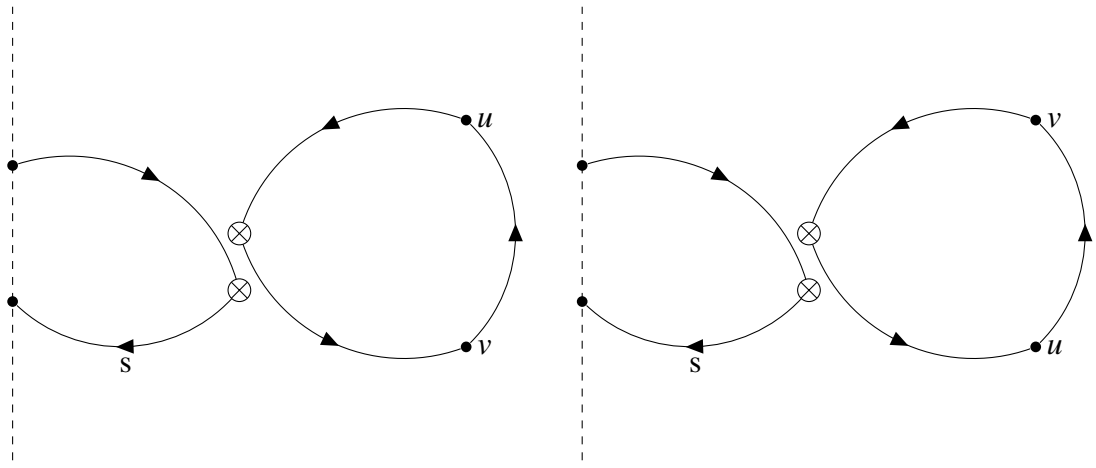

(a) Type III diagram 1(a) (b) Type III diagram 1(b)

Figure D.3: $\langle J_\mu(u)J_\nu(v)H_w(x)K^0(t_K)\rangle$ Type III diagrams

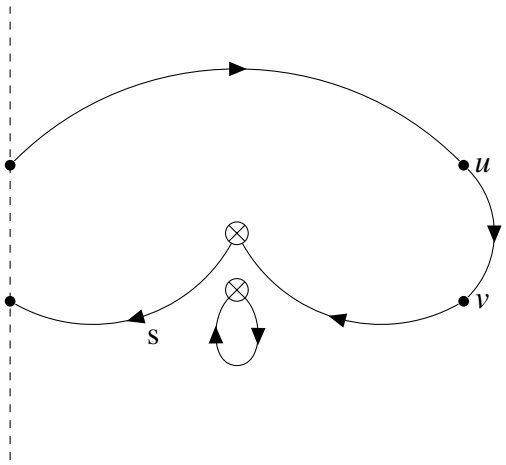

(a) Type IV diagram 1(a)

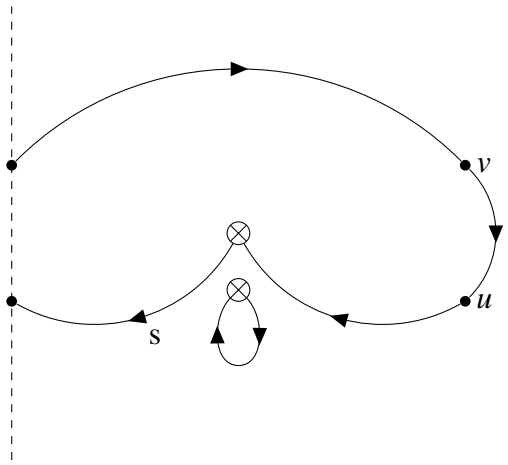

(b) Type IV diagram 1(b)

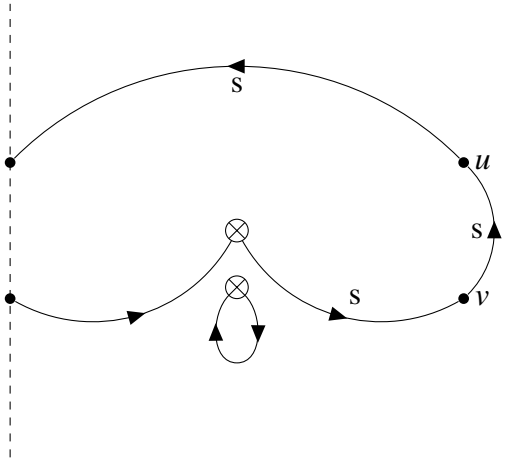

(c) Type IV diagram 2(a)

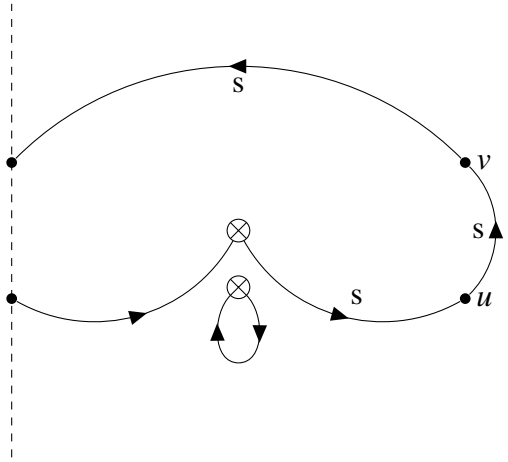

(d) Type IV diagram 2(b)

Figure D.4: $\langle J_\mu(u)J_\nu(v)H_w(x)K^0(t_K)\rangle$ Type IV diagrams

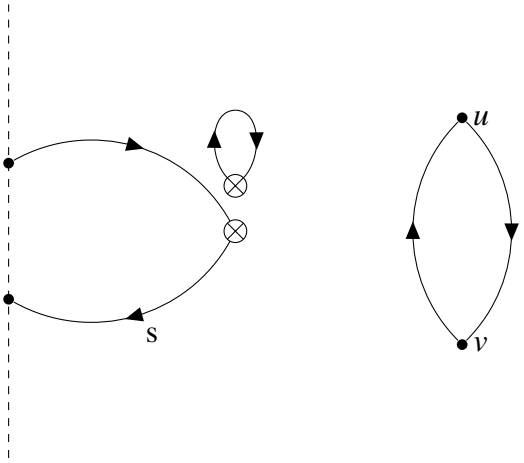

(a) Type V diagram 1

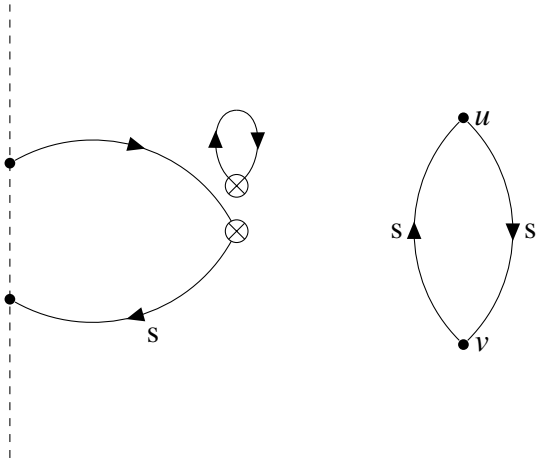

(b) Type V diagram 2

Figure D.5: $\langle J_\mu(u)J_\nu(v)H_w(x)K^0(t_K)\rangle$ Type V diagrams

D.2 Diagrams for $\langle J_\mu(u)J_\nu(v)\pi^0(t_\pi)\rangle$

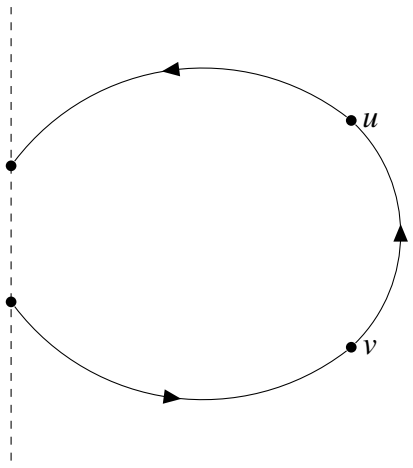

Figure D.6: $\langle J_\mu(u)J_\nu(v)\pi^0(t_\pi)\rangle$ diagram

D.3 Diagrams for $\langle \pi^0(t_\pi) H_w(x) K^0(t_K) \rangle$

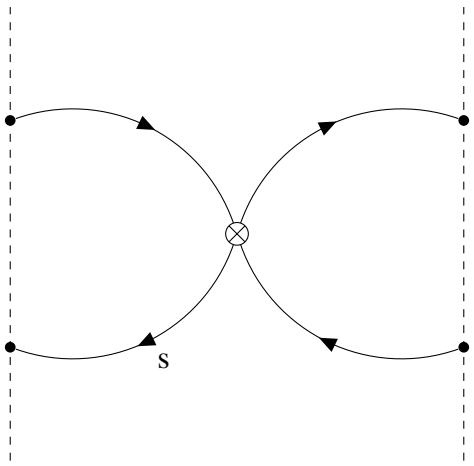

Figure D.7: $\langle \pi^0(t_\pi) H_w(x) K^0(t_K) \rangle$ Type I diagram

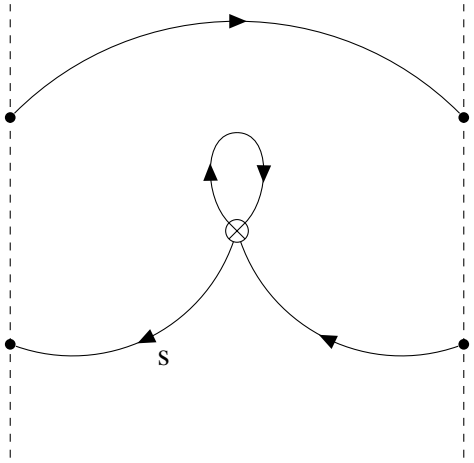

Figure D.8: $\langle \pi^0(t_\pi) H_w(x) K^0(t_K) \rangle$ Type II diagrams

D.4 Diagrams for $\langle 0|\eta(t_\eta)\bar{s}d(x)K^0(t_K)|0\rangle$

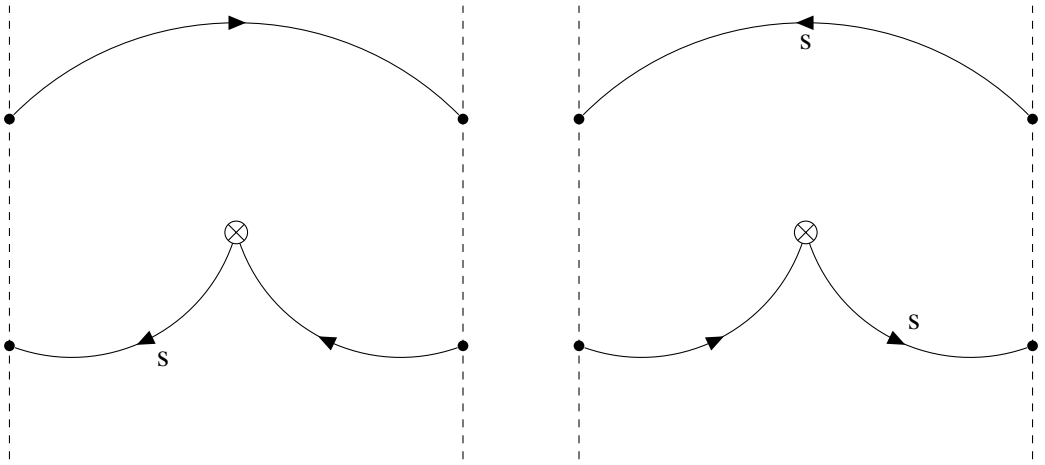

(a) Type I diagram 1 (b) Type I diagram 2

Figure D.9: $\langle 0|\eta(t_\eta)\bar{s}d(x)K^0(t_K)|0\rangle$ Type I diagrams

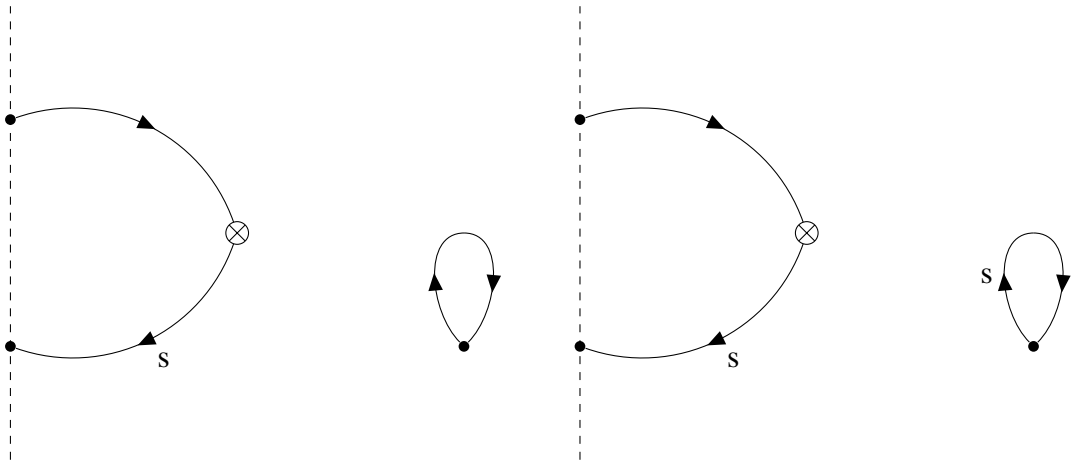

(a) Type II diagram 1 (b) Type II diagram 2

Figure D.10: $\langle 0|\eta(t_\eta)\bar{s}d(x)K^0(t_K)|0\rangle$ Type II diagrams

D.5 Diagrams for $\langle \eta(t_\eta) H_w(x) K^0(t_K) \rangle$

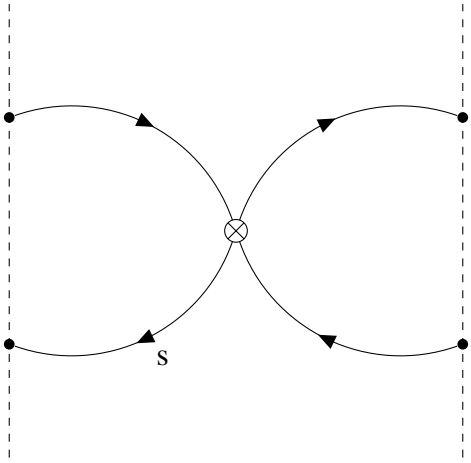

Figure D.11: $\langle \eta(t_\eta) H_w(x) K^0(t_K) \rangle$ Type I diagram

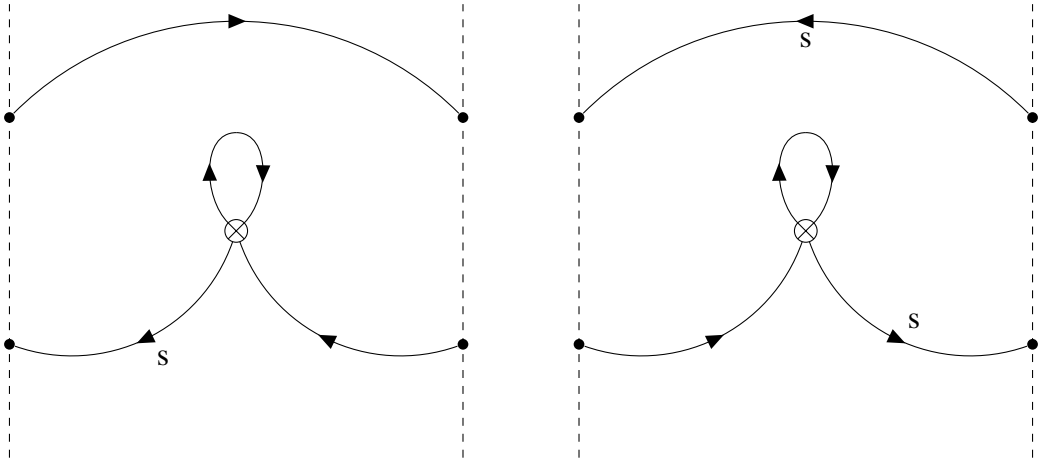

(a) Type II diagram 1 (b) Type II diagram 2

Figure D.12: $\langle \eta(t_\eta) H_w(x) K^0(t_K) \rangle$ Type II diagrams

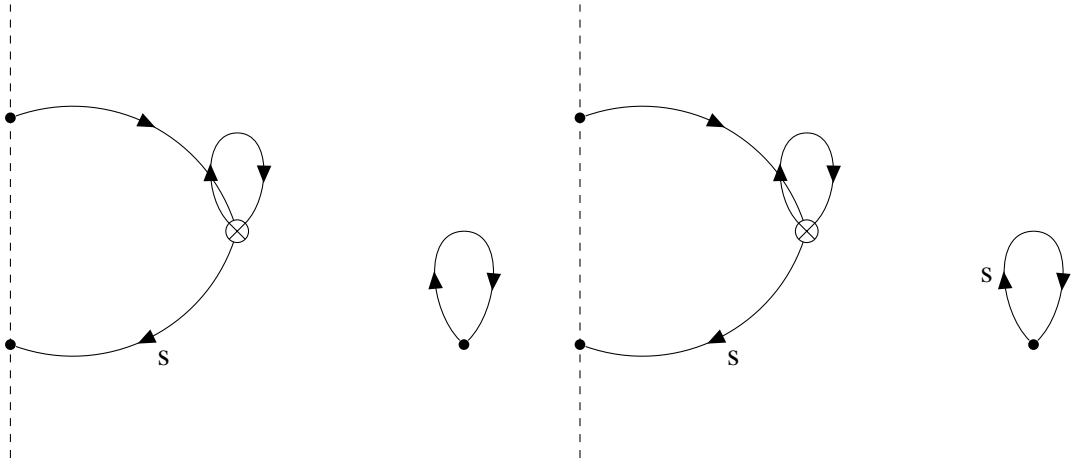

(a) Type III diagram 1

(b) Type III diagram 2

Figure D.13: $\langle \eta(t_\eta) H_w(x) K^0(t_K) \rangle$ Type III diagrams

D.6 Diagrams for $\langle J_\mu(u) J_\nu(v) \bar{s} d(x) K^0(t_K) \rangle$

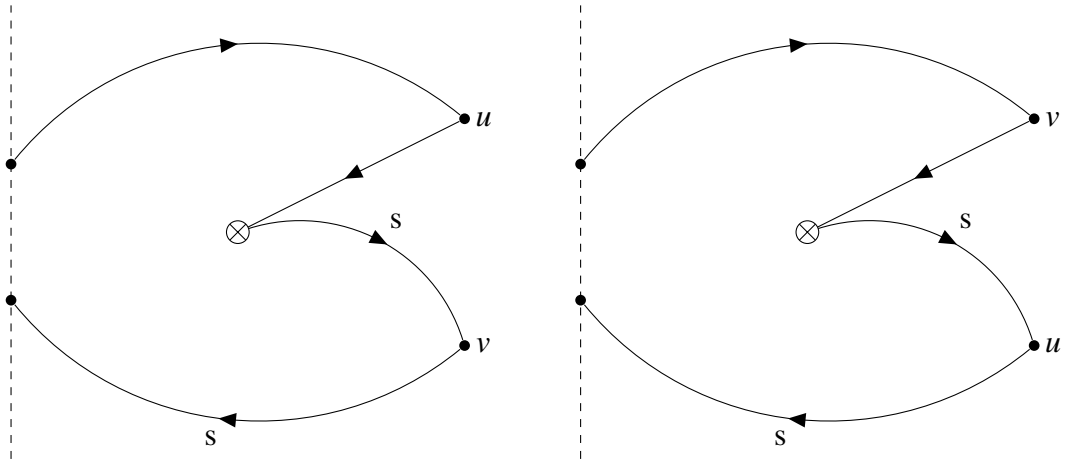

(a) Type I diagram 1(a)

(b) Type I diagram 1(b)

Figure D.14: $\langle J_\mu(u) J_\nu(v) \bar{s} d(x) K^0(t_K) \rangle$ Type I diagrams

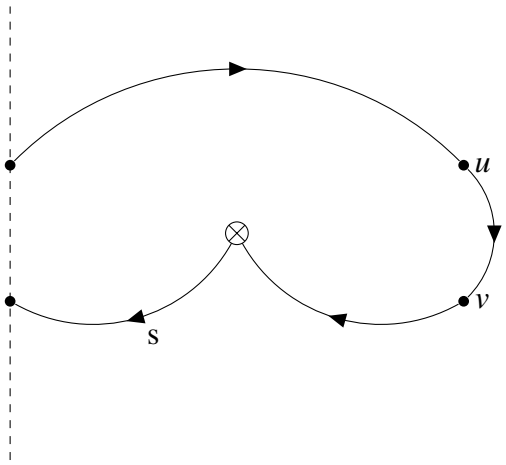

(a) Type II diagram 1(a)

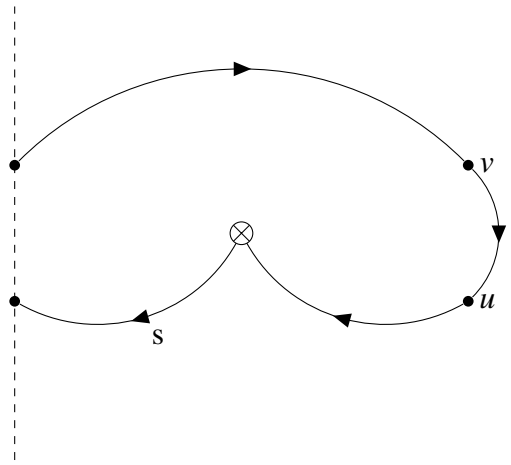

(b) Type II diagram 1(b)

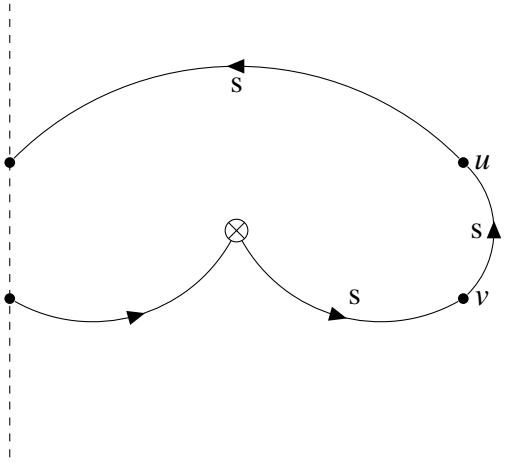

(c) Type II diagram 2(a)

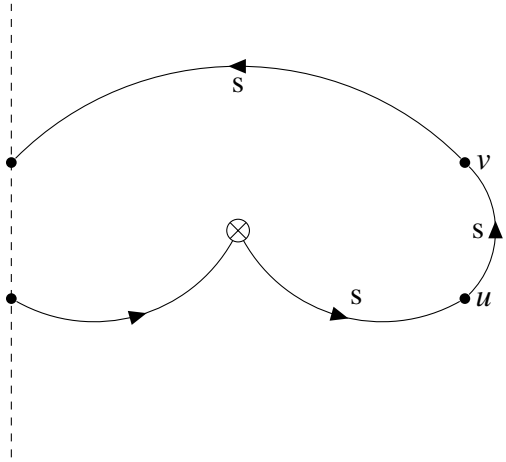

(d) Type II diagram 2(b)

Figure D.15: $\langle J_\mu(u) J_\nu(v) \bar{s}d(x) K^0(t_K) \rangle$ Type II diagrams

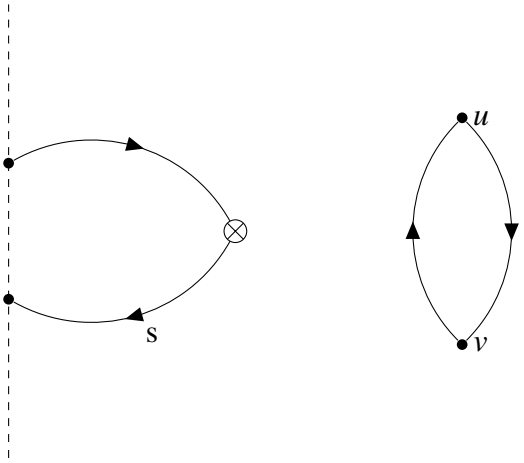

(a) Type III diagram 1

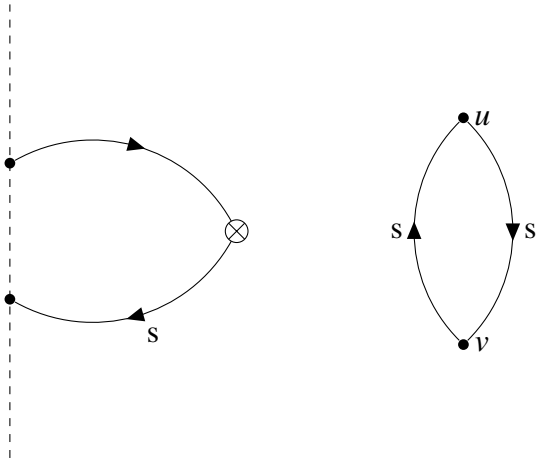

(b) Type III diagram 2

Figure D.16: $\langle J_\mu(u) J_\nu(v) \bar{s}d(x) K^0(t_K) \rangle$ Type III diagrams

Appendix E: Contractions

In this Appendix, we list the contractions and their coefficients for each diagram involved in the calculation of the $K_L \to \gamma\gamma$ decay. We use the following conventions

- The light quark propagators are denoted as L.
- The heavy quark propagators are denoted as H.
- "Tr" represents the trace on color and spin indices, while "Tr_S" represents the trace on spin indices only.
- If a type of diagrams has diagram (a) and diagram (b), we only list the contractions and coefficients for diagram (a). Its counterpart diagram (b) has the same coefficients and can be obtained by switching (u, μ) with (v, ν).

E.1 Contractions for $\langle J_\mu(u)J_\nu(v)H(x)K_L(t_K)\rangle$

	Q_1	Q_2
K^0	$-\frac{2}{9}Tr[\gamma_L L(x,v)\gamma_\nu L(v,x)]$ $Tr[\gamma_L L(x,u)\gamma_\mu L(u,t_K)\gamma_5 H(t_K,x)]$	$-\frac{2}{9}Tr_S[\gamma_L L(x,v)\gamma_\nu L(v,x)]_{c_1,c_2}$ $Tr_S[\gamma_L L(x,u)\gamma_\mu L(u,t_K)\gamma_5 H(t_K,x)]_{c_2,c_1}$
$\overline{K}^0$	$-\frac{2}{9}Tr[\gamma_L L(x,v)\gamma_\nu L(v,x)]$ $Tr[\gamma_L[L(x,u)\gamma_\mu L(u,t_K)\gamma_5 H(t_K,x)]^\dagger]$	$-\frac{2}{9}Tr_S[\gamma_L L(x,v)\gamma_\nu L(v,x)]_{c_1,c_2}$ $Tr_S[\gamma_L[L(x,u)\gamma_\mu L(u,t_K)\gamma_5 H(t_K,x)]^\dagger]_{c_2,c_1}$

Table E.1: Contractions for $\langle J_\mu(u)J_\nu(v)H_w(x)K_L(t_K)\rangle$ type I diagram 1(a)

	Q_1	Q_2
K^0	$-\frac{2}{9}Tr[\gamma_L L(x,v)\gamma_\nu L(v,x)]$ $Tr[\gamma_L L(x,t_K)\gamma_5 H(t_K,u)\gamma_\mu H(u,x)]$	$-\frac{2}{9}Tr_S[\gamma_L L(x,v)\gamma_\nu L(v,x)]_{c_1,c_2}$ $Tr_S[\gamma_L L(x,t_K)\gamma_5 H(t_K,u)\gamma_\mu H(u,x)]_{c_2,c_1}$
$\overline{K}^0$	$-\frac{2}{9}Tr[\gamma_L L(x,v)\gamma_\nu L(v,x)]$ $Tr[\gamma_L[L(x,t_K)\gamma_5 H(t_K,u)\gamma_\mu H(u,x)]^\dagger]$	$-\frac{2}{9}Tr_S[\gamma_L L(x,v)\gamma_\nu L(v,x)]_{c_1,c_2}$ $Tr_S[\gamma_L[L(x,t_K)\gamma_5 H(t_K,u)\gamma_\mu H(u,x)]^\dagger]_{c_2,c_1}$

Table E.2: Contractions for $\langle J_\mu(u)J_\nu(v)H_w(x)K_L(t_K)\rangle$ type I diagram 2(a)

	Q_1	Q_2
K^0	$\frac{1}{9}Tr[\gamma_L L(x,x)]$ $Tr[\gamma_L L(x,u)\gamma_\mu L(u,t_K)\gamma_5 H(t_K,v)\gamma_\nu H(v,x)]$	$-\frac{1}{9}Tr[\gamma_L L(x,x)$ $\gamma_L L(x,u)\gamma_\mu L(u,t_K)\gamma_5 H(t_K,v)\gamma_\nu H(v,x)]$
$\overline{K}^0$	$-\frac{1}{9}Tr[\gamma_L L(x,x)]$ $Tr[\gamma_L[L(x,u)\gamma_\mu L(u,t_K)\gamma_5 H(t_K,v)\gamma_\nu H(v,x)]^\dagger]$	$\frac{1}{9}Tr[\gamma_L L(x,x)$ $\gamma_L[L(x,u)\gamma_\mu L(u,t_K)\gamma_5 H(t_K,v)\gamma_\nu H(v,x)]^\dagger]$

Table E.3: Contractions for $\langle J_\mu(u)J_\nu(v)H_w(x)K_L(t_K)\rangle$ type II diagram 1(a)

	Q_1	Q_2
K^0	$\frac{4}{9}Tr[\gamma_L L(x,t_K)\gamma_5 H(t_K,x)]$ $Tr[\gamma_L L(x,u)\gamma_\mu L(u,v)\gamma_\nu L(v,x)]$	$-\frac{4}{9}Tr[\gamma_L L(x,t_K)\gamma_5 H(t_K,x)$ $\gamma_L L(x,u)\gamma_\mu L(u,v)\gamma_\nu L(v,x)]$
$\overline{K}^0$	$-\frac{4}{9}Tr[\gamma_L[L(x,t_K)\gamma_5 H(t_K,x)]^\dagger]$ $Tr[\gamma_L L(x,u)\gamma_\mu L(u,v)\gamma_\nu L(v,x)]$	$\frac{4}{9}Tr[\gamma_L[L(x,t_K)\gamma_5 H(t_K,x)]^\dagger$ $\gamma_L L(x,u)\gamma_\mu L(u,v)\gamma_\nu L(v,x)]$

Table E.4: Contractions for $\langle J_\mu(u)J_\nu(v)H_w(x)K_L(t_K)\rangle$ type III diagram 1(a)

	Q_1	Q_2
K^0	$\frac{1}{9}Tr[\gamma_L L(x,x)]$ $Tr[\gamma_L L(x,v)\gamma_\nu L(v,u)\gamma_\mu L(u,t_K)\gamma_5 H(t_K,x)]$	$-\frac{1}{9}Tr[\gamma_L L(x,x)$ $\gamma_L L(x,v)\gamma_\nu L(v,u)\gamma_\mu L(u,t_K)\gamma_5 H(t_K,x)]$
$\overline{K}^0$	$-\frac{1}{9}Tr[\gamma_L L(x,x)]$ $Tr[\gamma_L[L(x,v)\gamma_\nu L(v,u)\gamma_\mu L(u,t_K)\gamma_5 H(t_K,x)]^\dagger]$	$\frac{1}{9}Tr[\gamma_L L(x,x)$ $\gamma_L[L(x,v)\gamma_\nu L(v,u)\gamma_\mu L(u,t_K)\gamma_5 H(t_K,x)]^\dagger]$

Table E.5: Contractions for $\langle J_\mu(u)J_\nu(v)H_w(x)K_L(t_K)\rangle$ type IV diagram 1(a)

	Q_1	Q_2
K^0	$\frac{1}{9}Tr[\gamma_L L(x,x)]$ $Tr[\gamma_L L(x,t_K)\gamma_5 H(t_K,u)\gamma_\mu H(u,v)\gamma_\nu H(v,x)]$	$-\frac{1}{9}Tr[\gamma_L L(x,x)$ $\gamma_L L(x,t_K)\gamma_5 H(t_K,u)\gamma_\mu H(u,v)\gamma_\nu H(v,x)]$
$\overline{K}^0$	$-\frac{1}{9}Tr[\gamma_L L(x,x)]$ $Tr[\gamma_L[L(x,t_K)\gamma_5 H(t_K,u)\gamma_\mu H(u,v)\gamma_\nu H(v,x)]^\dagger]$	$\frac{1}{9}Tr[\gamma_L L(x,x)$ $\gamma_L[L(x,t_K)\gamma_5 H(t_K,u)\gamma_\mu H(u,v)\gamma_\nu H(v,x)]^\dagger]$

Table E.6: Contractions for $\langle J_\mu(u)J_\nu(v)H_w(x)K_L(t_K)\rangle$ type IV diagram 2(a)

	Q_1	Q_2
K^0	$-\frac{5}{9}Tr[\gamma_\mu L(u,v)\gamma_\nu L(v,u)]$ $Tr[\gamma_L L(x,t_K)\gamma_5 H(t_K,x)]Tr[\gamma_L L(x,x)]$	$\frac{5}{9}Tr[\gamma_\mu L(u,v)\gamma_\nu L(v,u)]$ $Tr[\gamma_L L(x,t_K)\gamma_5 H(t_K,x)\gamma_L L(x,x)]$
$\overline{K}^0$	$\frac{5}{9}Tr[\gamma_\mu L(u,v)\gamma_\nu L(v,u)]$ $Tr[\gamma_L[L(x,t_K)\gamma_5 H(t_K,x)]^\dagger]Tr[\gamma_L L(x,x)]$	$-\frac{5}{9}Tr[\gamma_\mu L(u,v)\gamma_\nu L(v,u)]$ $Tr[\gamma_L[L(x,t_K)\gamma_5 H(t_K,x)]^\dagger\gamma_L L(x,x)]$

Table E.7: Contractions for $\langle J_\mu(u)J_\nu(v)H_w(x)K_L(t_K)\rangle$ type V diagram 1

	Q_1	Q_2
K^0	$-\frac{1}{9}Tr[\gamma_\mu H(u,v)\gamma_\nu H(v,u)]$ $Tr[\gamma_L L(x,t_K)\gamma_5 H(t_K,x)]Tr[\gamma_L L(x,x)]$	$\frac{1}{9}Tr[\gamma_\mu H(u,v)\gamma_\nu H(v,u)]$ $Tr[\gamma_L L(x,t_K)\gamma_5 H(t_K,x)\gamma_L L(x,x)]$
$\overline{K}^0$	$\frac{1}{9}Tr[\gamma_\mu H(u,v)\gamma_\nu H(v,u)]$ $Tr[\gamma_L[L(x,t_K)\gamma_5 H(t_K,x)]^\dagger]Tr[\gamma_L L(x,x)]$	$-\frac{1}{9}Tr[\gamma_\mu H(u,v)\gamma_\nu H(v,u)]$ $Tr[\gamma_L[L(x,t_K)\gamma_5 H(t_K,x)]^\dagger\gamma_L L(x,x)]$

Table E.8: Contractions for $\langle J_\mu(u)J_\nu(v)H_w(x)K_L(t_K)\rangle$ type V diagram 2

E.2 Contractions for $\langle \pi^0(t_\pi) H_w(x) K_L(t_K) \rangle$

	Q_1	Q_2
K^0	$\frac{\sqrt{2}}{2} Tr[\gamma_L L(x,t_\pi)\gamma_5 L(t_\pi,x)]$ $Tr[\gamma_L L(x,t_K)\gamma_5 H(t_K,x)]$	$-\frac{\sqrt{2}}{2} Tr[\gamma_L L(x,t_\pi)\gamma_5 L(t_\pi,x)$ $\gamma_L L(x,t_K)\gamma_5 H(t_K,x)]$
$\overline{K}^0$	$\frac{\sqrt{2}}{2} Tr[\gamma_L L(x,t_\pi)\gamma_5 L(t_\pi,x)]$ $Tr[\gamma_L H(x,t_K)\gamma_5 L(t_K,x)]$	$-\frac{\sqrt{2}}{2} Tr[\gamma_L L(x,t_\pi)\gamma_5 L(t_\pi,x)$ $\gamma_L H(x,t_K)\gamma_5 L(t_K,x)]$

Table E.9: Contractions for $\langle \pi^0(t_\pi) H_w(x) K_L(t_K) \rangle$ type I diagram 1

	Q_1	Q_2
K^0	$-\frac{\sqrt{2}}{2} Tr[\gamma_L L(x,x)]$ $Tr[\gamma_L L(x,t_\pi)\gamma_5 L(t_\pi,t_K)\gamma_5 H(t_K,x)]$	$\frac{\sqrt{2}}{2} Tr[\gamma_L L(x,x)$ $\gamma_L L(x,t_\pi)\gamma_5 L(t_\pi,t_K)\gamma_5 H(t_K,x)]$
$\overline{K}^0$	$-\frac{\sqrt{2}}{2} Tr[\gamma_L L(x,x)]$ $Tr[\gamma_L H(x,t_K)\gamma_5 L(t_K,t_\pi)\gamma_5 L(t_\pi,x)]$	$\frac{\sqrt{2}}{2} Tr[\gamma_L L(x,x)$ $\gamma_L H(x,t_K)\gamma_5 L(t_K,t_\pi)\gamma_5 L(t_\pi,x)]$

Table E.10: Contractions for $\langle \pi^0(t_\pi) H_w(x) K_L(t_K) \rangle$ type II diagram

E.3 Contractions for $\langle \eta(t_\eta)\bar{s}d(x)K^0(t_K)\rangle$

K^0	$-\frac{1}{\sqrt{6}}Tr\left[\gamma_5 L(t_\eta,t_K)\gamma_5 H(t_K,x)L(x,t_\eta)\right]$
$\overline{K}^0$	$-\frac{1}{\sqrt{6}}Tr\left[\gamma_5 L(t_\eta,x)H(x,t_K)\gamma_5 L(t_K,t_\eta)\right]$

Table E.11: Contractions for $\langle \eta(t_\eta)\bar{s}d(x)K^0(t_K)\rangle$ type I diagram 1

K^0	$\frac{2}{\sqrt{6}}Tr\left[\gamma_5 H(t_\eta,x)L(x,t_K)\gamma_5 H(t_K,t_\eta)\right]$
$\overline{K}^0$	$\frac{2}{\sqrt{6}}Tr\left[\gamma_5 H(t_\eta,t_K)\gamma_5 L(t_K,x)H(x,t_\eta)\right]$

Table E.12: Contractions for $\langle \eta(t_\eta)\bar{s}d(x)K^0(t_K)\rangle$ type I diagram 2

K^0	$\frac{2}{\sqrt{6}}Tr\left[\gamma_5 L(t_\eta,t_\eta)\right]Tr\left[L(x,t_K)\gamma_5 H(t_K,x)\right]$
$\overline{K}^0$	$\frac{2}{\sqrt{6}}Tr\left[\gamma_5 L(t_\eta,t_\eta)\right]Tr\left[H(x,t_K)\gamma_5 L(t_K,x)\right]$

Table E.13: Contractions for $\langle \eta(t_\eta)\bar{s}d(x)K^0(t_K)\rangle$ type I diagram 1

K^0	$-\frac{2}{\sqrt{6}}Tr\left[\gamma_5 H(t_\eta,t_\eta)\right]Tr\left[L(x,t_K)\gamma_5 H(t_K,x)\right]$
$\overline{K}^0$	$-\frac{2}{\sqrt{6}}Tr\left[\gamma_5 H(t_\eta,t_\eta)\right]Tr\left[H(x,t_K)\gamma_5 L(t_K,x)\right]$

Table E.14: Contractions for $\langle \eta(t_\eta)\bar{s}d(x)K^0(t_K)\rangle$ type I diagram 2

E.4 Contractions for $\langle \eta(t_\eta) H_w(x) K^0(t_K) \rangle$

	Q_1	Q_2
K^0	$\frac{1}{\sqrt{6}} Tr[\gamma_L L(x,t_\eta)\gamma_5 L(t_\eta,x)]$ $Tr[\gamma_L L(x,t_K)\gamma_5 H(t_K,x)]$	$-\frac{1}{\sqrt{6}} Tr[\gamma_L L(x,t_\eta)\gamma_5 L(t_\eta,x)$ $\gamma_L L(x,t_K)\gamma_5 H(t_K,x)]$
$\overline{K}^0$	$\frac{1}{\sqrt{6}} Tr[\gamma_L L(x,t_\eta)\gamma_5 L(t_\eta,x)]$ $Tr[\gamma_L H(x,t_K)\gamma_5 L(t_K,x)]$	$-\frac{1}{\sqrt{6}} Tr[\gamma_L L(x,t_\eta)\gamma_5 L(t_\eta,x)$ $\gamma_L H(x,t_K)\gamma_5 L(t_K,x)]$

Table E.15: Contractions for $\langle \eta(t_\eta) H_w(x) K_L(t_K) \rangle$ type I diagram

	Q_1	Q_2
K^0	$\frac{1}{\sqrt{6}} Tr[\gamma_L L(x,x)]$ $Tr[\gamma_L L(x,t_\eta)\gamma_5 L(t_\eta,t_K)\gamma_5 H(t_K,x)]$	$-\frac{1}{\sqrt{6}} Tr[\gamma_L L(x,x)$ $\gamma_L L(x,t_\eta)\gamma_5 L(t_\eta,t_K)\gamma_5 H(t_K,x)]$
$\overline{K}^0$	$\frac{1}{\sqrt{6}} Tr[\gamma_L L(x,x)]$ $Tr[\gamma_L H(x,t_K)\gamma_5 L(t_K,t_\eta)\gamma_5 L(t_\eta,x)]$	$-\frac{1}{\sqrt{6}} Tr[\gamma_L L(x,x)$ $\gamma_L H(x,t_K)\gamma_5 L(t_K,t_\eta)\gamma_5 L(t_\eta,x)]$

Table E.16: Contractions for $\langle \eta(t_\eta) H_w(x) K_L(t_K) \rangle$ type II diagram 1

	Q_1	Q_2
K^0	$-\frac{2}{\sqrt{6}} Tr[\gamma_L L(x,x)]$ $Tr[\gamma_L L(x,t_K)\gamma_5 H(t_K,t_\eta)\gamma_5 H(t_\eta,x)]$	$\frac{2}{\sqrt{6}} Tr[\gamma_L L(x,x)$ $\gamma_L L(x,t_K)\gamma_5 H(t_K,t_\eta)\gamma_5 H(t_\eta,x)]$
$\overline{K}^0$	$-\frac{2}{\sqrt{6}} Tr[\gamma_L L(x,x)]$ $Tr[\gamma_L H(x,t_\eta)\gamma_5 H(t_\eta,t_K)\gamma_5 L(t_K,x)]$	$\frac{2}{\sqrt{6}} Tr[\gamma_L L(x,x)$ $\gamma_L H(x,t_\eta)\gamma_5 H(t_\eta,t_K)\gamma_5 L(t_K,x)]$

Table E.17: Contractions for $\langle \eta(t_\eta) H_w(x) K_L(t_K) \rangle$ type II diagram 2

	Q_1	Q_2
K^0	$-\frac{2}{\sqrt{6}} Tr\left[\gamma_5 L(t_\eta,t_\eta)\right]$ $Tr[\gamma_L L(x,x)] Tr[\gamma_L L(x,t_K)\gamma_5 H(t_K,x)]$	$\frac{2}{\sqrt{6}} Tr\left[\gamma_5 L(t_\eta,t_\eta)\right]$ $Tr[\gamma_L L(x,x)\gamma_L L(x,t_K)\gamma_5 H(t_K,x)]$
$\overline{K}^0$	$-\frac{2}{\sqrt{6}} Tr\left[\gamma_5 L(t_\eta,t_\eta)\right]$ $Tr[\gamma_L L(x,x)] Tr[\gamma_L H(x,t_K)\gamma_5 L(t_K,x)]$	$\frac{2}{\sqrt{6}} Tr\left[\gamma_5 L(t_\eta,t_\eta)\right]$ $Tr[\gamma_L L(x,x)\gamma_L H(x,t_K)\gamma_5 L(t_K,x)]$

Table E.18: Contractions for $\langle \eta(t_\eta) H_w(x) K_L(t_K) \rangle$ type III diagram 1

	Q_1	Q_2
K^0	$\frac{2}{\sqrt{6}} Tr\left[\gamma_5 H(t_\eta, t_\eta)\right]$ $Tr[\gamma_L L(x,x)] Tr[\gamma_L L(x,t_K)\gamma_5 H(t_K,x)]$	$-\frac{2}{\sqrt{6}} Tr\left[\gamma_5 H(t_\eta, t_\eta)\right]$ $Tr[\gamma_L L(x,x)\gamma_L L(x,t_K)\gamma_5 H(t_K,x)]$
$\overline{K}^0$	$\frac{2}{\sqrt{6}} Tr\left[\gamma_5 H(t_\eta, t_\eta)\right]$ $Tr[\gamma_L L(x,x)] Tr[\gamma_L H(x,t_K)\gamma_5 L(t_K,x)]$	$-\frac{2}{\sqrt{6}} Tr\left[\gamma_5 H(t_\eta, t_\eta)\right]$ $Tr[\gamma_L L(x,x)\gamma_L H(x,t_K)\gamma_5 L(t_K,x)]$

Table E.19: Contractions for $\langle \eta(t_\eta) H_w(x) K_L(t_K) \rangle$ type III diagram 2

E.5 Contractions for $\langle J_\mu(u)J_\nu(v)(\bar{s}d(x) + \bar{d}s(x))K_L(t_K)\rangle$

K^0	$-\frac{1}{9}\,Tr[\gamma_\mu L(u,t_K)\gamma_5 H(t_K,v)\gamma_\nu H(v,x)L(x,u)]$
$\overline{K}^0$	$-\frac{1}{9}Tr[\gamma_\mu L(u,x)H(x,v)\gamma_\nu H(v,t_K)\gamma_5 L(t_K,u)]$

Table E.20: Contractions for $\langle J_\mu(u)J_\nu(v)(\bar{s}d(x) + \bar{d}s(x))K_L(t_K)\rangle$ type I diagram 1(a)

K^0	$-\frac{1}{9}\,Tr[\gamma_\mu L(u,t_K)\gamma_5 H(t_K,x)L(x,v)\gamma_\nu L(v,u)]$
$\overline{K}^0$	$-\frac{1}{9}\,Tr[\gamma_\mu L(u,v)\gamma_\nu L(v,x)H(x,t_K)\gamma_5 L(t_K,u)]$

Table E.21: Contractions for $\langle J_\mu(u)J_\nu(v)(\bar{s}d(x) + \bar{d}s(x))K_L(t_K)\rangle$ type II diagram 1(a)

K^0	$-\frac{1}{9}\,Tr[\gamma_\mu H(u,v)\gamma_\nu H(v,x)L(x,t_K)\gamma_5 H(t_K,u)]$
$\overline{K}^0$	$-\frac{1}{9}\,Tr[\gamma_\mu H(u,t_K)\gamma_5 L(t_K,x)H(x,v)\gamma_\nu H(v,u)]$

Table E.22: Contractions for $\langle J_\mu(u)J_\nu(v)(\bar{s}d(x) + \bar{d}s(x))K_L(t_K)\rangle$ type II diagram 2(a)

K^0	$\frac{5}{9}\,Tr[\gamma_\mu L(u,v)\gamma_\nu L(v,u)]Tr[L(x,t_K)\gamma_5 H(t_K,x)]$
$\overline{K}^0$	$\frac{5}{9}\,Tr[\gamma_\mu L(u,v)\gamma_\nu L(v,u)]Tr[H(x,t_K)\gamma_5 L(t_K,x)]$

Table E.23: Contractions for $\langle J_\mu(u)J_\nu(v)(\bar{s}d(x) + \bar{d}s(x))K_L(t_K)\rangle$ type III diagram 1

K^0	$\frac{1}{9}\,Tr[\gamma_\mu H(u,v)\gamma_\nu H(v,u)]Tr[L(x,t_K)\gamma_5 H(t_K,x)]$
$\overline{K}^0$	$\frac{1}{9}\,Tr[\gamma_\mu H(u,v)\gamma_\nu H(v,u)]Tr[H(x,t_K)\gamma_5 L(t_K,x)]$

Table E.24: Contractions for $\langle J_\mu(u)J_\nu(v)(\bar{s}d(x) + \bar{d}s(x))K_L(t_K)\rangle$ type III diagram 2